UNIVERSITÀ DI PISA

Scuola di Dottorato in Ingegneria "Leonardo da Vinci"

Corso di Dottorato di Ricerca in
SCIENZE E TECNICHE DELL'INGEGNERIA CIVILE

ICAR/08 Scienza delle Costruzioni

On the Detachment of FRP Stiffeners from Brittle-Elastic Substrates

Tesi di Dottorato di Ricerca

Autore:

Annalisa Franco

Tutore:

prof. Gianni Royer-Carfagni

Anno 2014

Everything Should Be Made as
Simple as Possible,
But Not Simpler.

Albert Einstein

SOMMARIO

Materiali compositi fibro-rinforzati a matrice polimerica (FRP) sono correntemente impiegati per il rinforzo e la riabilitazione di strutture in calcestruzzo o muratura, ottenuti tramite l'incollaggio di lamine di forma opportuna sulla superficie dell'elemento debole. Studi sperimentali hanno mostrato che il collasso avviene per delaminazione della lamina di FRP dal supporto, innescata dalla concentrazione di tensione all'estremità del rinforzo. La frattura si propaga prima all'interfaccia parallelamente al rinforzo e poi all'interno del substrato, portando alla completa separazione dei due aderenti. La rottura finale è spesso caratterizzata dal distacco di un bulbo a forma di cuneo dal substrato, che rimane adeso alla lamina di FRP. Per descrivere l'intero processo, si è considerato il problema-modello di una lamina sottile elastica, incollata al bordo di una lastra semi-infinita in stato piano generalizzato di tensione. Lo spessore del rinforzo è supposto piccolo in modo tale da poterne trascurare la rigidezza flessionale, così che le tensioni di contatto sono tangenziali. Al contrario di quanto avviene nei modelli correnti, non si trascurano le deformazioni elastiche del supporto: questo costituisce la principale novità dell'approccio proposto. La compatibilità delle deformazioni tra rinforzo e substrato si traduce in un'equazione integrale singolare per il problema di contatto, la cui soluzione è ottenuta con un'espansione in serie di Chebyshev. Il processo di delaminazione, che avviene prevalentemente in modalità II di frattura, è attivato nel momento in cui il rilascio di energia di deformazione eguaglia l'energia di frattura dell'interfaccia. Se l'adesione è perfetta, il modello elastico predice la singolarità degli sforzi agli estremi del rinforzo. Le tensioni nell'intorno della singolarità all'estremità caricata della lamina equilibrano, in pratica, l'intero carico applicato, in disaccordo con l'evidenza sperimentale che mostra invece una lunghezza effettiva di incollaggio (EBL), dove il trasferimento del carico avviene gradualmente. Per risolvere questa incongruenza, in una seconda modellazione è stata introdotta una zona coesiva in corrispondenza dell'estremo caricato, in cui si può avere scorrimento tra i due aderenti secondo una relazione costitutiva di interfaccia, finché non si raggiunge un valore limite dello scorrimento. Seguendo un approccio alla Barenblatt, la lunghezza della zona coesiva è trovata imponendo che il fattore di intensificazione degli sforzi sia nullo in corrispondenza della transizione tra zona adesa e zona coesa, così da eliminare la singolarità. Esiste una massima lunghezza di tale zona, nella quale le forze coesive equilibrano praticamente tutto il carico applicato, e che pertanto può essere indicata come la EBL. Si è pure mostrato che la singolarità all'altro estremo del rinforzo non ha un ruolo importante, essendo trascurabile la parte di carico ad essa associata. Per descrivere il fenomeno del distacco del bulbo cuneiforme, si è considerato un modello alla Griffith per la frattura del substrato, assumendo un propagazione di cricca per quanti di lunghezza finita, dello stesso ordine di grandezza della lunghezza intrinseca del materiale. Dalla competizione, in termini energetici e tensionali, fra la rottura all'interfaccia del giunto e la fessurazione del substrato, è stato possibile determinare un angolo critico di propagazione della cricca che coincide con l'angolo caratteristico del cuneo distaccato. I risultati ottenuti dai modelli analitici sviluppati sono in ottimo accordo con i risultati sperimentali.

ABSTRACT

Fiber Reinforced Polymers (FRP) are commonly used for strengthening and rehabilitation of concrete or masonry structures, by gluing strips or plates made of this material on the surface of the weak material. Experimental studies have provided evidence that the main failure mode is the debonding of the FRP stiffener from the support, triggered by high stress concentrations at the extremities of the stiffener. Fracture propagates firstly parallel to the interface and then in the substrate, until complete separation between the two adherents occurs. Final failure is often characterized by the detachment of a wedge-shaped portion of the substrate, which remains bonded to the FRP strip. In order to describe the whole process, the model problem considered here is that of a finite thin elastic stiffener, bonded to an elastic half-space in generalized plane stress, pulled at one end by an axial force. The thickness of the stiffener is supposed very small, so that its bending stiffness can be considered negligible and only shear stresses act at the interface. On the contrary to the common assumptions of current models, the elastic deformations of the substrate are not neglected here: this is the main novelty of the proposed approach. Compatibility equations between the stiffener and the substrate allow to write a singular integral equation for the contact problem, whose solution can then be obtained through an expansion in Chebyshev's series. The debonding process in pure mode II is supposed to be activated by an energetic balance, i.e., when the release of elastic strain energy equals the surface energy associated with material separation. If the bond is perfect, the theory of elasticity predicts stress singularities at both ends of the stiffener. The shear stresses in a neighborhood of the singularity at the loaded end of the FRP strip is sufficient to counterbalance, in practice, the whole load applied, while the experimental evidence shows instead an *effective bond length* (EBL), over which the load transfer occurs gradually. To solve this inconsistency, in a second model a cohesive zone has been introduced at the loaded end of the stiffener, where slippage can occur according to an interface constitutive law, until a limit slip value is reached. Following an approach *à là* Barenblatt, the length of this zone is found by imposing that the stress intensity factor is null at the transition zone between the completely bonded part and the cohesive part, so to annihilate the stress singularity. There is a maximal reachable length of this cohesive zone, in which cohesive forces counterbalance, in practice, all the applied load, and which, therefore, can be referred to as the EBL. It can be also demonstrated that the second singularity at the free end of the stiffener plays a minor role, being negligible the load associated with it. In order to describe the phenomenon of the wedge-shaped fracturing of concrete, a fracture mechanics problem *à là* Griffith has been considered for the substrate, assuming the crack propagation occurs in steps of finite length (quanta), of the same order of the intrinsic material length scale. From the energetic and tensional competition between the failure of the adhesive joint and the fracturing of the substrate, it has been possible to determine a critic propagation angle which coincides with the characteristic angle of the detached wedge-shaped bulb. Results obtained from the analytical models are in very good agreement with the experimental results.

ACKNOWLEDGEMENTS

My most grateful thank you goes to Professor Gianni Royer Carfagni for his valuable advice and guidance, without which this thesis would not have been possible. Numerous and intense discussions provided me with an insight into fracture mechanics problems and allowed me to increase my knowledge in the theory of elasticity and its useful tools. His knowledge, experience and suggestions have been the basis for my scientific growth.

I would like to thank Professor Roberto Ballarini and his family for their kind hospitality in the beautiful city of Minneapolis. Their hospitality added to my experiences there and helped to make the period I lived in the US one of the most beautiful experiences of my life. I really appreciated having the opportunity to work in the excellent research environment of the University of Minnesota, and the support and feedback on my work improved its quality significantly.

I would like to address a special word to professor Michele Buonsanti who always believed in me and convinced me to start this beautiful path in the research world. He always has had warm words to support my choices and pushed me to always give my best effort in everything.

I cannot forget all of the new friends and people I met in this period in Pisa, Parma, and Minneapolis. They are now part of my life and in some way contributed to make these three years easier to live far from my family.

Last but not least, I would like to express my deep gratitude to my family for their interest in my work and their continuous support, which have been of inestimable value during my academic education. Despite the distance, my parents and my siblings are always present in my life helping me to overcome every difficulty I encounter in my life's path.

TABLE OF CONTENTS

TABLE OF CONTENTS **IX**

LIST OF SYMBOLS **XI**

LIST OF ACRONYMS **XVII**

1 INTRODUCTION **1**

1.1 Background **1**

1.2 Research objective and scope **1**

1.3 Outline **2**

2 STATE OF THE ART **3**

2.1 Introduction **3**

2.2 Mechanical properties of FRP **3**

2.3 FRP strengthening of structural elements **6**

2.3.1 Failure modes 9

2.3.2 Bond-slip behavior 12

2.3.2.1 Bond strength *12*

2.3.2.2 Effective bond length *13*

2.3.2.3 Interface constitutive law *13*

2.4 Analysis of the debonding process **15**

2.5 Open problems **18**

3 THE EFFECT OF THE DEFORMATION OF THE SUBSTRATE **23**

3.1 Introduction **23**

3.2 Load transfer from an elastic stiffener to a semi-infinite plate **24**

3.3 Energetic balance **27**

3.3.1 Generalization of the *Crack Closure Integral Method* by Irwin . 27
3.3.2 Strain energy release rate 29
3.3.3 Energetic balance 32

3.4 Comparison with experiments 36

3.5 Discussion 41

4 THE ROLE OF COHESIVE INTERFACE FORCES 43

4.1 Introduction 43

4.2 Adhesion of an elastic stiffener to an elastic substrate . . . 44
4.2.1 Double-Cohesive-Zone (Double Cohesive Zone model (DCZ)) model 44
4.2.2 Single-Cohesive-Zone (Single Cohesive Zone model (SCZ)) model 48
4.2.3 No-Cohesive-Zone (No Cohesive Zone model (NCZ)) model . . 50

4.3 Analysis of the debonding process 50
4.3.1 Constitutive law for the cohesive interface 50
4.3.2 Load-displacement curve for long stiffeners 53
4.3.3 Load-displacement curve for short stiffeners 57

4.4 Theoretical prediction of the contact shear stress 59

4.5 Effective bond length. Comparison with experiments . . . 65
4.5.1 Assessment of the constitutive properties of the interface from experiments. 65
4.5.2 Results from the various models. 69

4.6 Discussion 73

5 WEDGE-SHAPED FRACTURING OF SUBSTRATE 77

5.1 Introduction 77

5.2 The model problem 79
5.2.1 Preliminary considerations 79
5.2.2 Governing equations in linear elasticity theory 83
5.2.2.1 Problem I: elastic half-plane with edge dislocations 84
5.2.2.2 Problem II: elastic half-plane under surface tangential stress 86

5.3 Solution of the elastic problem 87
5.3.1 Approximation in Chebyshev's series 87
5.3.2 Stress intensity factors 89

5.4 Competing mechanisms of failure 90

5.5 Comparison with experiments 94

5.6 Discussion 98

6 CONCLUSIONS 101

6.1 Review . . . 101

6.2 Contributions . . . 104

6.3 Further developments and future research . . . 105

A CHEBYSHEV POLYNOMIALS 107

B GREEN'S FUNCTIONS 109

C STRESS AND STRAIN ON THE WEDGE-SHAPED-CRACKED HALF-PLANE, LOADED FOR THE WHOLE BOND LENGTH 111

REFERENCES 115

LIST OF SYMBOLS

General Notation

$(\cdot)'$	Differentiation with respect to the complex variable z	83
$(\cdot)_d$	Contribution of dislocations	84
$(\cdot)_q$	Contribution of shear stress	84
$(\cdot)_w$	Quantity dependent upon omega	90
$(\cdot)_{dc}$	Analytical continuation	85
$(\cdot)_{dw}$	Elastic solution for a dislocation acting on a whole plane	84
$(\cdot)_n$	Normalized quantity	89
$\overline{(\cdot)}$	Complex conjugation	83

Roman Symbols (Upper Case)

A_s	Cross sectional area of the stiffener	25
B	Distribution of dislocations	86
B_{reg}	Regular function	88

E	Total energy	29
E_{FRP}	Elastic modulus of FRP	6
E_p	Elastic modulus of the plate	25
E_s	Elastic modulus of the stiffener	25
E_f	Elastic modulus of the fiber	6
E_m	Elastic modulus of the matrix	6
G	Strain energy release rate	29
G_f	Interface fracture energy	12
G_r	Energy release rate for a rigid substrate	33
H_1, H_2, H_3	Green's functions for the shear stress	86
K	Complex stress intensity factor, $K = K_I + i\,K_{II}$	89
K_1, K_2, K_3, K_4	Green's functions for the dislocation	86
$K_{\mathrm{II,free}}$	Mode II stress intensity factor in correspondence of the free end of the stiffener	48
$K_{\mathrm{II,load}}$	Mode II stress intensity factor in correspondence of the loaded end of the stiffener	48
K_{II}	Mode II stress intensity factor	27
L_e	Effective bond length	12
N_s	Axial force in the stiffener	25
P	Longitudinal load applied at one end of the stiffener	25
P_u	Maximum load that can be achieved by the joint	12
P_{cr}	Critical value of the axial load	32

T_s	Chebyshev polynomials of the first kind	26
U	Elastic strain energy	29
U_s	Chebyshev polynomials of the second kind	47
V_F	Volume fraction of the fiber	6
V_m	Volume fraction of the matrix	6
W/C	Water/cement ratio by weight of the concrete mix	96
X_s	Parameters of the Chebyshev series	26

Roman Symbols (Lower Case)

a	Crack length	80
a^*	Quantum of crack	93
a_0	Factor that takes account of the shape of the aggregate in the concrete mix (1 for rounded aggregates and 1.44 for crushed or angular aggregates)	96
a_{js}, b_j, c_j, d_j	Coefficients of the system of algebraic equations describing the contact problem	47
b_p	Plate width	25
b_r, b_ϑ	Radial and circumferential components of the Burgers vector of the dislocation	85
b_s	Stiffener width	25
c	Length of the cohesive zone in the SCZ model	55
c_1,c_2	Length of the cohesive zones in the DCZ model	45
c_u	Cohesive zone correspondent to the ultimate load	55
d	Length of the debonded part	55

$d_{a,\max}$	Maximum aggregate size in the concrete mix	96
f'_c	Cylinder compressive strength of concrete	12
f_{ctm}	Average tensile strength of concrete	12
f_{ck}	Characteristic compression strength of concrete	37
$i = \sqrt{-1}$	Imaginary number	83
l	Bond length	12
l_b	Lenght of the bonded part in the cohesive model	46
l_c	Length over which the shear stress is applied in the problem of a surface stress over an half-plane	86
l_e	Effective bond length according to [1]	73
q	Contact tangential force per unit length	25
q_c	Cohesive tangential force per unit length	45
q_0	Maximum allowable tangential stresses for the interface	90
s	Relative slip of the adherents	13
s_f	Fracture slip	15
t	Non-dimensional coordinate ($t \in [-1, 1]$)	26
t_s	Stiffener thickness	25
u_p	Displacement of the plate	28
u_s	Displacement of the stiffener	28
u_{rel}	Relative displacement between stiffener and plate.	30
w	Characteristic function	88
z	Complex variable $z = x + iy = re^{i\vartheta}$	83

z_0	Point in the complex plane in which there is the dislocation	84

Greek Letters (Upper Case)

Γ	Surface fracture energy	29
Γ_F	Concrete fracture energy	37
Φ	Complex potential	83
Ψ	Complex potential	83

Greek Letters (Lower Case)

(ξ, η)	Cartesian reference system	25
β	Discrete dislocation	85
κ	Kolosov's constant, $\kappa = 3 - 4\nu$ for plate strain and $\kappa = (3 - \nu)/(1 + \nu)$ for plane stress	83
κ_a	Value calculated on the basis of a statistical analysis of experimental data (evaluation of fracture energy according to [1])	37
κ_b	Geometric parameter (evaluation of fracture energy according to [1])	37
λ	Rigidity parameter	26
$\mu = G$	Shear modulus	85
ν	Poisson's ratio	83
ω	Inclination angle of the crack	80
σ_{FRP}	Ultimate strength of the FRP	6
σ_f	Tensile strength of the fibers	6
σ_m	Tensile strength of the matrix	6

$\sigma_{rr}, \sigma_{\vartheta\vartheta}, \sigma_{r\vartheta}$	Normal and shear components of stresses in polar coordinates	83
τ	1. Shear bond-stress; 2. Non-dimensional coordinate	13
τ_c	Cohesive stress corresponding to half the peak stress in a stepwise constitutive law	52
τ_f	Peak shear stress in the interface constitutive law	15
ε_p	Axial strain in the plate	25
ε_s	Axial strain in the stiffener	25
$\varepsilon_{rr}, \varepsilon_{\vartheta\vartheta}, \varepsilon_{r\vartheta}$	Normal and shear components of strains in polar coordinates	113

LIST OF ACRONYMS

DCZ	Double Cohesive Zone model.
EBL	Effective Bond Length.
FES	Far End Supported.
FMB	Fracture Mechanics Based.
FRP	Fiber Reinforced Polymer.
LVDT	Linear Variable Differential Transformer.
NCZ	No Cohesive Zone model.
NES	Near End Supported.
RC	Reinforced Concrete.
SCZ	Single Cohesive Zone model.

CHAPTER 1

INTRODUCTION

1.1 Background

In recent years, there has been an increased interest in strengthening and rehabilitation of Reinforced Concrete (RC) structures. As a matter of fact, the ageing of infrastructures, the change of service loads, the demand of higher capacities to withstand seismic events have led to the necessity of an improvement of the performance of existing construction works during their service life. An effective and non-invasive method for increasing the capacity of RC structures is through the use of externally bonded reinforcement. Steel plates have traditionally been used as reinforcement to increase the flexural an shear capacity of structural elements. However, over the last two decades, the application of Fiber Reinforced Polymers (FRP) as external reinforcement has received much attention. This material has in fact a higher tensile strength, higher strength-to-weight ratio and higher corrosion resistance than other structural materials, such as steel. Thanks to their light weight, field application of FRP plates is easier and, although the material costs may be high, the improved durability offered by FRP materials can make them the most cost-effective material in many cases. The main issue associated with FRP strengthened structures is the debonding or peeling of the plate from the support before the desired strength or ductility is achieved. Despite the amount of literary work, there exists a lack of knowledge on some aspects of the phenomenon. This may result in erroneous implementation of FRP repair methods in rehabilitating or strengthening existing structures. In order to overcome this drawback, this study focus on the debonding behavior, failure mechanisms, and interfacial properties that limit the composite system from achieving its desired goal.

1.2 Research objective and scope

The principal objectives and scope of this investigation are:

- To provide a review of the state-of-the-art in FRP strengthening concrete structures and analyze the aspects that mainly influence the behavior of a bonded joint.

- To develop an analytical model able to describe the interfacial behavior in the FRP-to-concrete bonded joint.
- To analyze the effect of the substrate elasticity in the contact problem between an elastic FRP stiffener and the concrete substrate.
- To investigate the effect of the singularities arising from the elasticity problem on the behavior of the bonded joint and the effect of cohesive forces at the interface.
- To analyze and fully describe the process of debonding of the FRP plate from the support when a longitudinal force is applied at one end.
- To develop an analytical model for the description of crack propagation into the substrate in order to give an insight on the separation of a wedge-shaped concrete prism at the free end of the FRP plate.

1.3 Outline

This thesis is divided into six chapters and three appendixes. The chapters are organized as follows:
Chapter 2 - presents a state-of-the-art review of the existing work on FRP applications in structural strengthening, pointing out the main aspects that characterize the FRP-to-concrete interaction.
Chapter 3 - introduces a model problem for the debonding of an elastic stiffener from an elastic substrate, highlighting the influence of the substrate elasticity. At this stage, the case of a perfectly-adherent stiffener is considered, focusing the attention on the debonding process assumed to begin, and continue, as soon as the energy release rate due to an infinitesimal delamination becomes equal to the interfacial fracture energy (Griffith balance).
Chapter 4 - presents a model which considers the effect of cohesive forces at the interface. The presence of cohesive zones, where slippage between FRP plate and concrete can occur, allows to eliminate the singularities predicted by the theory of elasticity in the case of a perfect adherent stiffener. As a matter of fact, stress singularities at both ends of the stiffener produce an inconsistency in reproducing some aspects of the debonding phenomenon. The cohesive model is able to describe the entire process, taking into account the main factors that thoroughly characterize it.
Chapter 5 - presents an analytical model to describe peculiar phenomenon that occurs in the last stage of debonding: an inclined crack forms starting from the free end of the stiffener, so to define a *wedge-shaped* portion of the substrate that eventually separates to form a characteristic bulb that remains attached to the stiffener. The model employees the distributed dislocation technique and the hypothesis of a finite propagation of crack.
Chapter 6 - summarizes conclusions from the investigation, contributions and recommendations for further research.

CHAPTER **2**

STATE OF THE ART

2.1 Introduction

Existing construction works have to face modification or improvement of their performance during their service life. The main causes can be the change in their use, deterioration due to exposure to an aggressive environment and abrupt events such as earthquakes. To meet the need of rehabilitating and retrofitting the existing structures, various innovative techniques and new materials have been recently developed. Among them, the outstanding performance of the Fiber Reinforced Polymer (FRP) composites makes them an excellent candidate for repairing or retrofitting existing civil infrastructures. This is due to the many advantages these materials afford when compared to conventional steel reinforcement or concrete encasement, some of which include [2]:

- light weight;
- high strength-to-weight ratios;
- outstanding durability in a variety of environments;
- ease and speed of installation, flexibility, and application techniques;
- the ability to tailor mechanical properties by appropriate choice and direction of fibres;
- outstanding fatigue characteristics (carbon FRP);
- low thermal conductivity.

2.2 Mechanical properties of FRP

Composite materials are obtained by the combination of two or more materials, on a macroscopic scale, to form a new and useful material with enhanced properties that are superior to those of the individual constituents alone. In particular, an FRP is a specific type of two-components composite material consisting of high strength fibers embedded in a polymeric matrix (Figure 2.1). The most common applications of FRPs in structural engineering comprehend: *i*) externally bonded FRP plates, sheets and wraps for strengthening of reinforced concrete, steel, aluminum and timber structural members; *ii*) FRP bars for internal reinforcement of concrete and *iii*) all-FRP-structures (structures all made by FRP materials). As regards retrofitting applications, FRP sheets or plates are typically organized in a laminate structure, such that each lamina (or flat layer) contains an arrangement of unidirectional fibers or woven fiber fabrics embedded within a thin layer of light polymer matrix material. The fibers, typically composed of carbon, glass or aramid, provide the strength and stiffness. The matrix, commonly made of epoxy, vinyl ester or polyester, binds and protects the fibers from damage, and transfers the stresses between fibers [2]. A comparison of the different FRP mechanical properties is shown in Table 2.1. Since the presence of two distinct materials, overall FRP material properties depend on the characteristics of the individual constituents.

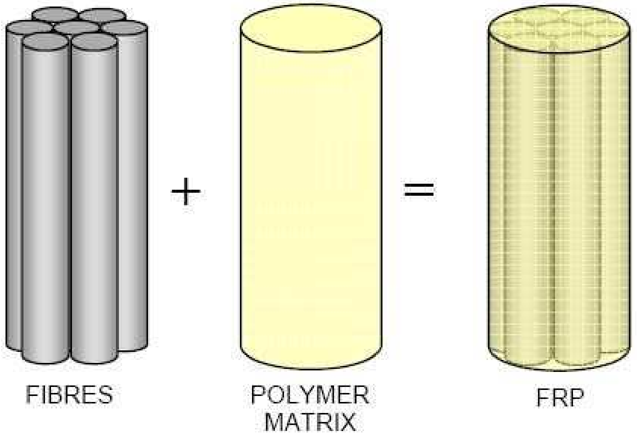

Figure 2.1: Material components of a FRP composite [2].

In particular, Figure 2.2 shows the constitutive laws of the fibers, of the matrix and the correspondent composite. It can be noted that the stiffness of the latter is lower than that of the fibers and its ultimate failure corresponds to a value of deformation equal to that of the fibers. After this value, the stress transfer from the fibers to the matrix cannot be possible.

The mechanical properties of an FRP depend also on the orientation of the fibers within the matrix. In general, for the purpose of the external reinforcement of concrete, the used FRP materials are usually unidirectional (with all the fibers oriented along the length of the sheet). There are then two different types of FRP composites available: *plates*, i.e., rigid strips obtained by a process called *pultrusion*, and *sheets*, made of raw or pre-impregnated fibers. The sheets are then applied on the element surface by saturating fibers with an epoxy resin. For unidirectional FRP materials, an estimate of the mechanical behavior of the composite can be possible using micro-mechanical models. In particular, through

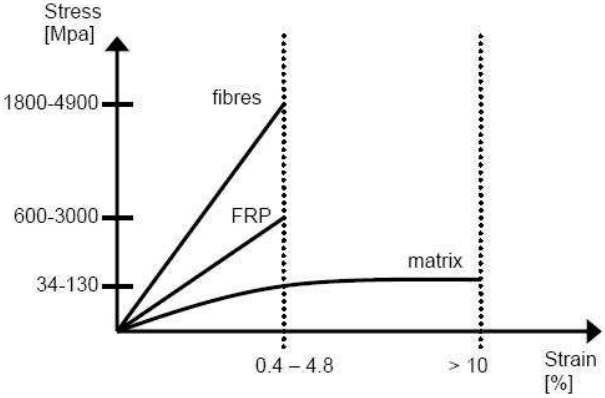

Figure 2.2: Constitutive laws of fibers, matrix and relative composite [3].

Table 2.1: Typical mechanical properties of materials used in retrofitting [4].

Material	**Tensile strength** $[MPa]$	**Modulus of elasticity** $[GPa]$	**Density** $[kg/m^3]$	**Modulus of elasticity to density ratio** $[Mm^2/s^2]$
Carbon	2200-5600	240-830	1800-2200	130-380
Aramid	2400-3600	130-160	1400-1500	90-110
Glass	3400-4800	70-90	2200-2500	31-33
Epoxy	60	2.5	1100-1400	1.8-2.3
CFRP	1500-3700	160-540	1400-1700	110-320
Steel	280-1900	190-210	7900	24-27

the *rule of mixtures*, the elastic modulus of the FRP, E_{FRP} , can be approximately expressed in terms of the elastic moduli of the component materials, E_m for the matrix and E_f for the fiber, and the their respective volume fractions, V_m and V_f, to obtain [1]:

$$E_{\text{FRP}} = V_f E_f + (1 - V_f) E_m. \tag{2.1}$$

In the same way, the ultimate strength of the FRP

$$\sigma_{\text{FRP}} = V_f \sigma_f + (1 - V_f) \sigma_m. \tag{2.2}$$

where σ_f and σ_m are the tensile strength of the fibers and of the matrix, respectively. It should be noted that the rule of mixtures, based on the hypothesis of perfect adherence between fibers and matrix, gives accurate estimation of the elastic modulus, while the value of the ultimate strength is in general not so accurate. For this reason, in the design of the reinforcing system, it is always suggested to evaluate both mechanical values (E_{FRP} and σ_{FRP}) experimentally [1].

2.3 FRP strengthening of structural elements

During the past years, FRP materials have been increasingly used for the repair and rehabilitation of existing structures. A noteworthy application refers to the flexural and shear strengthening of concrete structural elements, according to which FRP strips or plates are bonded to the exterior of the concrete members using a wet lay-up procedure with an epoxy resin. In flexural applications, the FRP sheets are bonded to the tension side of the element to improve the bending capacity. The fibers are oriented along the longitudinal axis of the beam (Figure 2.3(a)). In shear applications, FRP materials are applied on the side faces of the element (often in the form of U-wraps) (Figure 2.3(b)) to provide shear reinforcement which supplements that provided by the internal steel stirrups. In this case, the fibers are usually aligned perpendicular or rotated at a certain angle β with respect to the longitudinal axis of the beam. There are also cases in which FRPs are wrapped around reinforced concrete columns to provide confining reinforcement (Figure 2.4). Under compressive axial load, the column expands laterally and the FRP develops a tensile confining stress that places the concrete in a state of triaxial stress (Figure 2.4(a)). This significantly increases the strength and ductility of the concrete and the column. The fibers are generally perpendicular to the longitudinal axis of the element.

Due to the popularity of these techniques, most of the research is focused on the mechanical behavior of the bonded joints. There are many different experimental set-ups for the determination of the FRP-to-concrete bond strength. Chen *et al.* [5] classified the existing test set-ups into the following types (Figure 2.5): (a) Far End Supported (FES) and (b) Near End Supported (NES) double-shear tests [6, 7]; (c) FES and (d) NES single-shear tests [8, 9, 10, 11, 12, 13]; and (e)-(f) beam or bending tests [14, 15]. All these tests may also be referred to as *pull tests*, as the plate is always directly pulled by a tensile force and an extensive list of references can be found in [13, 5].

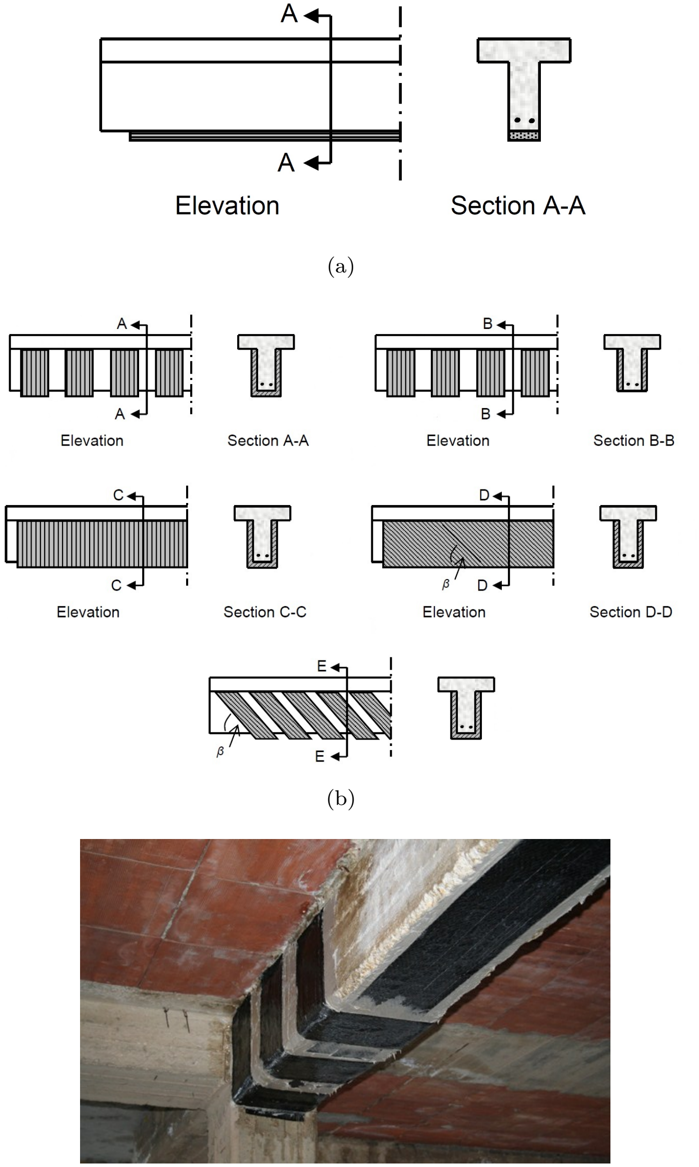
A
A
Elevation
Section A-A
(a)
A
A
Elevation
Section A-A
B
B
Elevation
Section B-B
C
C
Elevation
Section C-C
D
β
D
Elevation
Section D-D
E
β
E
(b)
(c)

Figure 2.3: Strengthening of a reinforced concrete T-beam using externally-bonded FRP reinforcement. (a) Flexural strengthening [3]; (b) Various schemes for shear strengthening [3]; (c) Flexural and shear strengthening application.

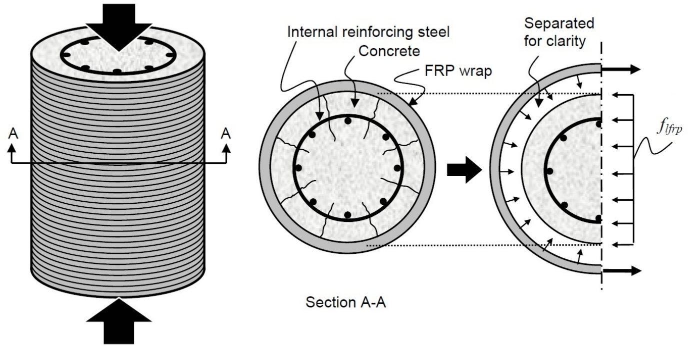
Internal reinforcing steel
Concrete
FRP wrap
Separated for clarity
A
A
f_{lfrp}
Section A-A

(a)

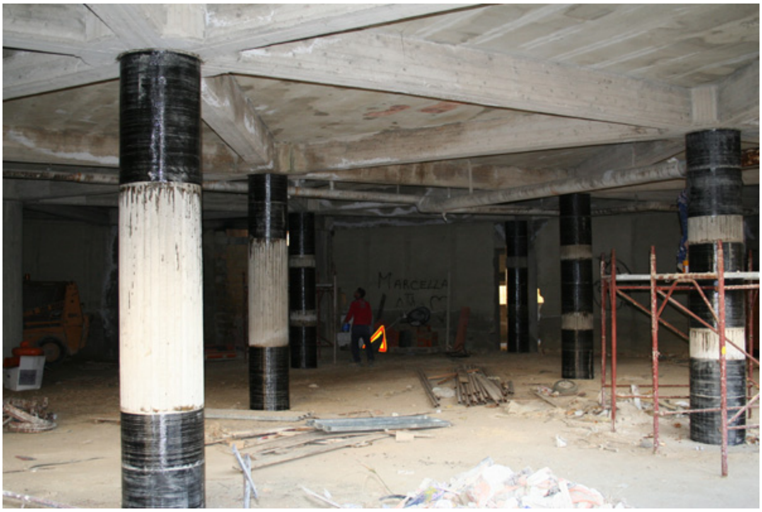

(b)

Figure 2.4: Strengthening of a circular reinforced concrete column using externally-bonded FRP wraps. (a) Confinement mechanism [3]; (b) Axial strengthening application.

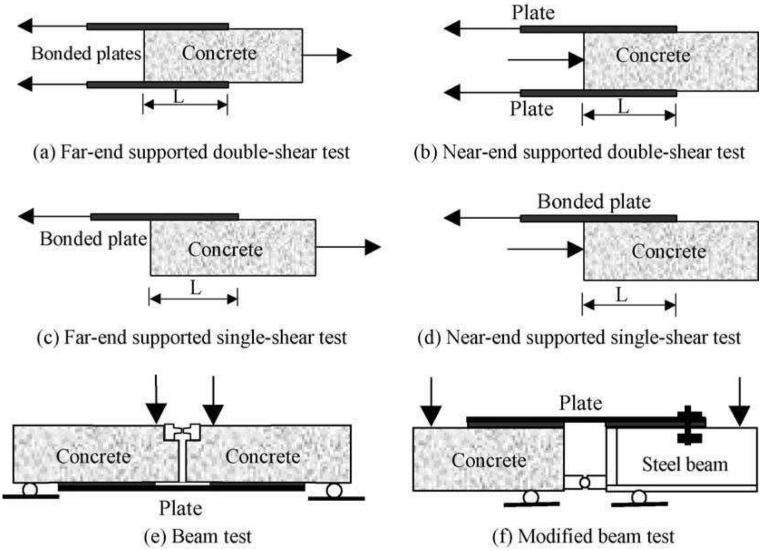
Bonded plates
Concrete
L
(a) Far-end supported double-shear test
Plate
Concrete
Plate
L
(b) Near-end supported double-shear test
Bonded plate
Concrete
L
(c) Far-end supported single-shear test
Bonded plate
Concrete
L
(d) Near-end supported single-shear test
Concrete
Concrete
Plate
(e) Beam test
Plate
Concrete
Steel beam
(f) Modified beam test

Figure 2.5: Classification of bond tests [5].

A more detailed scheme of the pull test is represented in Figure 2.6. According to some recent studies [11], if the FRP plate is bonded close to the front side of the concrete specimen, very high tensile stresses occur in this concrete portion. As a consequence, an early failure typically occurs due to concrete splitting of a prism with triangular section (Figure 2.7(a)). On the contrary, when the plate bonded length starts far from the front side, tensile stresses are much smaller with respect to previous case due to the confinement effect of concrete, and a more regular growth of delamination along the specimen can be followed during the test (Figure 2.7(b)). For this reason, in the pull-out test an unbonded zone is usually left near the loaded end of the FRP plate (Figure 2.6).

2.3.1 Failure modes

There are different failure modes of FRP-to-concrete bonded joints and interfacial debonding is one of the most common. A broadly classification can be made in order to distinguish the different failure modes for FRP strengthened concrete structures: *i*) failure related to the reach of the ultimate flexural or shear strength of the materials and *ii*) interfacial debonding. If the ends of the plate are properly anchored, then failure occurs when the ultimate flexural capacity of the beam is reached, by either tensile rupture of the FRP plate (Figure 2.8(a)) or crushing of concrete under compression (Figure 2.8(b)). The concrete beam can also fail in shear if the flexural capacity of the strengthened beam exceeds the shear capacity of the RC beam alone (Figure 2.8(c)). All these failure modes belong to the first category and occur when the full composite action between concrete and FRP is achieved. Numerous experimental studies have also reported brittle debonding failures in plated beams prior to their ultimate flexural or shear strength being reached. A variety of debonding failure modes have been observed in tests [5, 13]

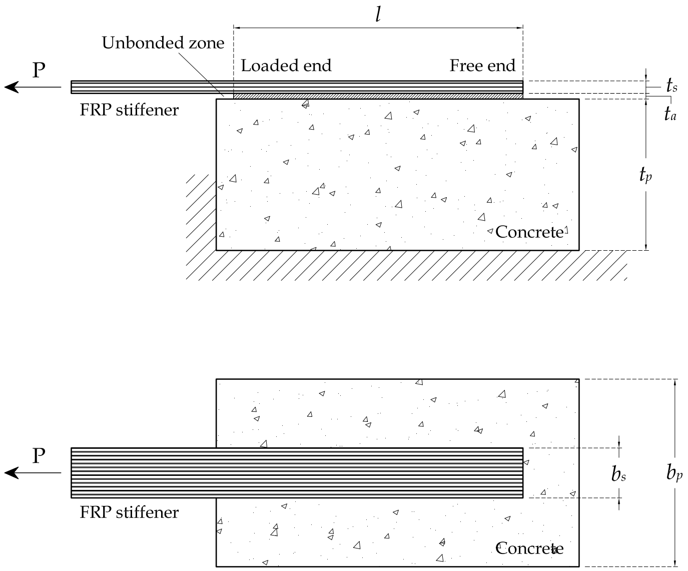
l
Unbonded zone
P
Loaded end
Free end
t_s
t_a
FRP stiffener
t_p
Concrete
P
b_s
b_p
FRP stiffener
Concrete

Figure 2.6: Scheme of a pull test.

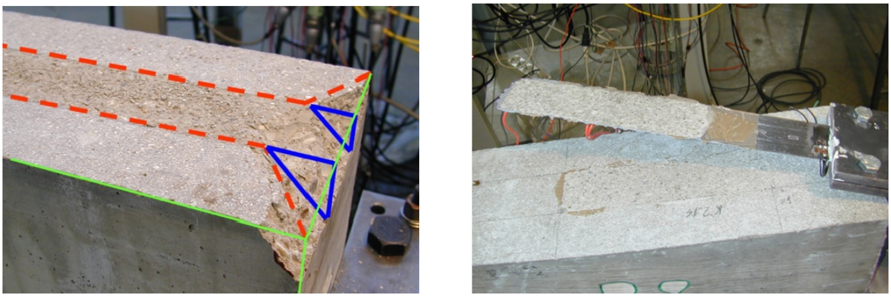
(a)
(b)

Figure 2.7: Effect of the FRP bonding mode on the concrete support [11]: (a) FRP plate bonded starting from the front side of concrete block; (b) FRP plate bonded far from the front side of concrete block.

and these can be broadly classified into two types: (a) those associated with high interfacial stresses near the ends of the bonded plate (Figure 2.8(d-e)); and (b) those induced by a flexural or flexural-shear crack (intermediate crack) away from the plate ends (Figure 2.8(f-g)).

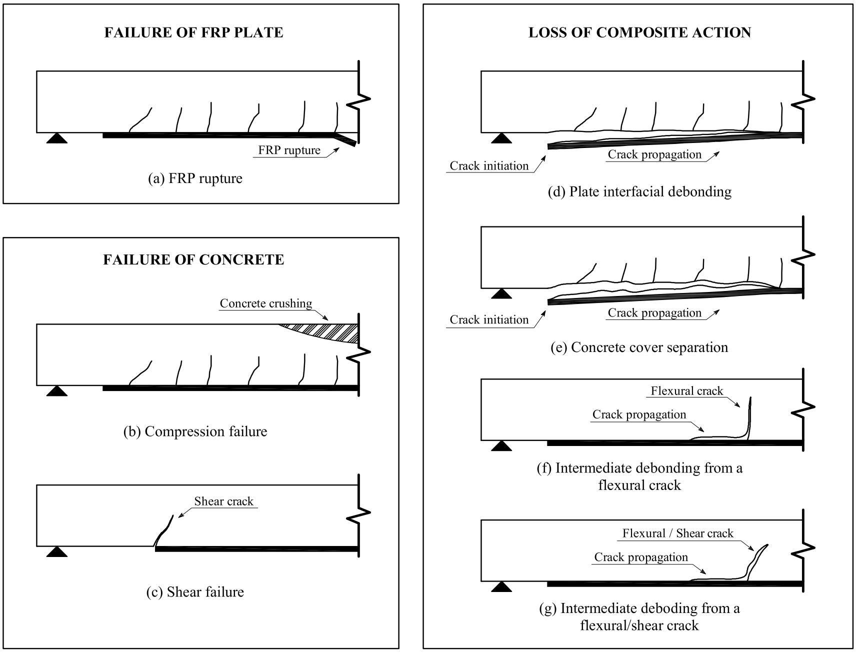
FAILURE OF FRP PLATE
FRP rupture
(a) FRP rupture
FAILURE OF CONCRETE
Concrete crushing
(b) Compression failure
Shear crack
(c) Shear failure
LOSS OF COMPOSITE ACTION
Crack initiation
Crack propagation
(d) Plate interfacial debonding
Crack initiation
Crack propagation
(e) Concrete cover separation
Flexural crack
Crack propagation
(f) Intermediate debonding from a flexural crack
Flexural / Shear crack
Crack propagation
(g) Intermediate deboding from a flexural/shear crack

Figure 2.8: Failure modes of FRP-strengthened RC beams.

Failure modes such as plate-end debonding and intermediate crack-induced debonding are regarded as *local failures*. In these cases, the composite action between concrete and FRP is lost and prevents the strengthened beam from reaching its ultimate flexural capacity due to debonding. Thus, local failures must be considered in design to ensure structural integrity. In general, with reference to the debonding failures, experimental evidence shows that the main failure mode is the cracking of concrete under shear, occurring commonly a few millimeters below the adhesive-concrete interface [6, 16]. Interfacial failure involving the rupture of adhesives is not found, due the availability of strong adhesives that bond well the support and the reinforcement. The experimentally-observed phenomenon is of the type schematized in Figure 2.9.

If the axial stiffness of the reinforcement is high and the bond is strong, the application of an axial pull-out load produces the initiation of cracking from the loaded edge; the crack slightly dives into the substrate and then propagates almost parallel to the interface a few millimeters beneath it, reaching a steady state phase of mode II propagation [17]. In fact, the maximal energy release rate is when

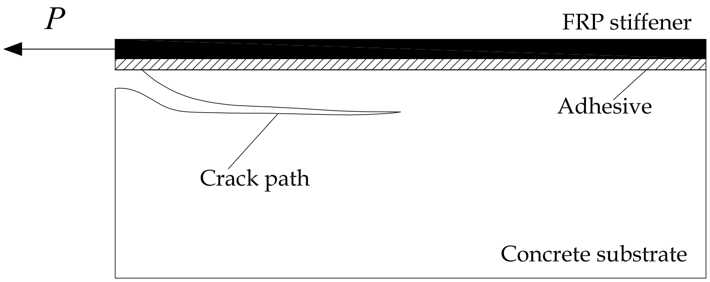

Figure 2.9: Crack propagation in a brittle substrate.

the FRP sheet itself is released. More precisely, a thin layer of the underlying substrate remains attached to the reinforcing stringer, but this layer is so thin that its contribution to the tension stiffening of the stringer is usually neglected: indeed, if this was not the case, the energy release associated with the stringer would be diminished. On the other hand, the contribution due to the glue layer can certainly be neglected due to its infinitesimal thickness. Therefore, a model-problem may consider the pure separation in *mode II* of the stringer from the substrate.

2.3.2 Bond-slip behavior

In order to fully comprehend the behavior of the bonded joint, the experimental tests introduced at the beginning of paragraph 2.3 need to focus on different aspects of the bond mechanism of FRP-to-concrete interface. In the following, a non-extensive list of these aspect is summarized and a reference can be found in [18].

2.3.2.1 Bond strength

Various shear-anchorage-strength models have been proposed to interpret the interfacial debonding mechanism, for which a review can be found in [5, 19]. In general, these models can be classified into three categories: *i*) empirical models based on the regression of test results [6]; *ii*) engineering formulations based upon simplified assumptions and appropriate safety factors [16, 5]; *iii*) Fracture Mechanics Based (FMB) models [20, 9, 21, 22]. Experimental and theoretical studies have shown that there is a certain number of parameters that governs the bond-slip behavior and consequently the ultimate bond-strength of the bonded joint: the concrete strength, in terms of the cylinder compressive strength, f_c' or the average tensile strength, f_{ctm}, the bond length, l, the FRP axial stiffness, $E_s A_s$, the FRP-to-concrete width ratio, b_s/b_p (Figure 2.6). Each model expresses the dependence by these parameters in different ways and a non-exhaustive summary can be found in Table 2.2. In this table, one can find the maximum load that can be achieved by the joint P_u, the effective bond length (see paragraph 2.3.2.2) L_e and the fracture energy of the interface G_f, according to some of the shear-anchorage-strength models present in the literature.

2.3.2.2 Effective bond length

In general, in pull-out tests the axial force in the stiffener is gradually transmitted to the substrate by shear forces acting at the interface. Such forces decay very quickly passing from the loaded end to the free end of the stiffener, so that they can be considered active on a certain length only, usually referred to as the *effective bond length* or the *effective stress transfer length*. In long stiffeners, as the load increases, debonding near the applied load shifts the stress transfer zone to new areas farther away from the loading point, confirming that only part of the bond is active. In other words, the anchorage strength does not increase with an increase of the bond length beyond its active limit. However, a longer bond length may improve the ductility of the failure process due to the gradual translation of the effective length, as debonding proceeds. This phenomenon has been confirmed by many studies on steel-to-concrete [9] and FRP-to-concrete bonded joints [6]. This is a fundamental difference between an externally bonded plate and an internal reinforcing bar for which a sufficiently long anchorage length can always be found so that the full tensile strength of the reinforcement can be achieved. Table 2.2 shows some expressions of the effective bond length according to some models present in the literature.

2.3.2.3 Interface constitutive law

Pull-out tests furnish not only the ultimate load of the FRP-to-concrete interface, but they can be used to build the local bond-slip law of the interface [23, 6, 7, 14, 24, 25], correlating the shear bond-stress τ with the relative slip s of the two adherents. Bond-slip curves are generally obtained in two ways: (a) from axial strains of the FRP plate measured with closely spaced strain gauges [26, 9, 14, 10]; (b) from load-displacement (slip at the loaded end) curves [27].

In the first method, assuming a linear variation of strains between two subsequent strain gauges, the average value of bond stresses is obtained by writing the equilibrium of the portion of plate where the strain gauges are located, while the corresponding slip can be found by a numerical integration of the measured axial strains of the plate. This method appears to be simple but it does not produce accurate bond-slip curves, since it cannot get rid of the experimental uncertainties related to the measurement of the strains, very sensitive to the presence of concrete cracks, to the heterogeneity of concrete and the roughness of the underside of the debonded FRP plate. Consequently, bond-slip curves found from different tests may differ substantially. In the second method, the local bond-slip curve is determined indirectly from the load-slip curve, but it is easy to show that rather different local bond-slip curves may lead to similar load-displacement curves.

A typical response for a FRP/concrete interface is represented by the curve of Figure 2.10(b): after a pseudo-linear branch up to the peak stress τ_f, a strain-softening phase follows, where increasing relative slip results in a decreasing interfacial shear stress transfer along the interface. The shear stress then drops to zero and this is associated with the complete separation of the FRP strip from the concrete substrate. The area under the $\tau - s$ curve represents the *interfacial fracture energy* G_f and can be obtained by integration in the form [29]:

$$G_f = \int \tau ds. \tag{2.3}$$

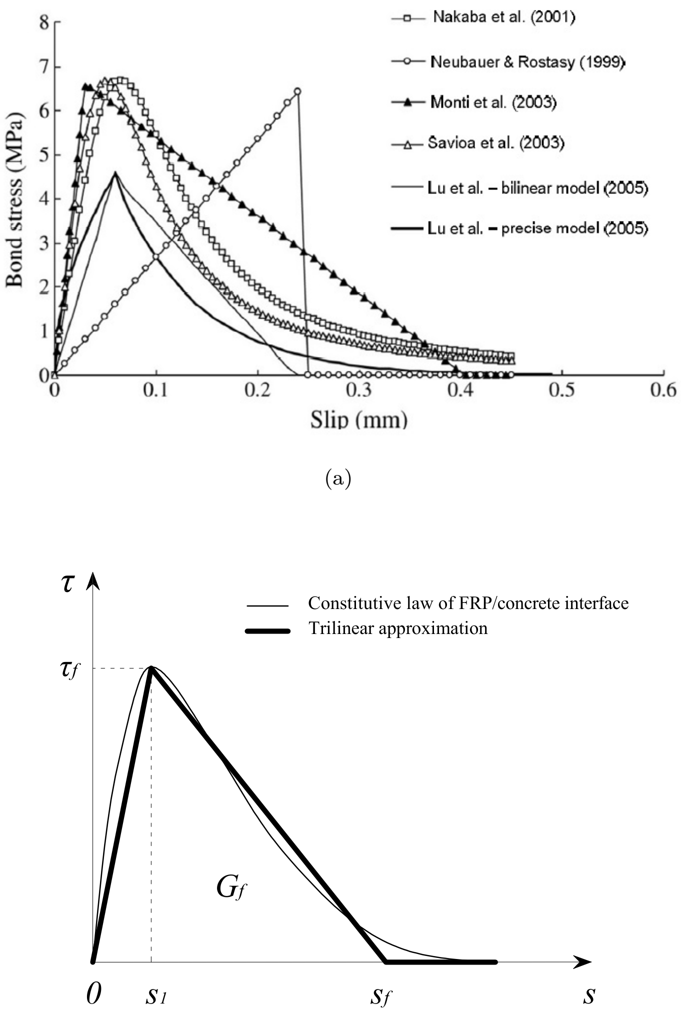

(a)

(b)

Figure 2.10: Shear-stress vs. slip constitutive relationship for FRP-to-concrete: (a) Bond-slip curves from existing bond-slip models [28]; (b) Tri-linear approximations.

Lu *et al.* [28] summarized four existing bond-slip models for an FRP-to-concrete bonded joint, whose curves are shown in Figure 2.10(a). It can be seen that the shapes of the predicted bond-slip curves differ substantially. In particular, the linear-brittle model of Neubauer and Rostasy [30] is very different from the other three models and it is considered unrealistic. Nakaba *et al.* [31] and Savoia *et al.* [32] have shown that the bond-slip curve should have an ascending branch and a descending branch. A bilinear model of bond-slip curve is proposed by Monti *et al.* [33]. Apart from the general shape, the slip at maximum stress and the ultimate slip at zero bond stresses, determine the accuracy of the model. It is interesting to notice that the models by Nakaba *et al.* [31], Monti *et al.* [33] and Savoia *et al.* [32] are in reasonably close agreement, and the linear-brittle model of Neubauer and Rostasy [30] predicts a similar maximum bond stress. Lu *et al.* [28] used another approach to obtain the bond-slip curve of FRP-to-concrete. Their new bond-slip models are not based on axial strain measurements on the FRP plate; instead, they are based on the predictions of a meso-scale finite element model, with appropriate adjustments to match their predictions with the experimental results for a few key parameters. The bond-slip curves proposed by Lu *et al.* [28] (the precise model and the bilinear model) are shown in Figure 2.10(a) as well.

As suggested in recent technical standards [1], a convenient curve can be obtained by approximating the $\tau - s$ interface law with a trilateral (Figure 2.10(b)), formed by a linearly ascending branch up to peak stress τ_f, followed by a linear softening phase approaching the fracture slip s_f where $\tau = 0$ and, finally, a zero-stress *plateau*. The fracture energy per unit-surface is $G_f = \frac{1}{2}\tau_f s_f$ and, in general, such value is made to coincide with the integral of the τ vs. s experimental curve. This equivalence allows to evaluate the limit slip s_f once the peak load τ_f is known and viceversa.

2.4 Analysis of the debonding process

The different-in-type pull tests shown in Figure 2.5 allow to have an insight into the debonding mechanism, triggered by the high shear stress concentrations typically found at the edges of the reinforcement. A direct shear test geometry consists of a stiffener bonded to a substrate, which is restrained from movement and where a longitudinal force is applied at one end of the FRP plate (Figure 2.6). A general configuration of a pull out test is represented in Figure 2.11.

Equally-spaced strain gauges are usually glued on the top of the FRP plate in order to measure longitudinal strains. Linear Variable Differential Transformers (LVDTs) are positioned on both sides of the FRP composite (on the concrete block) to measure the relative displacement of the FRP plate with respect to the concrete support. The test is then conducted applying an increasing load at one extremity of the FRP. Typical results show the actual load plotted against the relative displacement of the FRP, measured by the LVDTs. As shown by various experimental results present in the literature, the load response is initially approximately linear, becomes nonlinear and then levels off and essentially remains constant at a certain critical value of load with increasing global slip up to failure (Figure 2.12).

These results are not able to capture a very important part of the process, that is the snapback following the constant load phase. As a matter of fact, numerical

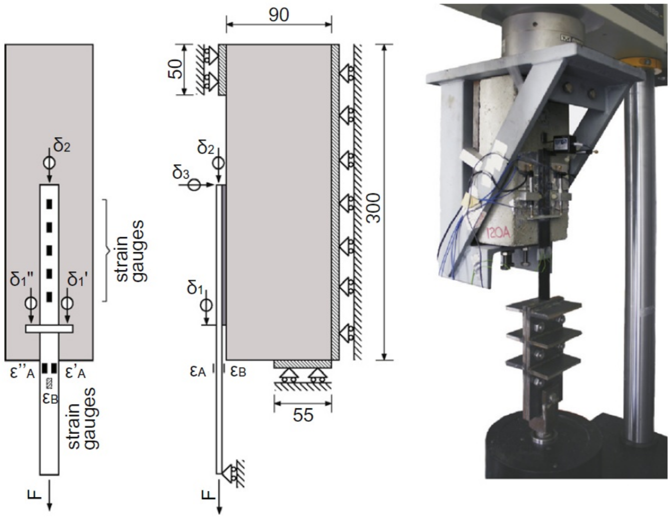

(a) (b)

Figure 2.11: Test setup of the experimental campaign of [12]: (a) Scheme of the specimen with LVDT's and strain gauges applied on the plate and (b) picture of the specimen on the supporting system.

analysis have shown that the behavior of the bonded joint is strongly characterized by the bond length l [23]. "Short" stiffeners show a post-peak softening while "long" stiffeners are characterized by a *plateau*, usually followed by a snapback phase, the more accentuated the higher the bond length is (Figure 2.13).

Scaling in the maximum load has been observed and the maximum load to achieve complete debonding has been experimentally shown to increase with an increase in the bond length until a critical length is reached after which no additional increase in load capacity is possible. We can then conclude that most of the experiments recorded in the technical literature are strain driven tests, which are not able to capture any snap-back response. An exception is the experimental campaign recently performed at the University of Parma by Carrara *et al.* [12], where a closed-loop tensometer was used to control the force P applied at a FRP stiffener glued to concrete specimens, according to the output of LVDT transducers (Figure 2.11). Two different controls were used. Tests were started controlling the load with a certain rate until the displacement measured by the clip-gauge reached its measuring range; successively, the control was switched to the relative sliding of the opposite free end of the stiffener, through a clip gauge. An observation of the experimental test allows to understand the propagation of debonding. Considering for example a bonded length of 150 mm, as long as the FRP stiffener is pulled, the interface crack is observed to initiate in the nonlinear part of the load response. Once the crack initiates in the interface, it grows in a stable manner. At the peak load, a portion of FRP plate close to the applied load is complete detached from the substrate. This debonded zone propagates in a self-similar manner at a constant applied load with an increase of the slip of the reference point, as a consequence

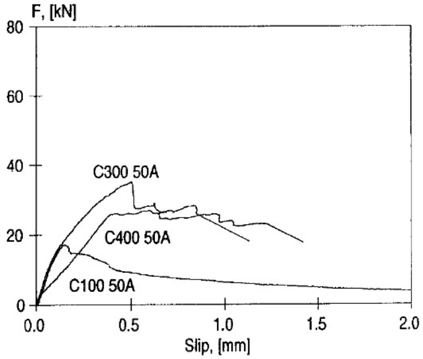

(a) Tests of Täljsten. [9].

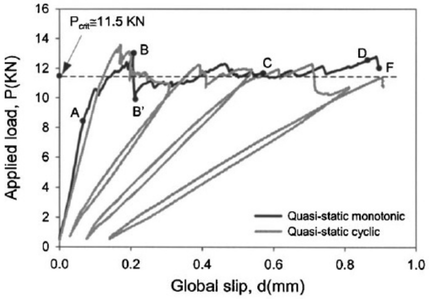

(b) Tests of Ali-Ahmad *et al.* [23]

Figure 2.12: Experimental load-displacement curves for pull-out tests on FRP/concrete bonded joints.

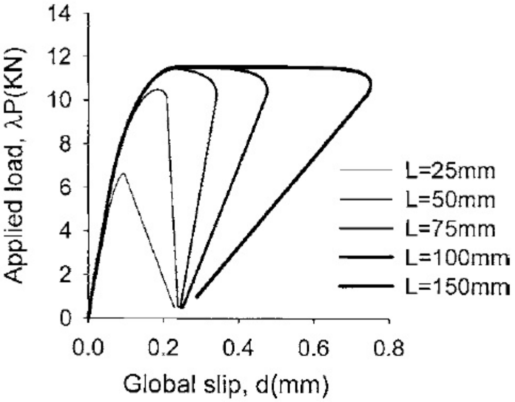

Figure 2.13: Typical load-displacement curves for pull-out tests on FRP/concrete bonded joints for different bond lengths [23].

of the deformation of the part of the FRP that is completely debonded. At a certain point, both the load and displacement decrease simultaneously, producing the phase that is known as *snapback*. The load carrying capacity of the remaining bonded part starts to decrease with additional crack growth. Snapback results due to the elastic unloading of the fully debonded FRP. This phenomenon, which is associated with a sudden release of elastic energy, would result in a catastrophic failure of the bond and becomes more dangerous as the bond length increases. The final failure of the specimen is produced by complete separation of the FRP composite sheet from the concrete substrate and the formation of a concrete bulb at the free end of the reinforcement, whose extension is in general approximately equal to the width of the lamina, and it seems independent from the reinforcement length [34] (Figure 2.14).

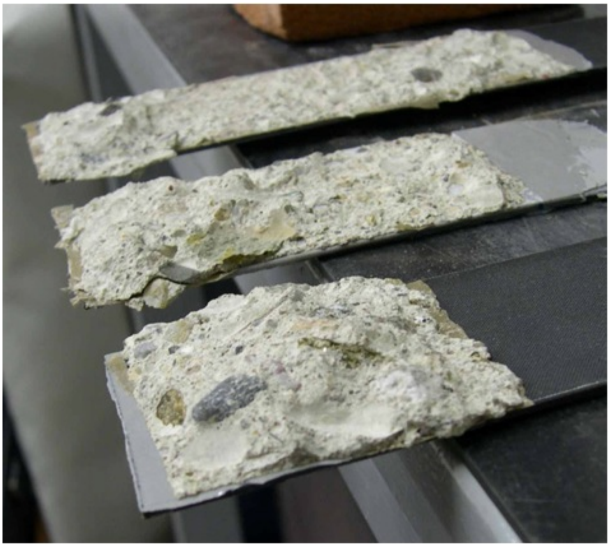

Figure 2.14: Bulbs at FRP free end for different lengths of the reinforcement [34].

2.5 Open problems

To my knowledge, the totality of the *analytical* anchorage-strength models neglects the elastic deformation of the substrate and assumes a shear vs. slip interface constitutive law to describe the entire phenomenon. Whatever the length of the stiffener is, such models predict a fast (usually *exponential*) decay of the transfer shear stress from the loaded-end to the free-end that never reaches the zero value. Since no part of the stiffener is inactive regardless of its length, the definition itself of *effective* bond length needs an engineering interpretation. For example, many researchers define the effective bond length as the bond length over which the shear bond stresses offer a total resistance which is at least 97% of the ultimate load[1] of an *infinite* joint [21, 25, 35, 36]. According to other authors, the evaluation cannot but be purely experimental. Measuring the strain profile in the stiffener - usually employing resistance strain gauges - the effective bond length is the length over which the strain decays from the maximum to the zero value [23, 10, 37, 38, 39, 40]. There are some intrinsic ambiguities in these definitions. In the first case, there is an *a priori*-defined percentage of load and the result strongly depends upon the particular bond-slip constitutive law that is used for the model. For example, Yuan *et al.* [21] and Wu *et al.* [35] studied the influence of the shape of the interfacial constitutive relationships on the load capacity of the bonded joint (Figure 2.15), developing equations for the ultimate load, the interfacial shear stress distribution and the effective bond length. The second definition cannot get rid of the experimental approximations and depends upon the sensitivity of the gauges. In any case, all definitions implicitly assume that the deformation of the substrate is negligible, because the relative displacement between stiffener and substrate is evaluated by simply integrating the axial strain of the stiffener. The hypothesis of rigid substrate is indeed supported by the greatest majority of authors (see also [12, 26, 11]) because it gives drastic simplifications, but it has major drawbacks, such as the implication that the slip is always nonzero whatever the bond length is.

---

[1] Notice that $\tanh 2 \simeq 0.97$: this is a characteristic value in the solution of the differential equations governing the debonding process [21]. Therefore, the limit of 97% seems to be motivated by the analytical approach to the problem, rather than by sound physical considerations.

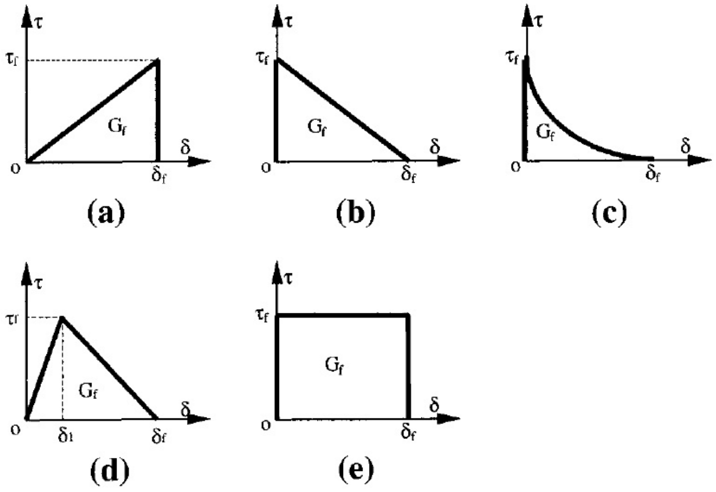

Figure 2.15: Shear-stress vs. slip constitutive relationships for FRP to concrete bonded joints used to develop the anchorage bond strength model of [21].

Moreover, as evidenced in section 2.4, the failure of the bonded joint is characterized by the complete separation of the FRP plate from the support. The duration of this process depends on the bond length of the FRP strip. It is very short or may not be noticed at all for a small bond length, but may be easily seen for long stiffeners. The completely debonded strips evidence the presence of a concrete bulb at the unloaded end [34, 12, 13] (Figure 2.14). A review of the existing literature has evidenced a lack in the description of this phenomenon, which instead it has been proved to be a characteristic part of experimental tests. Biolzi *et al.* [34]

have been able to identify the onset of the bulb formation by comparing the load-stroke and the load-clip curves of the individual tests: when the load drops with a small change in clip-gauge displacement, the Load-Stroke response exhibits an unstable branch (snap-back). In order to detect this phenomenon, Carrara *et al.* [12] applied a LVDT at the free end of the FRP plate to measure the orthogonal displacements between concrete and plate. Their results reveal that the peeling crack appears during the snap-back branch of the load-slip curves. In general, the debonding process starts from the loaded end and, as explained in section 2.4, propagates towards the free end of the stiffener until the energy release rate of the propagating crack is higher than the fracture toughness of the interface. As soon as it approaches the free end, the interface delamination stops and a crack appears at the unloaded end of the stiffener. As the process continues, the final failure is then characterized by the formation of the concrete prism. Starting from the physical observation of the phenomenon, its interpretation through an analytical model will be pursued in the following chapters.

Table 2.2: Shear-anchorage-strength models.

		Ultimate load P_u [N]	**Effective Bond Length** L_e [mm]	**Fracture Energy** G_f [N mm/mm^2]	**Observations**
EMPIRICAL MODELS	Maeda *et al.* [6]	$P_u = 110.2 \cdot 10^{-6} E_s t_s b_s L_e$	$L_e = \exp\left(6.13 - 0.580 \ln\left(E_s t_s\right)\right)$	-	Not valid for $l < L_e$
FMB MODELS	Holzenkämpfer [20]	$P_u = \begin{cases} 0.78 b_s \sqrt{2 G_f E_s t_s}, & l \geq L_e, \\ 0.78 b_s \sqrt{2 G_f E_s t_s \beta_l}, & l < L_e, \end{cases}$	$L_e = \sqrt{\frac{E_s t_s}{4 f_{\text{ctm}}}}$	$G_f = c_f k_p^2 f_{\text{ctm}}$	$\beta_l = \frac{l}{L_e}\left(2 - \frac{l}{L_e}\right)$ f_{ctm} concr. average tensile strength c_f from linear regression analysis $k_p = \sqrt{1.125 \frac{2 - b_s/b_p}{1 + b_s/400}}$
	Täljsten [9]	$P_u = b_s \sqrt{\frac{2 E_s t_s G_f}{1 + \alpha_t}}$	-	-	$\alpha_t = \frac{E_s t_s}{E_p t_p}$
	Yuan [25]	$P_u = \frac{\tau_f b_s}{\lambda_2} \frac{s_f}{s_f - s_1} \sin \lambda_2 a$	$L_e = a_0 + \frac{1}{2\lambda_1} \ln \frac{\lambda_1 + \lambda_2 \tan \lambda_2 a_0}{\lambda_1 - \lambda_2 \tan \lambda_2 a_0}$	-	$a \rightarrow \tan\left[\lambda_1 (l - a)\right] = \frac{\lambda_2}{\lambda_1} \tan \lambda_2 a$ $a_0 = \frac{1}{\lambda_2} \sin^{-1}\left(0.97 \sqrt{\frac{s_f - s_1}{s_f}}\right)$ $\lambda_1^2 = \frac{\tau_f}{s_1 E_s t_s}(1 + \alpha_y)$ $\lambda_2^2 = \frac{\tau_f}{(s_f - s_1) E_s t_s}(1 + \alpha_Y)$ $\alpha_Y = \frac{b_s E_s t_s}{b_p E_p t_p}$
	Neubauer [22]	$P_u = \begin{cases} 0.64 k_p b_s \sqrt{E_s t_s f_{\text{ctm}}}, & l \geq L_e, \\ 0.64 k_p b_s \sqrt{E_s t_s f_{\text{ctm}} \beta_l}, & l < L_e, \end{cases}$	$L_e = \sqrt{\frac{E_s t_s}{2 f_{\text{ctm}}}}$	$G_f = c_f f_{\text{ctm}}$	Valid for FRP and steel plates f_{ctm} concr. average tensile strength $\beta_l = \frac{l}{L_e}\left(2 - \frac{l}{L_e}\right)$ $c_f = 0.0204$ $k_p = \sqrt{1.125 \frac{2 - b_s/b_p}{1 + b_s/400}}$
DESIGN PROP.	Chen and Teng [5]	$P_u = 0.427 \beta_p \beta_l \sqrt{f_c'} b_s L_e$	$L_e = \sqrt{\frac{E_s t_s}{\sqrt{f_c'}}}$	-	$\beta_l = \begin{cases} 1, & l \geq L_e, \\ \sin \frac{\pi l}{2 L_e}, & l < L_e, \end{cases}$ $\beta_p = \sqrt{\frac{2 - b_s/b_p}{1 + b_s/b_p}}$ f_c' concr. cylinder compressive strength
	Van Gemert [16]	$P_u = 0.5 b_s L f_{\text{ctm}}$	-	-	-

CHAPTER 3

THE EFFECT OF THE DEFORMATION OF THE SUBSTRATE

3.1 Introduction

The aim of this chapter is to evaluate the influence of the substrate deformability with reference to the solution of a contact problem in plane linear elasticity, between an elastic stiffener and an elastic substrate supposed in generalized plane stress. Traditionally, from the point of view of applications, the problem has been categorized in two main groups: stiffeners or cover plates mainly used in aircraft structures [41, 42, 43, 44, 45, 46] and thin films used in microelectronics, sensors and actuators [47, 48, 49]. In both fields, the primary interest is the evaluation of stress concentrations or singularities near the edges of the film or the stiffener in order to deepen the question of crack initiation and propagation in the substrate or along the interface. This aspect seems to have been only partially considered for the specific case of civil applications through the use of fiber reinforced polymer composites.

The stress transfer between an elastic stiffener and an elastic plate was firstly studied by Melan in 1932 [45]. By supposing perfect bond between the bodies, both considered infinite, and by treating the fiber as a one dimensional stringer loaded at one end by a longitudinal force, he was able to obtain a closed-form solution. An important result was the unboundedness of the interface tangential stress in the neighborhood of the force application point. This work was then considered and extended by different authors. The problem of a finite stiffener on an infinite plate was treated by Benscoter [42]. He considered the problem of stress transfer under symmetric and anti-symmetric loading and reduced the governing integro-differential equation to a system of linear algebraic equations.

There are two types of approaches to study the problem of debonding from the theoretical treatment standpoint. The first deals with crack initiation by assuming a preexisting crack [50]; the second assumes that the edge delamination occurs due to stress singularities at the edges of the film [47, 51, 49, 52]. Erdogan and Gupta [51] provided one of the earliest and most relevant contributions to thin films, where they solved the problem of an elastic stiffener bonded to a half plane using the membrane assumption. Later, Shield and Kim [49] extended this analysis using the plate assumption for the film, in order to take into account the bending stiffness and the effect of peel stresses, especially near the edges of the film. It was demonstrated that the membrane assumption is still valid when the stiffener thickness is "small" compared to the other dimensions in the system. Freund and Suresh [53] gave a qualitative indication for the thickness of the stiffener, which has to be at least 20 times smaller than the other dimensions to assure a membrane behavior.

In this chapter, the contact problem of an elastic finite stiffener bonded to the boundary of a semi-infinite plate and loaded at one end by a longitudinal concentrated force is considered. A compatibility equation is written that automatically furnishes the integro-differential equation in terms of the tangential stresses between stiffener and plate. An approximate solution is then obtained in term of Chebyshev polynomial, following the approach proposed by Grigolyuk [54], tentatively pursued by Villaggio [55, 56] and probably firstly introduced by Benscoter [42].

I do not consider here the variety of responses that can be obtained under the assumption of cohesive shear fractures *à la* Barenblatt, regulated by an assumed shear stress vs. slip constitutive law. Being interested in the effect of the substrate elasticity, at this stage I consider the minimal model, in which the debonding process is assumed to begin and continue as soon as the energy release rate due to an infinitesimal crack growth equals the interfacial fracture energy (Griffith balance). The evaluation of the energy release rate due to a propagating interface crack does not seem to have been correctly considered by previous contributions [56]. This is why I analyze here in detail the extension to this particular problem of the *Crack Closure Integral Method* developed by Irwin [57]. This energetic balance is then used to derive the maximum load as a function of the bond length, provided that the specific fracture energy is known. Moreover, one can reproduce a pull out test, following step by step the corresponding interface-crack path.

A parametric study has been conducted in order to evaluate the load vs. displacement curves predicted by this model, which are compared with careful experimental data obtained from recent direct tensile tests [12]. Despite the simplicity of the Griffith energetic balance, the analytical results are in good agreement with the experimental pull-out curves for high bond length, being able to reproduce, at least at the qualitative level, their typical trend. This is characterized by a *plateau*, during which debonding occurs, followed by a snap-back phase, related to the release of the strain energy stored by the FRP stringer during the delamination process. The latter was obtained with a closed loop control of the crack opening in the detaching stringer [12].

3.2 Load transfer from an elastic stiffener to a semi-infinite plate

Suppose that an elastic stiffener of constant width b_s and (small) thickness t_s is bonded to the boundary of an elastic semi-infinite plate in generalized plane stress over the interval $[0, l]$, considered with respect to the ξ-axis of the Cartesian system shown in Figure 3.1. At one end, the stiffener is loaded by a longitudinal force P, which represents the resultant of the normal stress on the cross sectional area. Since t_s is small, the bending strength of the stiffener is negligible, so that its normal component of the contact stress with the semi-plane may be neglected. The state of stress in the stiffener is then uni-axial, due to P and the tangential contact stresses transmitted by the plate.

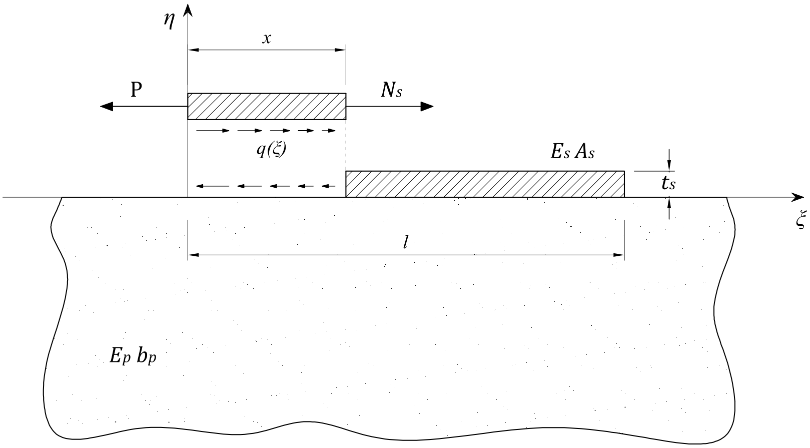

Figure 3.1: A finite stiffener bonded to the boundary of a semi-infinite plate.

Equilibrium for that part of the stiffener comprised between the origin and a section $\xi = x$ allows to write the axial force $N_s(x)$ in the form

$$N_s(x) = P - \int_0^x q(\xi)\, d\xi\,, \tag{3.1}$$

where $q(\xi)$ is the contact tangential force per unity length. By Hooke's law, the stiffener strain reads

$$\varepsilon_s(x) = \frac{N_s(x)}{E_s A_s} = \frac{1}{E_s A_s}\left[P - \int_0^x q(\xi)\, d\xi\right], \tag{3.2}$$

where E_s is its elastic modulus and A_s its cross sectional area. Besides, on the boundary of the semi-plane, the strain in the interval $[0, l]$ due to the tangential contact stress may be written in the form [54]

$$\varepsilon_p(x) = -\frac{2}{\pi E_p b_p}\int_0^l \frac{q(\xi)}{\xi - x}\, d\xi\,, \tag{3.3}$$

where E_p is the elastic modulus of the plate and b_p its width. Since the strains must be equal over the interval of contact, equating (3.2) and (3.3) one obtains the singular integral equation

$$\frac{1}{E_s A_s}\left[P - \int_0^x q(\xi)\, d\xi\right] = -\frac{2}{\pi E_p b_p}\int_0^l \frac{q(\xi)}{\xi - x}\, d\xi. \tag{3.4}$$

Introducing the rigidity parameter λ, defined as

$$\lambda = \frac{2}{\pi}\frac{E_p b_p l}{E_s A_s}, \tag{3.5}$$

and the dimensionless coordinate $\tau = \xi/l$, equation (3.4) can be written in the form

$$\int_0^1 \frac{q(\tau)}{\tau - \tau_0}\,d\tau = -\frac{\pi^2\lambda}{4}\left[\frac{P}{l} - \int_0^{\tau_0} q(\tau)\,d\tau\right], \tag{3.6}$$

which has to be solved under the equilibrium condition

$$l\int_0^1 q(\tau)\,d\tau = P. \tag{3.7}$$

An approximate solution for (3.6) can be obtained by expressing the contact force q in term of a series of Chebyshev polynomials [54, 51, 58]. Chebyshev terms are orthogonal in the interval $[-1, 1]$, so that it is convenient to make the change of variable

$$t = 2\tau - 1\,,$$

so that conditions (3.6) and (3.7) become, respectively,

$$\int_{-1}^1 \frac{q(t)}{t - t_0}\,dt = -\frac{\pi^2\lambda}{8}\left[\frac{2P}{l} - \int_{-1}^{t_0} q(t)\,dt\right], \tag{3.8}$$

$$l\int_{-1}^1 q(t)\,dt = 2P\,. \tag{3.9}$$

The approximate solution of (3.8) can be sought in the form of an expansion in Chebyshev polynomials of the first kind $T_s(t)$ defined as

$$q(t) = \frac{2P}{\pi l\sqrt{1-t^2}}\sum_{s=0}^{n} X_s T_s(t)\,, \tag{3.10}$$

where X_s are constants to be determined. Observe that there is a square-root singularity in the solution at both ends of the reinforcement, which is typical of most contact problems in linear elasticity theory; the strength of the singularity is determined by all terms of the series. Substituting (3.10) into condition (3.9) and recalling the orthogonality conditions of the Chebyshev polynomials of the first kind (see Appendix, eq. (A.4)), one obtains that

$$X_0 = 1.$$

Moreover, substitution of the expansion (3.10) in (3.8) allows to determine, after integration, the other constants X_s by means of the Bubnov method [54]. The final result is a set of algebraic equations for X_j of the type

$$X_j + \frac{\lambda}{4}\sum_{s=1}^{n} a_{js}X_s = -\frac{\lambda}{4}b_j\,, \qquad \text{for } j = 1, 2, ..., n \tag{3.11}$$

where

$$\begin{cases} a_{js} = -\frac{4j}{[(j+s)^2-1][(j-s)^2-1]}, & \text{for even } j - s, \\ a_{js} = 0, & \text{for odd } j - s, \end{cases}$$

and

$$\begin{cases} b_1 = \frac{\pi^2}{4}, & \\ b_j = -\frac{4j}{(j^2-1)^2}, & \text{for even } j, \\ b_j = 0, & \text{for odd } j \neq 1. \end{cases}$$

Solving the system of algebraic equations (3.11), it is immediate to determine the X_j and hence $q(t)$. It may be seen that in the neighborhood of $t = \pm 1$, the contact problem for the stiffener/plate gives a singularity analogous to a crack problem under pure Mode II loading conditions. Therefore, one can define the Mode II stress intensity factor at $\xi = 0$ $(t = -1)$ in the form

$$K_{II} = \lim_{\xi \to 0} q(\xi)\sqrt{2\pi\xi}. \tag{3.12}$$

Substitution of the contact stress (3.10) into (3.12) gives the expression

$$K_{II} = \frac{2P}{\sqrt{2\pi l}}\sum_{s=0}^{n} X_s(-1)^s\,, \tag{3.13}$$

which represents the governing parameter for the problem at hand.

3.3 Energetic balance

Linear elastic fracture mechanics (LEFM) is based upon an energetic balance *à la* Griffith between the strain energy release rate and the increase in surface energy.

3.3.1 Generalization of the *Crack Closure Integral Method* by Irwin

For the problem at hand, let us consider the case of an elastic stringer bonded for a length l to an elastic plate in generalized plane stress. The stringer is pulled by a force P in the configurations sketched in Figure 3.2, referred to as the sound state.

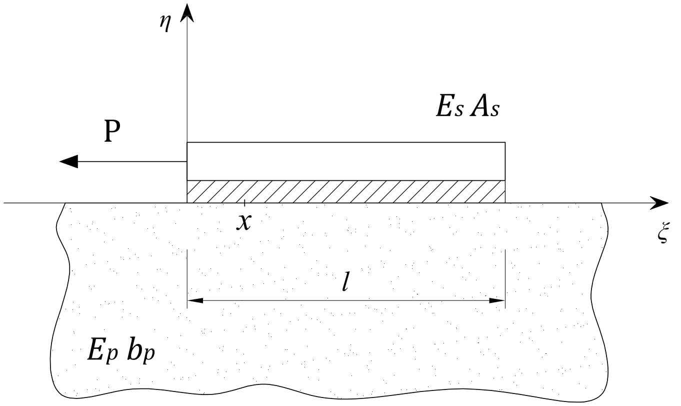

Figure 3.2: Sound state: stiffener bonded for a length l upon an elastic plate.

Let us consider another configuration, i.e., the debonded state represented in Figure 3.3, in which delamination has occurred over a portion of length c. A reference system (ξ, η) is introduced with the origin on the left-hand-side border of the stringer, so that the bonded portion is $c \leq \xi \leq l$. The composite body is loaded by two system of forces. System I is the force P^I appended at the stringer left-hand-side border, while system II is composed of forces per-unit-length $q^{II}(\xi)$, representing a mutual interaction stress between plate and stringer (Figure 3.3). Let $u_s^I(\xi)$ $(u_s^{II}(\xi))$ represent the displacement of the stringer in the positive $\xi-$axis direction of the stringer due to system I (II) of forces, and let $u_p^I(\xi)$ $(u_p^{II}(\xi))$ be the corresponding displacement of the plate, again associated with system I (II). In the following, quantities referred to system I or II will be labeled with the I or II apex, respectively.

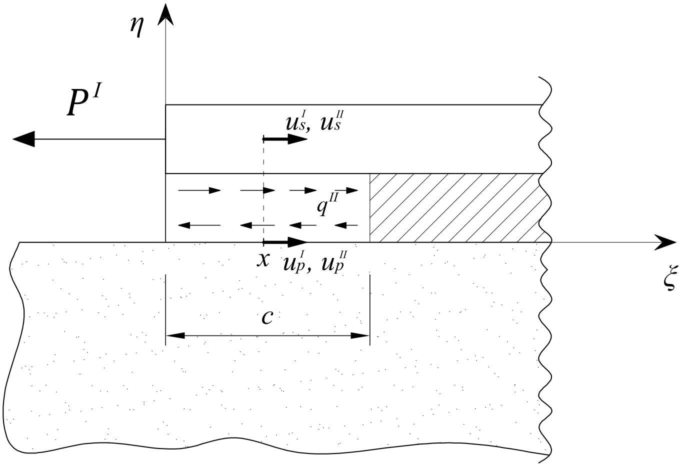

Figure 3.3: Debonded state, where delamination has occurred on a portion of length c.

By Clapeyron theorem, the elastic strain energy U^I due to the action of system I reads

$$U^I = -\frac{1}{2}P^I u_s^I(0)\,. \tag{3.14}$$

The strain energy $U^{(I+II)}$, associated with system $I + II$, is of the form

$$\begin{aligned} U^{I+II} &= -\frac{1}{2}P^I u_s^I(0) + \frac{1}{2}\int_0^c q^{II}(\xi)[u_s^{II}(\xi) - u_p^{II}(\xi)]d\xi + \int_0^c q^{II}(\xi)[u_s^I(\xi) - u_p^I(\xi)]d\xi \\ &= -\frac{1}{2}P^I u_s^I(0) + \frac{1}{2}\int_0^c q^{II}(\xi)\{[u_s^I(\xi) + u_s^{II}(\xi)] - [u_p^I(\xi) + u_p^{II}(\xi)]\}d\xi \quad (3.15) \\ &\quad +\frac{1}{2}\int_0^c q^{II}(\xi)[u_s^I(\xi) - u_p^I(\xi)]d\xi\,. \end{aligned}$$

Let us then assume that $P^I = P$ and that $q^{II}(\xi)$ represent the contact bonding forces for the sound state of Figure 3.2. Since in this case the portion $0 \leq \xi \leq c$ is perfectly bonded, one has that

$$[u_s^I(\xi) + u_s^{II}(\xi)] - [u_p^I(\xi) + u_p^{II}(\xi)] = 0\,, \tag{3.16}$$

and consequently, from (3.14) and (3.15), one finds

$$\Delta U = U^{I+II} - U^I = \frac{1}{2}\int_0^c q^{II}(\xi)[u_s^I(\xi) - u_p^I(\xi)]d\xi\,. \tag{3.17}$$

Here ΔU represents the difference of the strain energy between the sound state and the debonded one. Obviously, the variation of the total energy ΔE equals $-\Delta U$. The latest expression represents the extension to this case of the *Crack Closure Integral Method* developed by Irwin [57].

3.3.2 Strain energy release rate

With the same notation of Section 3.2, indicating with Γ the surface fracture energy and with b_s the width of the stiffener, energetic balance states that

$$\Gamma\, b_s = \lim_{c\to 0}\frac{d}{dc}\Delta U = -\lim_{c\to 0}\frac{d}{dc}\Delta E = G\,, \tag{3.18}$$

where G denotes the strain energy release rate.
Substituting expression (3.17) in the relation (3.18), the problem reduces to the evaluation of G, i.e.,

$$G = \lim_{c\to 0}\frac{d}{dc}\left[\frac{1}{2}\int_0^c q^{II}(\xi)\,\{u_s^I(\xi) - u_p^I(\xi)\}d\xi\right] = \lim_{c\to 0}\frac{d}{dc}\left[\frac{1}{2}\int_0^c q^{II}(\xi)\, u_{rel}^I(\xi)d\xi\right], \tag{3.19}$$

where it has been posed $u^I_{rel} = u^I_s - u^I_p$. By using Leibniz's rule for differentiation under the integral sign, the preceding expression becomes

$$G = \lim_{c\to 0}\left\{\frac{1}{2}q^{II}(c)\,u^I_{rel}(c) + \frac{1}{2}\int_0^c q^{II}(\xi)\,\frac{\partial}{\partial c}u^I_{rel}(\xi)\,d\xi\right\}. \tag{3.20}$$

The first term is null because there is no relative displacement for $\xi = c$, since at this point the stiffener is still bonded to the plate. As regards to the second term, denoting with ε^I_s the axial strain in the stiffener, and with ε^I_p the normal strain component in the ξ direction of the plate, observe that

$$\begin{aligned}\frac{\partial}{\partial c}u^I_{rel}(\xi) &= \frac{\partial}{\partial c}\left[\int_\xi^c \varepsilon^I_s(\zeta)\,d\zeta\right] - \frac{\partial}{\partial c}\left[\int_\xi^c \varepsilon^I_p(\zeta)\,d\zeta\right]\\ &= \varepsilon^I_s(c) - \frac{\partial}{\partial c}\left[\int_\xi^c \varepsilon^I_p(\zeta)\,d\zeta\right].\end{aligned} \tag{3.21}$$

Consider first the term containing ε^I_p, i.e., the one associated with the strain in the plate. Referring to Figure 3.3, the strain needs to be evaluated at points that are external to the interval $[c, l]$, where stiffener and plate are bonded. The elastic solution for a plate reinforced by a stringer of length $l - c$ can be obtained with the same method described in Section 3.2. With reference to equation (3.3), let us introduce the new variable

$$t = \frac{2\xi - l - c}{l - c}.$$

Solving the elastic problem in terms of the new variable t, from equation (3.3), one obtains

$$\varepsilon^I_p(t_0) = -\frac{4P}{\pi^2 E_p b_p (l-c)}\sum_{s=0}^{n} X_s \int_{-1}^{1}\frac{T_s(t)}{\sqrt{1-t^2}\,(t-t_0)}dt\,, \tag{3.22}$$

where $t_0 = (2\xi_0 - l - c)/(l - c)$. The integral can be evaluated by using the property of Chebyshev polynomials reported in Appendix (eq. (A.6)), with reference to the case $|t_0| > 1$. The final result is

$$\varepsilon^I_p(t_0) = -\frac{4P}{\pi E_p b_p (l-c)}\sum_{s=0}^{n} X_s \frac{(t_0 + \sqrt{t_0^2 - 1})^s}{\sqrt{t_0^2 - 1}}\,, \tag{3.23}$$

and therefore the displacement reduces to

$$
\begin{aligned}
u_p^I(t_0) &= \int_{t_0}^{-1} \varepsilon_p^I(t)dt = -\frac{4P}{\pi E_p b_p (l-c)} \sum_{s=0}^{n} X_s \int_{t_0}^{-1} \frac{(t+\sqrt{t^2-1})^s}{\sqrt{t^2-1}} \frac{l-c}{2}\, dt \\
&= -\frac{2P}{\pi E_p b_p} \sum_{s=0}^{n} \frac{X_s}{s} \left[(-1)^s - \left(t_0 + \sqrt{t_0^2-1} \right)^s \right].
\end{aligned}
\tag{3.24}
$$

Written in term of ξ, using a Taylor expansion in a neighborhood of $\xi = c$, (3.24) reads

$$
u_p^I(\xi) = -\frac{2P}{\pi E_p b_p} \sum_{s=0}^{n} X_s (-1)^s 2 \sqrt{\frac{c-\xi}{l-c}}\,. \tag{3.25}
$$

Consequently, the derivative of the displacement with respect to the interfacial crack length c is

$$
\frac{\partial}{\partial c} u_p^I(\xi) = -\frac{2P}{\pi E_p b_p} \sum_{s=0}^{n} X_s (-1)^s \frac{(l-\xi)}{(l-c)\sqrt{(c-\xi)(l-c)}}\,. \tag{3.26}
$$

The contact stresses $q^{II}(\xi)$ are given by (3.10) and can also be expanded in Taylor's series in neighborhood of $\xi = 0$ to obtain

$$
q^{II}(\xi) = \frac{P}{\pi} \sum_{s=0}^{n} X_s \cos(\pi s) \left[\frac{1}{\sqrt{\xi}\sqrt{l}} - \frac{2s^2\sqrt{\xi}}{l\sqrt{l}} \right]. \tag{3.27}
$$

Therefore, the strain energy release rate G can be evaluated substituting (3.26) in (3.21) and the result, together with (3.27), in the second term of (3.20). After integration, one obtains the expression

$$
G = \lim_{c\to 0} \frac{1}{2} \varepsilon_s^I(c) \int_0^c q^{II}(\xi)\; d\xi + \frac{P^2}{\pi E_p b_p l} \left[\sum_{s=0}^{n} X_s (-1)^s \right]^2. \tag{3.28}
$$

But the first term of (3.28) is null, because the contact stress $q^{II}(\xi)$ of (3.27) has a square-root singularity in a neighborhood of $\xi = 0$ so that for $c \to 0$ the integral vanishes[2]. Consequently, one finds the general expression for the energy release rate G in the form

---

[2] Indeed, one can demonstrate that when $E_p \to \infty$ (rigid substrate) $q^{II}(\xi)$ tends to become a Dirac distribution centered at $\xi = 0$, so that the integral does not vanish when $c \to 0$. Here I consider the elastic solution for $E_p < \infty$ and will show later on that when $E_p \to \infty$ the second term of (3.28) tends to the energy release rate associated with the problem of an elastic stiffener on a rigid substrate. This fact does not seem to have been recognized in [56], where the expression proposed is not correct.

$$G = \frac{P^2}{\pi E_p b_p l} \left[\sum_{s=0}^{n} X_s (-1)^s \right]^2 . \tag{3.29}$$

Recalling the expression of Mode II stress intensity factor given by (3.13), the expression (3.29) can be re-written in the form

$$G = \frac{K_{II}^2}{2 E_p b_p} . \tag{3.30}$$

Equation (3.30) plays a key role since it bridges the energetic approach with the stress analysis. Remarkably, it is similar to Irwin's relationship between the strain energy release rate and the stress intensity factor. To my knowledge, the method used to derive the strain energy release rate in the context of plane elasticity has never been stated up to now. As a matter of fact, common ways to evaluate G are based on the J-integral [59].

The expression (3.30) is particularly important because the stress intensity factor K_{II} can also be evaluated numerically[3], without resorting to the Chebyshev expansion. The energetic balance detailed in Section 3.3.3 thus allows to calculate the maximum tensile load P once the fracture energy of the bond is known.

3.3.3 Energetic balance

Suppose that the toughness of the bonded joint is defined by the fracture energy per unit area Γ_F. Then, energetic balance *à la* Griffith implies that the crack propagates when

$$G = \Gamma_F b_s , \tag{3.31}$$

where b_s is the width of the stiffener. Then, from (3.29), one finds that the critical value P_{cr} of P reads

$$P_{cr} = \sqrt{\Gamma_F b_s \frac{\pi E_p b_p l}{\left[\sum_{s=0}^{n} X_s (-1)^s\right]^2}} . \tag{3.32}$$

Apparently P_{cr} depends upon the elasticity of the substrate only, because the elasticity of the stiffener is not explicitly involved in the expression (3.29) of G. But it should be noticed that the terms of the Chebyshev expansion strongly depend upon the mechanical properties of the stiffener through the rigidity parameter λ, defined in (3.5).

To illustrate, it is useful to consider directly the limit condition $E_p = \infty$, i.e., the case of a rigid substrate. A simple calculation indicates that the energy release rate takes the form

---

[3] Most numerical codes evaluate the stress intensity factor using the J-integral.

$$G_r = \frac{P^2}{2E_s A_s}\,, \tag{3.33}$$

which is the same expression derived by Taljsten in [60], for a general linear and non-linear interface law with reference to a pure shear bond-slip model, and by Wu *et al.* in [35], for a bilinear interface law.
Figure 3.4 shows the ratio G/G_r, with G evaluated through (3.30) and G_r through (3.33), as a function of the bond length l for values of E_p/E_s ranging from 0.01 to 100. Notice that $G \to G_r$ as $l \to \infty$, and the limit value is attained more quickly as E_p/E_s increases, i.e., as the substrate tends to become rigid.

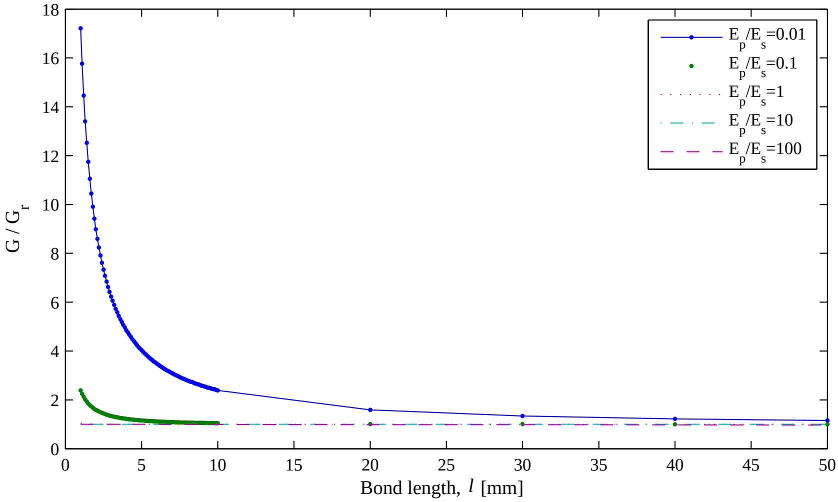

Figure 3.4: Normalized strain energy release rate G/G_r for different values of the ratio E_p/E_s.

Moreover, as shown more in detail in Figure 3.5, *for short bond lengths the value of the energy release rate may be much higher than the value associated with the case of rigid substrate.* From (3.31), this means that *short stiffeners* may detach at *much lower load levels* than *long stiffeners.* This effect is entirely due to the elasticity of the substrate, because if the substrate is rigid then G_r is given by (3.33), which is independent of the length of the stringer.
It is important at this point to quantify the meaning of “short” and “long” stiffeners. Recall that terms X_s defining the Chebyshev expansion only depend upon the non-dimensional parameter λ of (3.5). Figure 3.6 shows the ratio G/G_r now as a function of λ: obviously the graphs obtained in Figures 3.4 and 3.5 for varying E_p/E_s collapse into one curve (for convenience of representation, the scale for λ is now logarithmic). It is then quite evident that the transition between the case of a *soft* elastic substrate to the case of a *rigid* substrate is marked by a value $\lambda = \lambda^*$ that can be estimated of the order $\lambda^* \simeq 10^1$. But since the stringer length

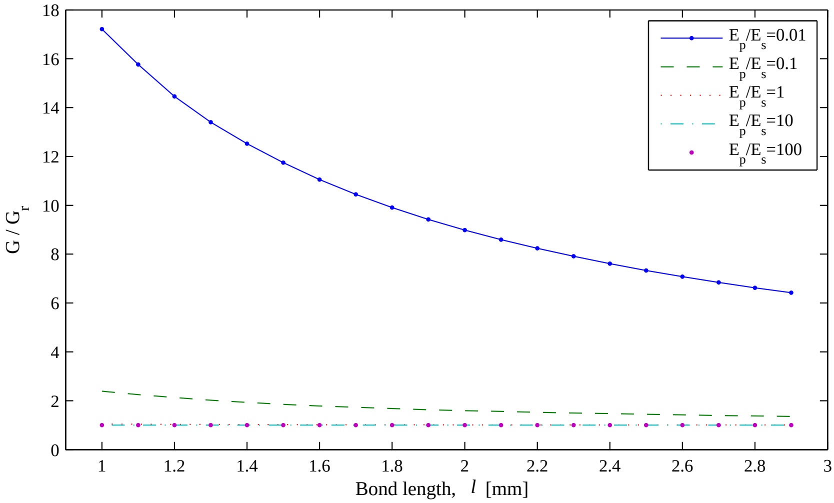

Figure 3.5: Normalized strain energy release rate G/G_r for different values of the ratio E_p/E_s. Detail for small bond lengths l.

l enters in the definition (3.5) of λ, the "rigidity" of the substrate does not depend upon its elastic modulus only. In other words, it is λ that represents the similarity parameter: the case $\lambda \gg \lambda^*$ ($\lambda \ll \lambda^*$) is associated with long (short) stiffeners and rigid (soft) substrates.

The presence of a step change in the distribution of contact stress along the stiffener bond length is also evident in the logarithmic plot of Figure 3.7, where ξ denotes again the distance from the stringer edge where the load P is applied. As $\xi \to 0$, the slope of the curves equals to $-1/2$ because of the typical square root singularity. The graphs tend to a vertical asymptote when approaching the second edge of the stringer, where another stress singularity occurs (the various graphs refer to different bond lengths). The slope of the graphs changes for a value of ξ comprised between 10^0 and 10^1. This transition value should not be confused with the anchorage length, i.e., the minimum length assuring maximum anchoring force. In fact, there are stress singularities at both edges of the stiffener, so that the axial strain in the stiffener is never zero. This is a characteristic feature (and perhaps a limitation) of this model.

Figure 3.8 represents, as a function of ξ, the normalized axial load N_s/P calculated as *per* (3.1), for two different value of the substrate elastic modulus E_p. The continuous lines may be associated with a typical reinforcement on a concrete support, whereas the dashed lines refer to the case of a substrate ten times more deformable (elastic modulus one tenth of the previous one). From the graphs it is evident that the softer the substrate, the higher is the length that is necessary to transfer the load from the stringer.

It should also be mentioned that, in order to achieve a good approximation, the number n of Chebyshev terms that are needed in the series (3.29) to define G, strongly increases as E_p/E_s increases, i.e., as the substrate becomes stiffer and

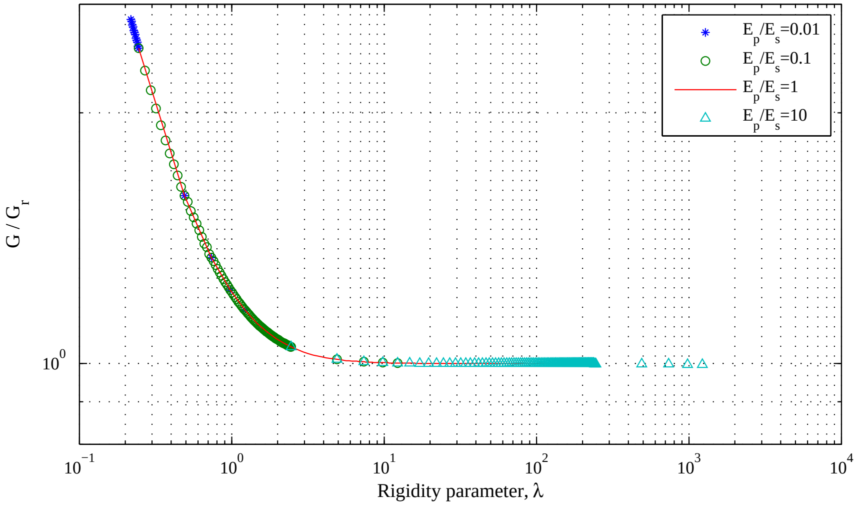

Figure 3.6: Normalized strain energy release rate G/G_r as function of the rigidity parameter λ for different values of the ratio E_p/E_s.

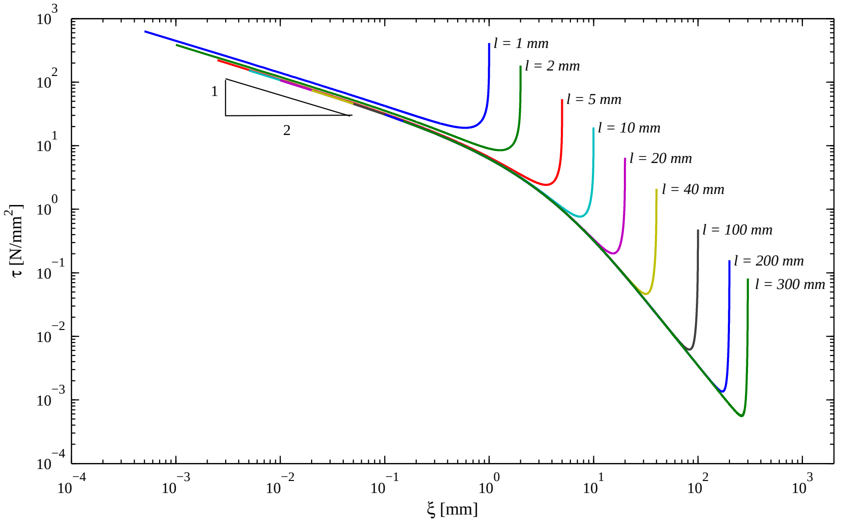

Figure 3.7: Interfacial shear stress along the stiffener for different bond lengths l.

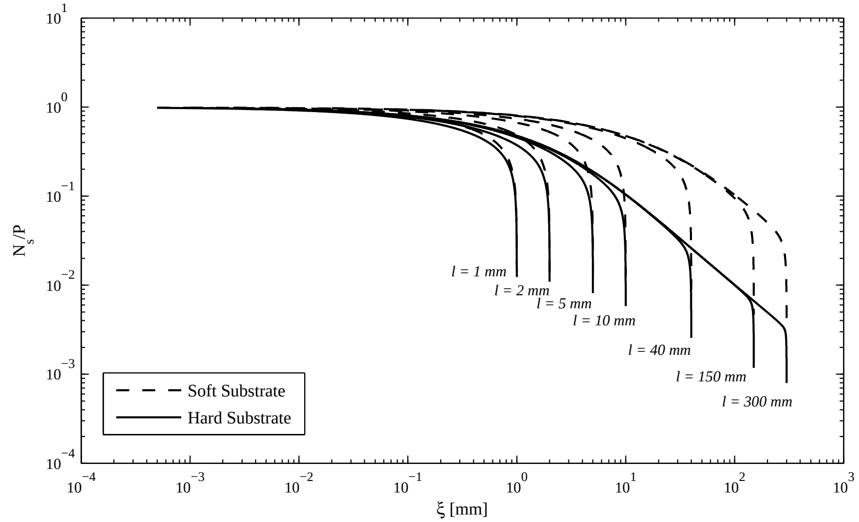

Figure 3.8: Distribution of the normalized longitudinal force in the stiffener, N_s, for two different values of the substrate elasticity and different values of the bond length l. For each pairs of curves, the continuous line is for a typical concrete substrate, whereas and the dashed line is for a substrate ten times softer.

stiffer. This fact is shown in Figure 3.9, which refers to cases when $\lambda \gg \lambda^*$ (rigid substrate) and represents the ratio G/G_r as a function of n for varying E_p/E_s. Observe that when $E_p/E_s = 0.1$ just a few terms are sufficient to obtain a good approximation, but when $E_p/E_s = 1000$, more than one thousands terms are necessary. This remark is useful to indicate a suitable value for n in the case of a typical concrete/FRP stiffness ratio. Since for this case $E_p/E_s \simeq 0.1 \div 0.2$, one finds in Figure 3.9 that the curve of interest lays between the curves $E_p/E_s = 0.1$ and $E_p/E_s = 1$, for which $n \simeq 100$ can be considered appropriate.

3.4 Comparison with experiments

Expression (3.32) allows to calculate the critical tensile load $P = P_{cr}$ in the stiffener as a function of the geometric and mechanical parameters, in particular the fracture energy Γ_F. In general, there may be two distinct failure mechanisms: *i*) failure in the thin glue layer or *ii*) failure in the neighboring layer of the substrate. In the first case, Γ_F represents the fracture energy of the glued interface, whereas in the second case it is the (mode II) fracture energy of the substrate.

One of the most common applications certainly consists in the strengthening of concrete with Carbon Fiber Reinforced Polymers (CFRP). In most of the tests recorded in the technical literature, fracture occurs through the shearing of a thin concrete layer underneath the CFRP plate. Thus, one can assume that Γ_F is the concrete fracture energy, for which the relation proposed by Italian technical recommendations [1], also accepted at the European Community level, is of the

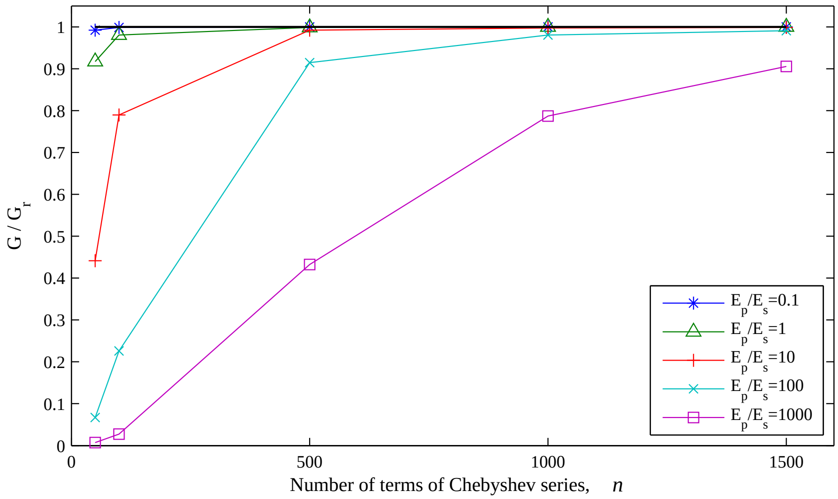

Figure 3.9: Case $\lambda \gg \lambda^*$ (rigid substrate). Normalized strain energy release rate G/G_r as a function of the number n of terms in the Chebyshev series for different values of the ratio E_p/E_s.

form

$$\Gamma_F = \frac{1}{2} s_f \kappa_a \kappa_b \sqrt{f_{ck} f_{ctm}}\,. \tag{3.34}$$

Here s_f is the maximum slip, associated with an assumed bilinear shear-stress vs. relative-slip constitutive relationship, usually taken equal to 0.2 mm; f_{ck} and f_{ctm} are the characteristic compression strength and the mean tensile strength of concrete; κ_a is a value calculated on the basis of a statistical analysis of experimental data, for which 0.64 represents an average value; κ_b is a geometric parameter that depends upon the stiffener width b_s and substrate width b_p, that takes the form

$$\kappa_b = \sqrt{\frac{2 - \frac{b_s}{b_p}}{1 + \frac{b_s}{400[\mathrm{mm}]}}} \geq 1\,, \tag{3.35}$$

when $b_s/b_p \geq 0.33$ (when $b_s/b_p < 0.33$, assume $b_s/b_p = 0.33$).

In this study the results of a series of pull tests on CFRP-to-concrete bonded joints collected from the existing literature are considered. The fundamental problem is the evaluation of the critical load which can be transmitted to the reinforcement before debonding occurs.

Experimental evidence suggests that, in general, crack propagation due to debonding occurs approximately at a constant load. The model predicts this response in the case of “long” strips. In fact, when the parameter λ of (3.5) exceeds the threshold value $\lambda^* \simeq 10^1$, Figure 3.6 shows that the energy release rate G is almost constant and equal to the value G_r of (3.33) for the rigid support. The energetic balance (3.31) thus furnishes the value

$$P_{cr,r} = \sqrt{2E_sA_s\Gamma_F b_s} = b_s\sqrt{2E_st_s\Gamma_F}\,, \tag{3.36}$$

which coincides with the expression suggested by most technical standards. Debonding of the stiffener occurs when $P \simeq P_{cr,r} =$ const. as long as $\lambda \gg \lambda^*$, i.e., when the bonding length l is sufficiently high. When $\lambda \ll \lambda^*$, one understands from Figure 3.6 that the energy release rate becomes much higher than G_r and consequently P_{cr} results much lower than $P_{cr,r}$.

In summary, “long” stiffeners progressively detach from the support, until the bond length becomes so small that equilibrium can only be attained provided that the pull out load P is decreased. This decay provokes an elastic release in that part of the stiffener that has already debonded from the substrate and is strained by P. The main consequence of this is that, after a *plateau*, pull out tests on long strip should exhibit a *snap-back* phase.

Most of the pull-out tests considered in the technical literature are strain-driven tests that cannot capture any snap back response. An exception is the experimental campaign recently performed in the laboratories of the University of Parma by [12], who used a closed-loop tensometer to control the pull-out-force P from the output of LVDT transducers, placed at the non-loaded end of the stringer, i.e., at point $\xi = l$ in the scheme of Figure 3.2. Among other tests, recorded in [12], concrete prisms of 150 × 90 × 300 mm nominal size were reinforced by pultred CFRP plates 30 mm wide and 1.3 mm thick. The measured mechanical properties of the materials used in the tests are reported in Table 3.1.

Table 3.1: Mechanical properties of materials used for the tests of [12]

	Concrete	**FRP**	**Adhesive**
Young’s Modulus, E [MPa]	28700	168500	3517.3
Poisson’s Ratio, ν	0.2	0.248	0.315
Tensile Strength, f_t [MPa]	3.2	-	12.01
Average Compression Strength, f_c [MPa]	37.2	-	-

The results of the pull-out experiments are summarized in the graphs of Figure 3.10, reporting the load P as a function of Δ, i.e., the measured displacement at the point of application of P. What should be noticed here is the marked snap-back response, which occurs approximately when $\Delta = 0.30 \div 0.35$ mm.

In order to compare this results according to the prediction of the proposed model, parameter calibration has to be performed. The critical load is evaluated through (3.32), where the Chebyshev coefficients X_s depend upon the parameter λ of (3.5).

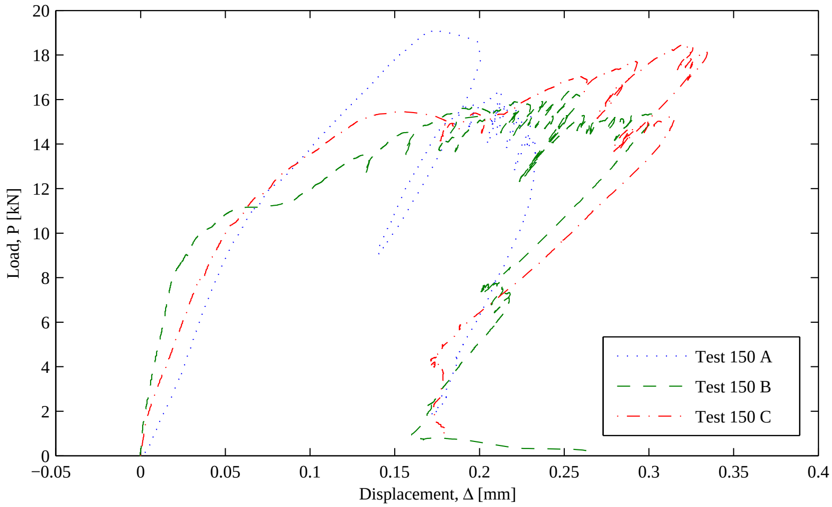

Figure 3.10: Load P vs. displacement Δ curves for the pull-out tests of [12]. Initial bond length $l = 150$ mm.

Material parameters are taken from Table 3.1. The geometry of the stiffener is known, but attention should be paid in the evaluation of b_p. The proposed model is two-dimensional and consequently is accurate only when $b_p/b_s \simeq 1$. For the case at hand $b_p/b_s = 5$ and the hypothesis of plate in generalized plane stress is questionable. A technical solution can be found through the following argument. Recalling from Figure 3.6 that the decrease of load P occurs at $\lambda = \lambda^* \simeq 10^1$, one can measure from experiments [12] what is the bond length l^* that is associated with the beginning of the decay of the tensile strength. By using (3.5), the effective width b_p^* can be evaluated as

$$b_p^* = \frac{\pi}{2}\lambda^* \frac{E_s t_s b_s}{E_p(l^*)} = \alpha^*\, b_s. \qquad (3.37)$$

For the experiments of Figure 3.10 the value $l^* \simeq 60$ mm has been measured [12], from which $\alpha^* \simeq 2.0$ and $b_p^* \simeq= 60$ mm.
The results are shown in Figure 3.11, which represents the experimental force vs. displacement curves juxtaposed with that obtained through the model. There is a good estimate of the *plateau* associated with stable debonding. Moreover, the model can also predict the *snap-back* phenomenon: that part of the CFRP stiffener already detached from the substrate is strained by the applied load that, when released, causes its contraction. In the theoretical curve, the bond length calculated through the model are evidenced by labeled dots: bigger circles are at multiples of 10 mm, whereas smaller dots are for lengths multiple of 1 mm. Notice that material softening starts approximately in the fourth quarter of the *plateau*, when the bond strength is about 60 mm, even if the decay is just appreciable at the scale of resolution of the graph. Remarkably, when the snap-back branch

starts, the bond length rapidly diminishes. This is a phase governed by an abrupt phenomenon, whose experimental evaluation needs appropriate feed-back controls. It must also be mentioned that the value of the fracture energy Γ_F that has been used in the relevant expressions is that obtained by integrating the $P - \Delta$ curves of Figure 3.10, i.e., $\Gamma_F \simeq 0.57$ N/mm. Such a value is much lower that obtainable with the expression (3.34), which would give $\Gamma_F = 0.77$ N/mm.

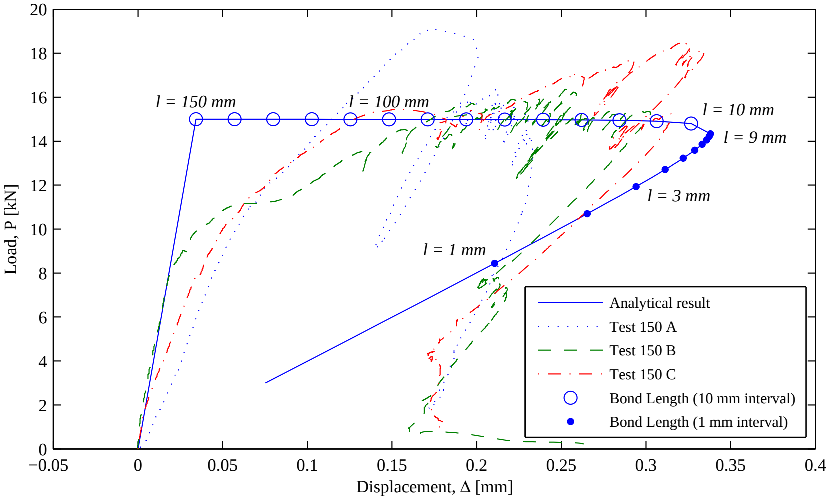

Figure 3.11: Load vs. displacement curves: comparison between theoretical and experimental [12] results. In the theoretical curve, bond lengths l are evidenced by dots (bigger dots for l multiple of 10 mm, smaller dots for l multiple of 1 mm).

There are however some aspects that the model is not able to capture, such as the strain-hardening trend evidenced by the experimental data. This finding may be ascribed to an increase in surface toughness as the crack propagates, a phenomenon observed in quasi-brittle materials such as concrete. Quasi brittle materials exhibit an extensive microcracking in a limited area, known as the fracture *process zone*. Whereas in ductile fracture of metals the fracture process zone is negligible in size when compared to the non linear plastic-hardening zone, in a quasi-brittle material the process zone is larger than the plastic hardening zone. Microcracking affects the behavior of the material and results in an apparent increase of toughness, described through the well-known rising *R-curve* (crack Resistance curve). Fracture energy cannot be considered constant with crack growth as in the case of a flat R-curve typical of ideally brittle materials [61]: then, the driving force due to P must increase to maintain crack growth.

Another aspect is that the predicted slope of the snap-back branch is lower than the one measured through experiments. There is little uncertainty about this, because the occurrence of the snap-back phase is associated with the release of elastic strain energy in the stringer whose geometry and mechanical properties are perfectly known. In the theoretical model the final deformation of the stiffener tends to the null value, because no detachment is assumed from the substrate matrix; on the other hand, the experimental curves of Figure 3.10 highlight a permanent displacement of the stiffener. Consequently, other phenomena such as residual cohesion, inelastic slip, or friction between the detached surfaces, must be considered for a deeper characterization of the phenomenon.

3.5 Discussion

An analytical model has been presented for the description of the interfacial debonding failure of an elastic stiffener from a substrate, in view to practical applications such as the characterization of reinforcements with Fiber Reinforced Polymers (FRP). The contact problem is analyzed under the hypotheses that the bending stiffness of the stringer is negligible and the substrate is a linear elastic semi-infinite plate in generalized plane stress. Compatibility conditions for the relative displacement allow to obtain an integral equation in terms of the tangential stresses [54]. A solution with Chebyshev polynomials can then be used to establish an energetic balance *à la* Griffith, providing the maximum transmissible load. In order to determine the energy release rate, a generalization of the *Crack Closure Integral Method* developed by Irwin [57] has been detailed.

Results of the calculations show that the strain energy release rate strongly depends upon the elasticity of the substrate, tending to the limit value for a rigid substrate calculated by Taljsten [60] when the Young modulus of the substrate, E_p, tends to ∞. In general, a soft substrate influences the fracture propagation process and, consequently, the diffusion of the load. The qualitative properties of the solution depend upon a coefficient λ, defined in (3.5), which represents a non-dimensional similarity parameter providing a synthesis of all those physical variables that influence the phenomenon, such as elastic moduli of stiffener and substrate, geometry and bond length. The substrate can be considered rigid when $\lambda \gg \lambda^*$, where λ^* is of the order of 10^1. Clearly λ is directly proportional to the substrate modulus E_p, but remarkably λ also depends linearly upon the bond length l. Consequently, the substrate can be considered rigid when, left aside all the other material properties, the length of the stringer is sufficiently high.

In other words, “long” (“short”) stringers are those for which $\lambda \gg \lambda^*$ ($\lambda \ll \lambda^*$). In “long” stringers, the elasticity of the substrate does not influence the strain energy release rate (case of rigid substrate), so that energetic balance predicts a gradual detachment at approximately constant pull-out force. In “short” stringers, the contribution from the substrate is important: the lower the bond length, the higher the strain energy release rate. Short stringers thus exhibit a strain softening response.

In a load history when the relative displacement of the stringer is controlled in a closed loop testing machine, such as in the experiments of [12], the stringer gradually debonds from the substrate at approximately constant load, until the bond length becomes so small that the equilibrium load decreases. Release of strain energy in the elastic stringer results in typical load vs. displacement snap-back response, that has been experimentally verified. Results obtained through the model are in good quantitative agreement with the experimental results of [12], provided that the fracture energy considered in the formulas is the one experimentally measured through integration of load-displacement curve.

The model just presented may be considered minimal, because it only relies upon an energetic Griffith balance for the description of the debonding phenomenon. One of the major drawbacks of this assumption is that the diffusion of the load from the stringer to the substrate only depends upon the elasticity of the material: stress singularities occur at both ends of the adherent interface, so that it is difficult to give a consistent definition of the effective anchorage length. However, despite its simplicity, the model is able to capture the maximum transmissible load, the progression of the debonding phenomenon as well as the onset of a snap-back phase, remarking the important role played by the elasticity of the substrate, which is usually neglected in the practice. In order to provide a more accurate description, it would be necessary to slightly complicate the model, taking into account for the possibility of cohesive sliding before final detachment through the assumption of a proper shear-stress vs. slip constitute law at the interface. This is the subject of the next chapters.

CHAPTER 4

THE ROLE OF COHESIVE INTERFACE FORCES

4.1 Introduction

In the previous chapter, the case of a perfectly-adherent stiffener has been considered, focusing the attention on the debonding process assumed to begin, and continue, as soon as the energy release rate due to an infinitesimal delamination becomes equal to the interfacial fracture energy (Griffith balance) [62]. The main drawback of this approach was the difficulty to give a consistent definition of the *effective* anchorage length. In fact, when slip is not contemplated, the presence of the stress singularities at both ends of the stiffener produces a very rapid decay of the shear stress profile at the interface, which does not agree with experiments.

This chapter aims at solving this inconsistency by introducing a cohesive zone where slippage can occur. Following the approach originally proposed by Barenblatt [63], also pursued by other authors [64, 49] for similar-in-type problems, the length of the cohesive zone for a fixed load is evaluated by imposing that the stress intensity factor at the end of the bonded zone is null, eliminating the singularities which are predicted by the theory of elasticity. Effective material separation is supposed to start when the relative slip exceeds a certain threshold. If the stiffener is sufficiently long, there is a maximal reachable length of the cohesive zone: in a strain-driven pull out test, the cohesive portion simply translates along the stiffener as debonding proceeds, maintaining its length unchanged, while the load remains practically constant. A strain softening phase, usually associated with snap-back, is entered when the cohesive zone reaches the free end of the stiffener.

The present model provides a natural, physically-motivated definition of the effective bond length, since it is associated with the maximal length of the cohesive zone reached in sufficiently long stiffeners. Assuming a very simple, step-wise, shear-stress vs. slip constitutive law for the interface, the model is able to interpret the debonding process step-by-step, evidencing different-in-type responses when the bond length is higher, or lower, than the effective bond length. The response is characterized in terms of load-displacement curves that, despite the simplicity of the model, are in excellent agreement with experimental data drawn from the technical literature.

4.2 Adhesion of an elastic stiffener to an elastic substrate

The contact problem of an elastic stiffener of finite length bonded to the boundary of an elastic semi-infinite plate and pulled at one end by a coaxial load is governed by a singular integral equation involving the unknown tangential contact forces [54]. If no slippage occurs between stiffener and plate, the theory of elasticity predicts that interface shear forces have a singularity at both ends of the stiffener. In order to remove this physically-inconsistency, two cohesive zones are introduced at both edges of the reinforcement. The length of these zones depends upon the applied load, and can be found from condition that interface forces are finite in the whole bond, according to the same rationale followed by Barenblatt in the theory of cohesive cracks [63]. In section 4.2.1 the resulting system of singular integral equations is solved through a Chebyshev expansion, while sections 4.2.2 and 4.2.3 recover the solutions of one cohesive zone and no cohesive zone (perfect bond) (the latter seen in Chapter 3) as limit cases.

4.2.1 Double-Cohesive-Zone (DCZ) model

Consider an elastic stiffener of length l, thickness t_s and constant width b_s, bonded to the boundary of an elastic semi-infinite plate in generalized plane stress of width b_p (Figure 4.1). At one end, the stiffener is loaded by a coaxial concentrated force P. As indicated in Figure 4.1, let c_1 and c_2 denote the length of the cohesive zones at the left-hand-side and at the right-hand-side extremities of the stringer, respectively. A reference system (ξ, η) is introduced with the origin on the left-hand-side edge, so that the loaded-end cohesive zone is $0 \leq \xi \leq c_1$ and the free-end cohesive zone is $l - c_2 \leq \xi \leq l$, while the perfectly bonded part is the interval $c_1 \leq \xi \leq l - c_2$.

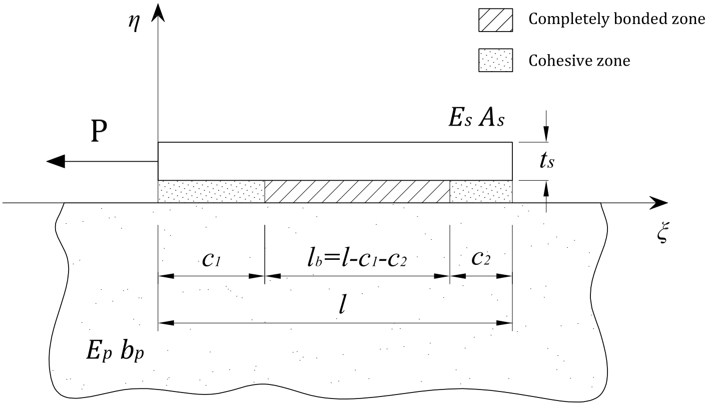

Figure 4.1: A finite stiffener bonded to the boundary of a semi-infinite plate with cohesive zones at both ends.

With reference to the free-body diagram of Figure 4.2, let $q_c(\xi)$ be the (cohesive) tangential force per unit length acting over the length c_1 and c_2, while $q(\xi)$ the contact tangential force per unit length in the bonded portion. The stiffener strain can be obtained through Hooke's law, from the equilibrium of that part of

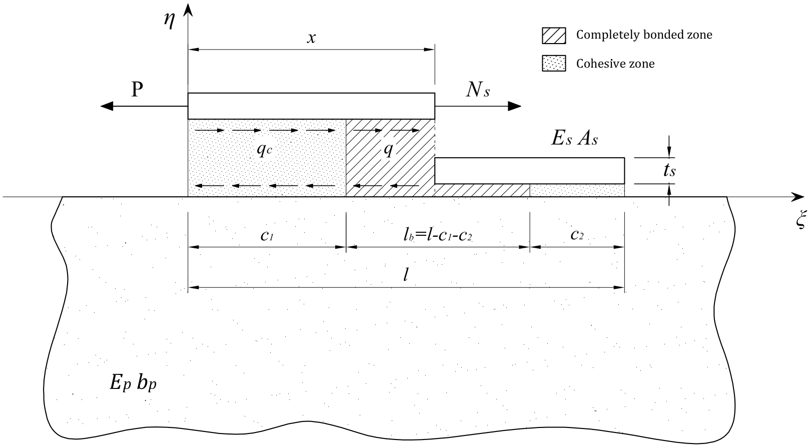

Figure 4.2: A finite stiffener bonded to the boundary of a semi-infinite plate. Free body diagram of a portion of the stiffener.

the stiffener comprised between the origin and a section $\xi = x$, in the form

$$\varepsilon_s(x) = \frac{N_s(x)}{E_s A_s} = \frac{1}{E_s A_s}\left[P - \int_0^{c_1} q_c(\xi)\, d\xi - \int_{c_1}^{x} q(\xi)\, d\xi\right], \tag{4.1}$$

where E_s is the elastic modulus of the stiffener and A_s its cross sectional area. Besides, on the boundary of the semi-infinite plate, the strain in the interval $[0, l]$ due to the cohesive stress and to the tangential contact stress may be written as [54]

$$\varepsilon_p(x) = -\frac{2}{\pi E_p b_p}\left[\int_0^{c_1} \frac{q_c(\xi)}{\xi - x}\, d\xi + \int_{c_1}^{l-c_2} \frac{q(\xi)}{\xi - x}\, d\xi + \int_{l-c_2}^{l} \frac{q_c(\xi)}{\xi - x}\, d\xi\right], \tag{4.2}$$

where E_p is the elastic modulus of the plate and b_p its width.
One obtains the singular integral equation that solves the problem by imposing that strains are equal over the perfectly-bonded interval. In the simplest case one may assume that the cohesive forces are constant, i.e., $q_c(\xi) = const. = q_c$. Consequently, by equating (4.1) and (4.2) and introducing the dimensionless coordinate t in such a way that the completely bonded zone is the interval $[-1, 1]$, that is

$$t = 2\frac{(\xi - c_1)}{(l - c_1 - c_2)} - 1 \Longleftrightarrow \xi = \frac{(l - c_1 - c_2)}{2}(t + 1) + c_1, \tag{4.3}$$

one finds

$$q_c\left[\ln\left|\frac{t_0 + 1}{t_0 + a}\right| + \ln\left|\frac{t_0 - b}{t_0 - 1}\right|\right] + \int_{-1}^{1} \frac{q(t)}{t - t_0}\, dt = -\frac{\pi^2 \lambda}{8}\left[\frac{2(P - q_c c_1)}{l_b} - \int_{-1}^{t_0} q(t)\, dt\right], \tag{4.4}$$

where λ is the rigidity parameter, which reads

$$\lambda = \frac{2}{\pi}\frac{E_p b_p l_b}{E_s A_s}, \tag{4.5}$$

having defined

$$\begin{aligned} l_b &= l - c_1 - c_2, \\ a &= (l_b + 2c_1)/l_b, \\ b &= (l_b + 2c_2)/l_b. \end{aligned} \tag{4.6}$$

Solution to equation (4.4) is subject to the equilibrium condition for the stiffener

$$\int_{-1}^{1} q(t)\, dt = \frac{2(P - q_c c_1 - q_c c_2)}{l_b}\,. \tag{4.7}$$

An approximate solution for (4.4) can be obtained by expanding the contact force q in term of a series of Chebyshev polynomials[4] [54, 51, 58], which are orthogonal in the interval $[-1, 1]$, i.e,

$$q(t) = \frac{2Q}{\pi l_b \sqrt{1-t^2}} \sum_{s=0}^{n} X_s T_s(t)\,, \tag{4.8}$$

where $T_s(t)$ are the Chebyshev polynomials of the first kind [54], X_s are constants to be determined and, for simplicity of notation, I have set $Q = P - q_c c_1 - q_c c_2$. Observe that there is a square-root singularity in the solution at both ends of the reinforcement, which is typical of most contact problems in linear elasticity theory. Following Bubnov's method [54], with a procedure similar to that of section 3.2, substitution of (4.8) into conditions (4.7) and (4.4) allows to obtain, with the orthogonality conditions for Chebyshev polynomials of the first kind (see Appendix A),

$$X_0 = 1,$$

and the system of linear equations

$$X_j + \frac{\lambda}{4}\sum_{s=1}^{n} a_{js} X_s = -\frac{\lambda}{4} b_j - \frac{\pi \lambda q_c c_2}{4Q} c_j - \frac{q_c l_b}{\pi Q} d_j\,, \qquad \text{for } j = 1, 2, ..., n\,. \tag{4.9}$$

---

[4] The main properties of Chebyshev polynomials are reported in Appendix A.

Here

$$
\begin{aligned}
a_{js} &= 1/s \int_{-1}^{1} U_{j-1}(t) U_{s-1}(t)(1-t^2)\, dt, \\
b_j &= \int_{-1}^{1} U_{j-1}(t)\sqrt{1-t^2}\arccos t\, dt, \\
c_j &= \int_{-1}^{1} U_{j-1}(t)\sqrt{1-t^2}\, dt, \\
d_j &= \int_{-1}^{1} U_{j-1}(t)\sqrt{1-t^2}\, \left[\ln\left|\frac{t+1}{t+a}\right| + \ln\left|\frac{t-b}{t-1}\right|\right]\, dt,
\end{aligned}
$$

being $U_j(t)$ the Chebyshev polynomials of the second kind [54]. These expressions can be evaluated with the change of variable $t = \cos\varphi$, so that $U_{j-1}(t(\varphi)) = \sin j\varphi / \sin\varphi$. In conclusion, one finds

$$
\begin{cases}
a_{js} = -\frac{4j}{[(j+s)^2-1][(j-s)^2-1]}, & \text{for even } j-s, \\
a_{js} = 0, & \text{for odd } j-s,
\end{cases}
$$

$$
\begin{cases}
b_1 = \frac{\pi^2}{4}, \\
b_j = -\frac{4j}{(j^2-1)^2}, & \text{for even } j, \\
b_j = 0, & \text{for odd } j \neq 1.
\end{cases}
$$

$$
\begin{cases}
c_1 = \frac{\pi}{2}, \\
c_j = 0, \quad \text{for } j = 2, 3, .., n,
\end{cases}
$$

and

$$
\begin{cases}
d_1 = \frac{\pi}{2}\left\{\left[a\left(\sqrt{a^2-1}-a\right) - \ln\left|a+\sqrt{a^2-1}\right|\right] - \left[b\left(\sqrt{b^2-1}-b\right) - \ln\left|b+\sqrt{b^2-1}\right|\right]\right\}, \\
d_j = \dfrac{\pi}{2}\left[\dfrac{2(-1)^j}{j^2-1} - \dfrac{(\sqrt{a^2-1}-a)^{j+1}}{j+1} + \dfrac{(\sqrt{a^2-1}-a)^{j-1}}{j-1}\right] \\
\qquad + \dfrac{\pi}{2}(-1)^j\left[\dfrac{2(-1)^j}{j^2-1} - \dfrac{(\sqrt{b^2-1}-b)^{j+1}}{j+1} + \dfrac{(\sqrt{b^2-1}-b)^{j-1}}{j-1}\right], \quad \text{for } j = 2, 3, .., n.
\end{cases}
$$

The parameters c_1 and c_2 add to the other n unknowns X_s, so that there are $n+2$ unknowns for the n equations (4.9). Other two conditions need to be introduced, and these are accomplished by imposing that in $\xi = c_1$ $(t = -1)$ and in $\xi = l - c_2$ $(t = 1)$ the shear stress must be finite, or, equivalently, that the mode II stress intensity factors K_{II} are null. The resulting conditions become

$$\begin{cases} K_{\text{II,load}} = \lim\limits_{\xi \to c_1} q(\xi)\sqrt{2\pi(\xi - c_1)} = 0, \\ K_{\text{II,free}} = \lim\limits_{\xi \to l-c_2} q(\xi)\sqrt{2\pi(\xi - l + c_2)} = 0. \end{cases} \tag{4.10}$$

where the subscripts "*load*" and "*free*" refer to the loaded end and the free end of the bonded part of the stiffener, respectively. Substitution of the contact forces (4.8) into (4.10) gives the expressions

$$\begin{cases} K_{\text{II,load}} = \frac{2Q}{\sqrt{2\pi l_b}} \sum\limits_{s=0}^{n} X_s(-1)^s \,, \\ K_{\text{II,free}} = \frac{2Q}{\sqrt{2\pi l_b}} \sum\limits_{s=0}^{n} X_s \,. \end{cases} \tag{4.11}$$

which reduce to the conditions

$$\begin{cases} \sum\limits_{s=0}^{n} X_s(-1)^s = 0 \,, \\ \sum\limits_{s=0}^{n} X_s = 0 \,. \end{cases} \tag{4.12}$$

under the requirement that, of course, $l_b > 0$. This is the adaptation to the contact problem of the approach originally proposed by Barenblatt [63] to eliminate the stress singularity predicted by the elasticity theory in an opening crack, as a consequence of cohesive forces acting at its tip. Conditions (4.12) allow to evaluate the length of the zones over which tangential slippage can occur at the interface, provided that the cohesive stress q_c is known.

4.2.2 Single-Cohesive-Zone (SCZ) model

This model can be considered a limit case of the DCZ approach when the cohesive zone at the free end c_2 is null. Setting for simplicity $c_1 = c$ (Figure 4.3 B), this Single Cohesive Zone (SCZ) model is governed by the set of algebraic equations

$$X_j + \frac{\lambda}{4}\sum_{s=1}^{n} a_{js}X_s = -\frac{\lambda}{4}b_j - \frac{q_c l_b}{\pi Q}d_j \,, \qquad \text{for } j = 1, 2, ..., n \,, \tag{4.13}$$

where $l_b = l - c_1 = l - c$, $Q = P - q_c c_1 = P - q_c c$ and λ has the same expression of (3.5). The coefficients of (4.13) are

$$\begin{aligned} a_{js} &= 1/s \int_{-1}^{1} U_{j-1}(t) U_{s-1}(t)(1-t^2)\, dt, \\ b_j &= \int_{-1}^{1} U_{j-1}(t)\sqrt{1-t^2} \arccos t \, dt, \\ d_j &= \int_{-1}^{1} U_{j-1}(t)\sqrt{1-t^2}\, \ln\left|\frac{t+1}{t+a}\right| dt. \end{aligned}$$

From equation (4.6), one has $b = 1$ and $a = (l+c)/(l-c)$. Therefore, with the change of variable $t = \cos\varphi$ and the representation for the Chebyshev polynomials of the second kind U_{j-1}, one finds

$$\begin{cases} a_{js} = -\frac{4j}{[(j+s)^2-1][(j-s)^2-1]}, & \text{for even } j-s, \\ a_{js} = 0, & \text{for odd } j-s, \end{cases}$$

$$\begin{cases} b_1 = \frac{\pi^2}{4}, \\ b_j = -\frac{4j}{(j^2-1)^2}, & \text{for even } j, \\ b_j = 0, & \text{for odd } j \neq 1, \end{cases}$$

and

$$\begin{cases} d_1 = \dfrac{\pi}{2}\left[1 - a^2 + a\sqrt{a^2-1} - \ln(a+\sqrt{a^2-1})\right], \\ d_j = \dfrac{\pi}{2}\left[\dfrac{2(-1)^j}{j^2-1} - \dfrac{(\sqrt{a^2-1}-a)^{j+1}}{j+1} + \dfrac{(\sqrt{a^2-1}-a)^{j-1}}{j-1}\right], & \text{for } j = 2,3,..,n. \end{cases}$$

It is evident how the second term of the right-hand side of equation (4.9) disappears, because it was associated with the cohesive length c_2. The expression of the coefficient d_j results substantially simplified. In this case, the parameter c adds to the other n unknowns X_s, so that there are $n+1$ unknowns for the n equations (4.13). The condition to be introduced is the annihilation of the mode II stress intensity factor K_{II} in $\xi = c$ $(t = -1)$, that is

$$K_{\mathrm{II,load}} = \lim_{\xi \to c} q(\xi)\sqrt{2\pi(\xi - c)} = 0, \tag{4.14}$$

which reduces, after substitution of the contact stress (3.10) into (4.14) and simplification, to the first condition of equation (4.12) under the condition that, of course, $l_b = l - c > 0$.

4.2.3 No-Cohesive-Zone (NCZ) model

When at the interface between stiffener and substrate no cohesive zone exists, i.e. $c_1 = c_2 = 0$, one has (Figure 4.3 A):

$$X_j + \frac{\lambda}{4}\sum_{s=1}^{n} a_{js}X_s = -\frac{\lambda}{4}b_j\,, \qquad \text{for } j = 1, 2, ..., n \tag{4.15}$$

which is the solution of an elastic stiffener bonded to the boundary of an elastic semi-infinite plate [54], just analyzed in section 3.2. Hereinafter, this will be referred to as the No-Cohesive Zone (NCZ) model. In this case the coefficients c_j and d_j of equations (4.13) and (4.15) disappear, because there is no more dependence by the cohesive zone size, while the coefficients a_{js} and b_j have the same expression of sections 4.2.1 and 4.2.2. In this case, the rigidity parameter λ involves the entire bond length, i.e. $l_b = l$, and reads

$$\lambda = \frac{2}{\pi}\frac{E_p b_p l}{E_s A_s}, \tag{4.16}$$

The solution of (4.15) presents singularities at both ends of the reinforcement, which are typical of most contact problems in the linear theory of elasticity.

4.3 Analysis of the debonding process

In order to give an insight on the debonding process, reference will be made to the case of a single cohesive zone (SCZ model). It will be demonstrated later on in section 4.4 that the influence of the singularity at the free end of the stiffener is almost negligible, since the load balanced by the second cohesive zone is very low and the contact shear stress profile of the DCZ model coincides with that of the SCZ model, giving in practice identical results in terms of bond strength and effective bond length. For this reason, in order to avoid much more complicated calculations, the analysis will be done on the simple SCZ model, even if results would be similar if one considered the more refined DCZ model.

4.3.1 Constitutive law for the cohesive interface

Any adhesive junction is characterized by an interface constitutive law, correlating the shear bond-stress τ with the relative slip s of the two adherents through the adhesive. In general, the $\tau - s$ curve is evaluated by measuring experimentally the strain in the stiffener and the substrate, as done e.g. in [23]. A typical trend is of the type represented in Figure 4.4: after a pseudo-linear branch up to the peak stress, a strain-softening phase follows that ends when the zero-stress level, associated with complete debonding, is reached.

As suggested in recent technical standards [1], the $\tau - s$ interface law may approximated by a trilateral (Figure 4.4), formed by a linearly ascending branch up to peak stress τ_f, followed by a linear softening phase approaching $s = s_f$ where $\tau = 0$ and, finally, a zero-stress *plateau*. The fracture energy per unit-surface is $G_f = \frac{1}{2}\tau_f s_f$ and, in general, such value is made to coincide with the integral of the τ vs. s experimental curve. This equivalence allows to evaluate the limit slip

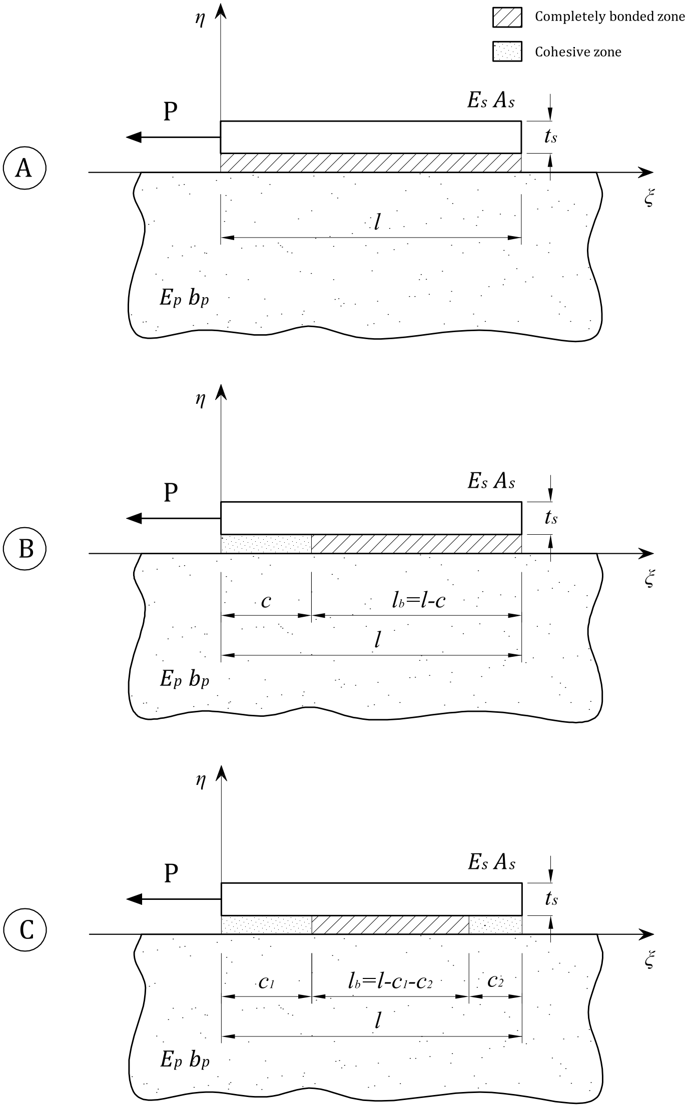
Completely bonded zone
Cohesive zone
A
B
C
P
η
ξ
$E_s\ A_s$
t_s
l
$E_p\ b_p$
c
$l_b=l-c$
c_1
$l_b=l-c_1-c_2$
c_2

Figure 4.3: A finite stiffener bonded to a semi-infinite plate. A) No-cohesive zone (NCZ) model; B) Single cohesive zone (SCZ) model; C) Double cohesive zone (DCZ) model.

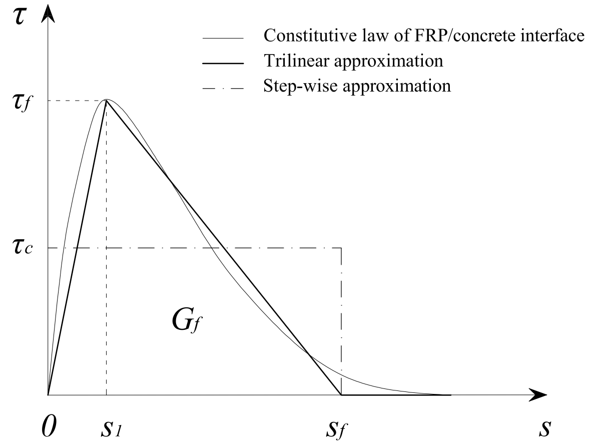

Figure 4.4: Typical experimentally-measured shear-stress vs. slip constitutive law at the interface. Trilinear and step-wise approximation.

s_f once the peak load τ_f is known.

In the simplest NCZ approach of Section 4.2.3, the only relevant parameter is the material fracture energy. Debonding is regulated by Griffith energetic balance, i.e., the stiffener detaches from the substrate whenever the release of elastic energy becomes equal to the work consumed to fracture the interface. Assume that the stress is constant on the width b_s of the interface. Remarkably, as discussed at length in Chapter 3, the energy release rate is associated with the stress intensity factor K_{II} by an expression *à là* Irwin of the type

$$b_s G_f = \frac{K_{II}^2}{2E_p b_p}\,. \tag{4.17}$$

Consequently, the debonding condition for the NCZ model is $K_{II} \geq \sqrt{b_s \tau_f s_f E_p b_p}$.

The models SCZ and DCZ for cohesive debonding of Sections 4.2.2 and 4.2.1 have been derived under the hypothesis that the cohesive force per-unit-length $q_c = \tau_c b_s$ is constant. To comply with this simplification, an equivalence may be established between the triangular and a step-wise constitutive law by imposing the same slip limit s_f and the same delamination fracture energy G_f. This is obviously achieved when $\tau_c = \frac{1}{2}\tau_f$. I will show that, despite this simplification, the obtainable results are in excellent agreement with experimental measurements.

As highlighted in various experimental and numerical works [23, 12], the gross force vs. displacement response of a bonded joint strongly depends upon the bond length l. “Short” stiffeners show a post-peak softening while “long” stiffeners are characterized by a *plateau*, usually followed by a snapback phase (Figure 2.13). These two cases need to be distinguished in the analysis.

Referring to the SCZ model, relative slip takes place in the cohesive zone, whereas adhesion is perfect on the remaining part of the bond length. For any given pull out force P it is possible to calculate the length c of the cohesive zone for which the cohesive force per unit length q_c, supposed uniformly distributed, can annihilate the stress singularity at the extremity of the adherent part. From the elastic solution, it is also possible to calculate the relative slip between stiffener and substrate; debonding starts when the relative slip reaches the limit value s_f (Figure 4.4). The overall response will be different in type in the case of “long” stiffeners and “short” stiffeners.

4.3.2 Load-displacement curve for long stiffeners

Suppose that in the undistorted reference configuration the stringer is bonded over its length l (Figure 4.3 A). Then, the load P is gradually applied at the left hand side. One can consider an hypothetical strain-driven test where the relative displacement of the loaded end of the stiffener with respect to the substrate can be controlled, until debonding starts. From that instant on, equilibrium configurations are sought as the length of the debonded zone increases.

The typical response for long stiffeners is summarized in the graph on the right hand side of Figure 4.5, which shows the applied load P as a function of the relative slip δ_0 between stiffener and substrate, calculated at a reference point coinciding with the loaded end. The curve can be characterized by three branches, which represent respectively the strain-hardening, *plateau* and strain-softening phases. The graph is marked by a series of key-points that correspond to step changes in the response.

The relative slip between stiffener and plate needs to be established at various points. Hereinafter, the slip at ξ may be denoted with $\delta(\xi)$, but to simplify I will use the concise notation

$$\delta(\xi)|_{\xi=\xi_0} \equiv \delta_{\xi_0}. \tag{4.18}$$

As already mentioned, the reference point for the force vs. slip graphs will be the loaded end $\xi = 0$ (Figure 4.1); here the slip, according to (4.18), will be referred to as δ_0.

i) Strain hardening branch (point A).

The first, strain hardening phase, marks the development of the cohesive zone. Using equations (4.13) with condition (4.12), each value of the load P is associated with a unique value of the cohesive length c. Such equations are non linear in c, so that a root-finding algorithm has to be used. Once P and the corresponding c are known, the value of the slip δ_0 at the loaded end $\xi = 0$ can be calculated as

$$\delta_0 = u_s(0) - u_p(0), \tag{4.19}$$

where (Figure 4.1) u_s and u_p are the displacements of the stiffener and of the plate substrate, respectively, taken positive if leftwards, i.e., in opposite direction of the ξ axis. Then, for the situation sketched in Figure 4.5 (A), the relative displacement of a point x comprised in the interval $[0, c]$ can be written as (recall the positive verse of displacements)

$$u_s(x) - u_s(c) = \int_x^c \varepsilon_s(\xi)\, d\xi = \frac{1}{E_s A_s}[P\, c - q_c c^2/2]\,, \tag{4.20}$$

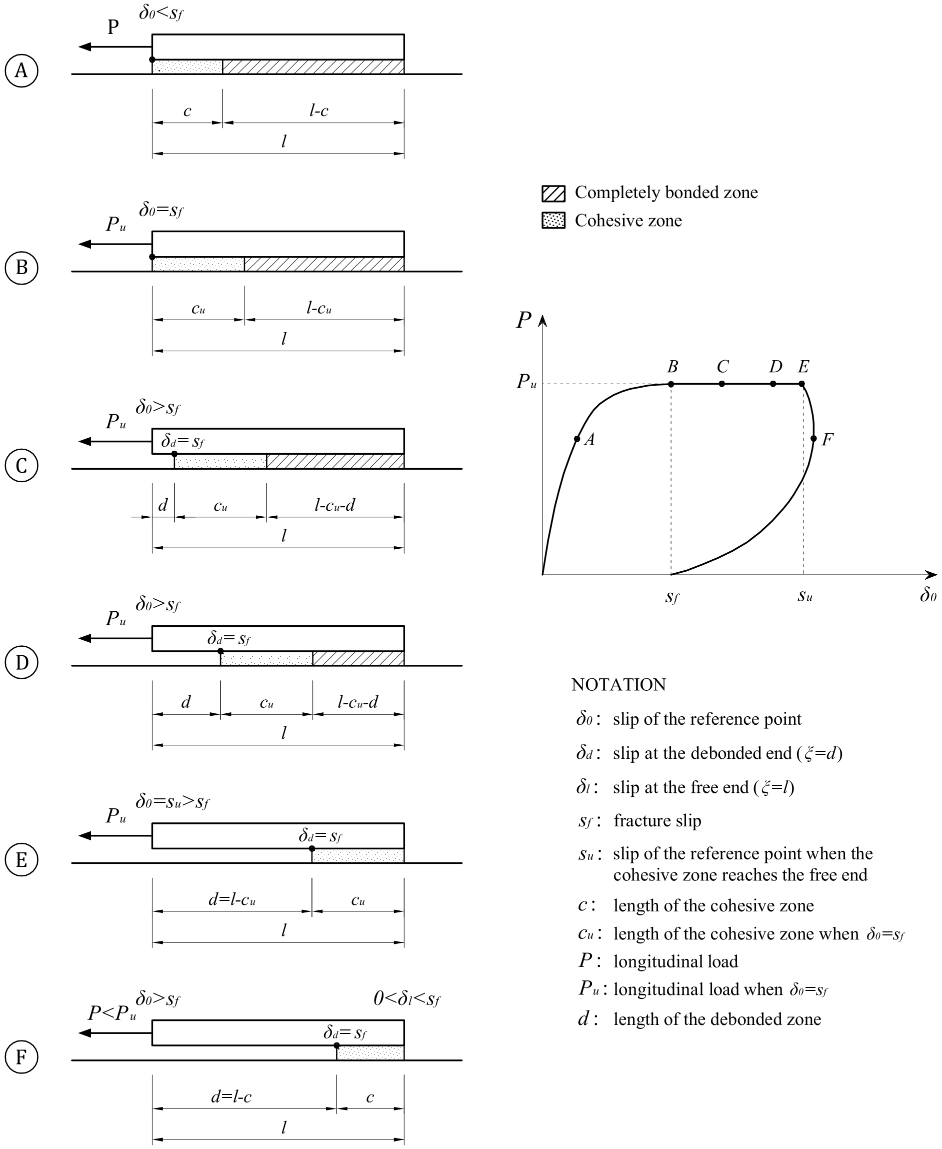
A
P
$\delta_0<s_f$
c
l-c
l
B
P_u
$\delta_0=s_f$
c_u
l-c_u
l
C
P_u
$\delta_0>s_f$
$\delta_d=s_f$
d
c_u
l-c_u-d
l
D
P_u
$\delta_0>s_f$
$\delta_d=s_f$
d
c_u
l-c_u-d
l
E
P_u
$\delta_0=s_u>s_f$
$\delta_d=s_f$
$d=l$-c_u
c_u
l
F
$P<P_u$
$\delta_0>s_f$
$0<\delta_l<s_f$
$\delta_d=s_f$
$d=l$-c
c
l
▨ Completely bonded zone
▒ Cohesive zone
P
P_u
B
C
D
E
A
F
s_f
s_u
δ_0
NOTATION
δ_0: slip of the reference point
δ_d: slip at the debonded end ($\xi=d$)
δ_l: slip at the free end ($\xi=l$)
s_f: fracture slip
s_u: slip of the reference point when the cohesive zone reaches the free end
c: length of the cohesive zone
c_u: length of the cohesive zone when $\delta_0=s_f$
P: longitudinal load
P_u: longitudinal load when $\delta_0=s_f$
d: length of the debonded zone

Figure 4.5: Response of long stiffeners. A) development of the cohesive zone; B) initiation of debonding at the loaded end ($\delta_0 = s_f$); C)-D) propagation of debonded zone; E) the cohesive zone reaches the free end; F) strain softening branch.

$$u_p(x) - u_p(c) = \int_x^c \varepsilon_p(\xi)\, d\xi = u_p(t_0) - u_p(-1) = \int_{t_0}^{-1} \varepsilon_p(t) \frac{l-c}{2}\, dt\,, \quad (4.21)$$

where, in (4.21), I have used the change of variables (4.3). Observing that at $\xi = c$ the plate and stiffener are perfectly bonded so that $u_s(c) = u_p(c)$, the slip δ_0 can thus be calculated from the difference of the terms on the right hand side of (4.20) and (4.21). Referring to the expression (4.2) for the plate strain, equation (4.21), evaluated at $x = 0$ ($t_0 = -(l+c)/(l-c)$), becomes[5]

$$u_p(t_0) - u_p(-1) =$$
$$-\frac{2}{\pi E_p b_p}(P - q_c\, c)\left[X_0 \ln\left(-t_0 + \sqrt{t_0^2 - 1}\right) + \sum_{s=1}^{n} \frac{X_s}{s}\left[(-1)^s - \left(t_0 + \sqrt{t_0^2-1}\right)^s\right]\right]. \quad (4.22)$$

The load P continues to increase as the length c of the cohesive zone increases. The debonding process does not start until the slip δ_0 reaches the limit value s_f (Figure 4.5, point B), i.e., the value of the slip after which the shear stress reduces to zero (Figure 4.4). At this point the maximum load P_u is attained and, correspondingly, the cohesive zone reaches the maximum length c_u.

ii) Plateau (points B-E).

If the test is strain driven, after point B, debonding propagates along the interface (Figure 4.5, points C and D). Let d denote the length of the debonded part. Given d, one can again calculate with the same procedure just outlined the length c of the cohesive zone and the corresponding value of equilibrium load P that annihilates the stress singularity at $\xi = d + c$. The condition in this case is that, at the point $\xi = d$, the slip δ_d equals the fracture slip s_f. Remarkably, one finds that $P \simeq P_u$ and $c \simeq c_u$. In other words, *the cohesive zone, once established, remains constant in practice, and moves towards the free end of the bonded joint, leaving the load P_u unchanged.* As recalled in section 2.3.2.2, the *effective bond length* is usually defined as that bond length beyond which there is no further increase of the strength of the joint. From the former analysis, it is possible now to identify the length c_u as the *effective bond length.* In fact, the debonding process occurs at constant ultimate load in the way just outlined whatever the bond length is, provided this is higher than c_u. In fact, as it will be verified later on, the shear stress in the zone that remains perfectly bonded decays very quickly, so that the entire load P_u is in practice equilibrated by the shear interface-stress acting in the cohesive portion only. Indeed, the part of the load that is equilibrated by the contact forces in the perfectly bonded region is negligible (here, less than 1%) and acts in a very small (right) neighborhood of $\xi = d + c$.
From this analysis, it is then possible to make precise the definition of "long" stiffeners. A stiffener is "long" when its bond length is higher than c_u. If this is

---

[5] Note that the point t_0 is external to the interval of contact, i.e. $t_0 < -1$, so integration has to be performed using relation (A.6) for the case $|t_0| > 1$.

the case, the stiffener can withstand the maximum tensile load, associated with the formation of the maximum cohesive zone c_u, that is, the development of the full stress-transfer zone.

As debonding develops, the relative slip δ_0 at the reference point $\xi = 0$ increases as a consequence of the strain of the debonded portion of the stringer, not any more constrained by the substrate. To precisely determine δ_0, it is necessary to calculate the displacement of the plate at $\xi = 0$ ($t_0 = -(l + c_u + d)/(l - c_u - d)$) that, similarly to (4.22), can be found from an expression of the form

$$u_p(t_0) - u_p(-1) = -\frac{2}{\pi E_p b_p}\Bigg\{ q_c\Big(-c_u \ln c_u + (c_u + d)\ln(c_u + d) - d \ln d\Big) \\ + (P - q_c\, c_u)\left[X_0 \ln\left(-t_0 + \sqrt{t_0^2 - 1}\right) + \sum_{s=1}^{n} \frac{X_s}{s}\left[(-1)^s - \left(t_0 + \sqrt{t_0^2 - 1}\right)^s\right]\right]\Bigg\}. \tag{4.23}$$

Observing again that $u_s(-1) = u_p(-1)$, the slip δ_0 at the reference point becomes

$$\delta_0 = [u_s(t_0) - u_s(-1)] - [u_p(t_0) - u_p(-1)] = \frac{1}{E_s A_s}[P_u(d + c_u) - q_c c_u^2/2] - [u_p(t_0) - u_p(-1)]\,. \tag{4.24}$$

Clearly δ_0 increases with the debonding length d and this is why this phase is associated with a *plateau*.

iii) Strain softening branch (point F).

When the cohesive zone reaches the free end, the strain softening branch is attained (Figure 4.5, point E). From now on, the interface is purely cohesive and the shear forces are equal to q_c. If the stringer is pulled further, the relative slip increases and debonding proceeds where the relative slip exceeds the limit value s_f of Figure 4.4. However, this phenomenon is associated with a sudden decrease of the load carrying capacity and the consequent release of the stiffener produces in general a snap-back response (Figure 4.5, point F).

Observe that the snap-back phase cannot be revealed if the test is strain driven: therefore at this point a new control variable must be introduced. In particular, as done in the experimental tests of [12], the control variable can be chosen to be the slip δ_l of the free end $\xi = l$ of the stiffener. The relative slip δ_0 at the reference point $\xi = 0$ is then equal to

$$\delta_0 = [u_s(0) - u_s(l)] - [u_p(0) - u_p(l)] + \delta_l\,, \tag{4.25}$$

where

$$u_s(0) - u_s(l) = \frac{q_c\, c}{E_s A_s}(l - c/2)\,, \tag{4.26}$$

and

$$u_p(0) - u_p(l) = -\frac{2}{\pi E_p b_p}\left[q_c\Big(-c\ln c + l\ln l - (l-c)\ln(l-c)\Big)\right]. \qquad (4.27)$$

For any given value of δ_l the corresponding c is found from condition that at $\xi = d \equiv l - c$ the relative slip δ_d equals the limit value s_f of Figure 4.4. The resulting $P - \delta_0$ graph actually exhibits a snap-back response. If one neglects the strain in the plate and the consequent displacement given by (4.27), the snap back branch shows a parabolic trend. As $P \to 0$, the slip δ_0 of the reference point $\xi = 0$ tends to the value s_f.

4.3.3 Load-displacement curve for short stiffeners

Having defined in section 4.3.2 the length c_u as the effective bond length, one can consequently call "short" stiffeners those for which $l < c_u$. The debonding process for this case is sketched in Figure 4.6.

i) Strain hardening branch (point A).

The first stage is characterized by a strain-hardening branch where the cohesive zone develops. The equilibrium configuration at point A can be calculated with the same procedure of Section 4.3.2. However, now the stringer is too short to permit the development of the entire effective bond length c_u. Consequently, point B of Figure 4.6 is characterized by a full cohesive interface of length $l < c_u$ where $q = q_c$, and a relative slip δ_0 of the reference point $\xi = 0$ such that $\delta_0 < s_f$. The ultimate load is consequently attained at $P_u = q_c l$.

ii) Plateau (points B-D).

Augmenting the pull out displacement, the relative slip increases due to a rigid translation of the stringer, characterized by the relative slip δ_l of the free end $\xi = l$. The scenario is that of point C, with the load remaining equal to P_u.
It must be clearly remarked that the *plateau* attained in this case of short stiffeners is different in type from that developing in long stiffeners, discussed in the preceding section 4.3.2. In short stiffeners the *plateau* is due to a uniform slip of the completely yielded interface and, consequently, its width can never exceed the limit value s_f defined in the constitutive relation of Figure 4.4. On the other hand, in long stiffeners the *plateau* is consequent to a progressive translation of the cohesive zone, and its extension becomes proportional to the bond length.
Since s_f is in general very small, in short stiffeners the *plateau* can be hardly recognized, although for clarity of representation it has been oversized in the graph on the right hand side of Figure 4.6. On the contrary, long stiffeners exhibit a well-marked yielding, due to the progressive debonding and consequent translation of the cohesive zone c_u throughout the stiffener length. This finding is in agreement with the experimental results, qualitatively recalled in Figure 2.13.
Eventually, one reaches point D, characterized by condition $\delta_0 = s_f$.

iii) Strain softening branch (point E).

After passing point D, it is again necessary to switch the control variable to the relative slip δ_l of the free end $\xi = l$. Increasing this parameter, the situation is

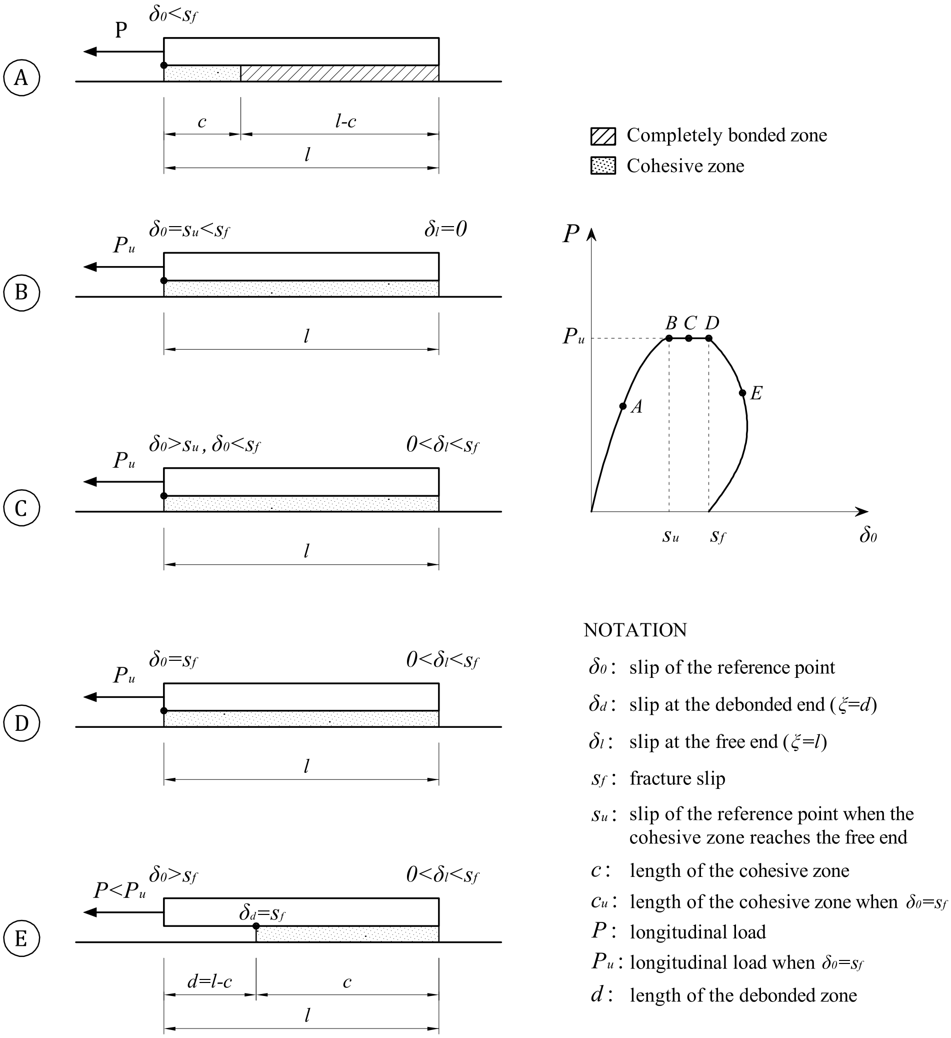
A
P
$\delta_0 < s_f$
c
l-c
l
B
P_u
$\delta_0 = s_u < s_f$
$\delta_l = 0$
l
C
P_u
$\delta_0 > s_u$, $\delta_0 < s_f$
$0 < \delta_l < s_f$
l
D
P_u
$\delta_0 = s_f$
$0 < \delta_l < s_f$
l
E
$P < P_u$
$\delta_0 > s_f$
$0 < \delta_l < s_f$
$\delta_d = s_f$
d=l-c
c
l
▨ Completely bonded zone
░ Cohesive zone
P
P_u
B C D
A
E
s_u
s_f
δ_0

NOTATION

δ_0 : slip of the reference point

δ_d : slip at the debonded end ($\xi = d$)

δ_l : slip at the free end ($\xi = l$)

s_f : fracture slip

s_u : slip of the reference point when the cohesive zone reaches the free end

c : length of the cohesive zone

c_u : length of the cohesive zone when $\delta_0 = s_f$

P : longitudinal load

P_u : longitudinal load when $\delta_0 = s_f$

d : length of the debonded zone

Figure 4.6: Response for short stiffeners. A) development of the cohesive zone; B) the cohesive zone reaches the free end; C) *plateau* due to rigid slip; D) initiation of debonding ($\delta_0 = s_f$); E) strain softening branch.

like that of Figure 4.6, point E. For a given δ_l, one can find the length c of the cohesive zone from the condition that relative slip δ_d at $\xi = d \equiv l - c$ is equal to s_f.

At this stage, the $P - \delta_0$ graph can be found from conditions analogous to (4.25), (4.26) and (4.27). The result is as represented on the right-hand-side of Figure 4.6.

4.4 Theoretical prediction of the contact shear stress

The interfacial shear stress associated with the NCZ, SCZ and DCZ models are now compared in an example that uses the material data from the experiments of [12]. Results for a bond length of $l = 150$ mm are represented in Figure 4.7, which shows the normalized interfacial shear force distribution q/q_c at various stages of loading. Results are shown for increasing complexity of the models, i.e., from the NCZ model to the DCZ model.

i) The NCZ model

It is evident in Figure 4.7(a) the presence of singularities at both ends of the reinforcement. The stress rapidly diminishes going towards the free end of the stiffener: it is almost null for most part of the bond length, except for a very small zone near the free end where another singularity occurs. The results that can be obtained with this model have been discussed at length in Chapter 3.

ii) The SCZ model

For each value of the applied load, the length c of the cohesive zone can be calculated with the equations of Section 4.2.2. In the normalized interfacial-force graph of Figure 4.7(b) it is evident that at the loaded end the shear distribution tends to the maximum allowable stress q_c, i.e.,

$$\lim_{\xi \to c} \frac{q(\xi)}{q_c} = 1\,. \tag{4.28}$$

This means that the shear stress at the frontier between the cohesive and the perfectly bonded zones is continuous. At the free edge of the stiffener, the solution still presents the singularity predicted by the theory of elasticity. Debonding starts when the relative slip between stiffener and substrate exceeds the limit value s_f. In this particular example, the applied load is always lower than the debonding limit.

What is important to notice for this case is that most of the applied load is equilibrated by the tangential force acting in this cohesive portion; in particular, the stress singularity at the free end does not play a significant role in the equilibrium of the stiffener. To illustrate, Figure 4.8 shows the load fraction carried by the cohesive part (P_{cohes}/P) and by the remaining part of the bond length (P_{bond}/P) as a function of the applied load P. In the same picture the value of the cohesive zone length c corresponding to each load-level is indicated at the top border. It is clear that increasing the load, the cohesive portion is the one that gives by far the most important contribution ($P_{cohes}/P \simeq 1$).

Figure 4.9 represents the axial load P as a function of the slip δ_0 at the reference point $\xi = 0$ (Figure 4.5), calculated with no consideration of debonding, i.e., as if

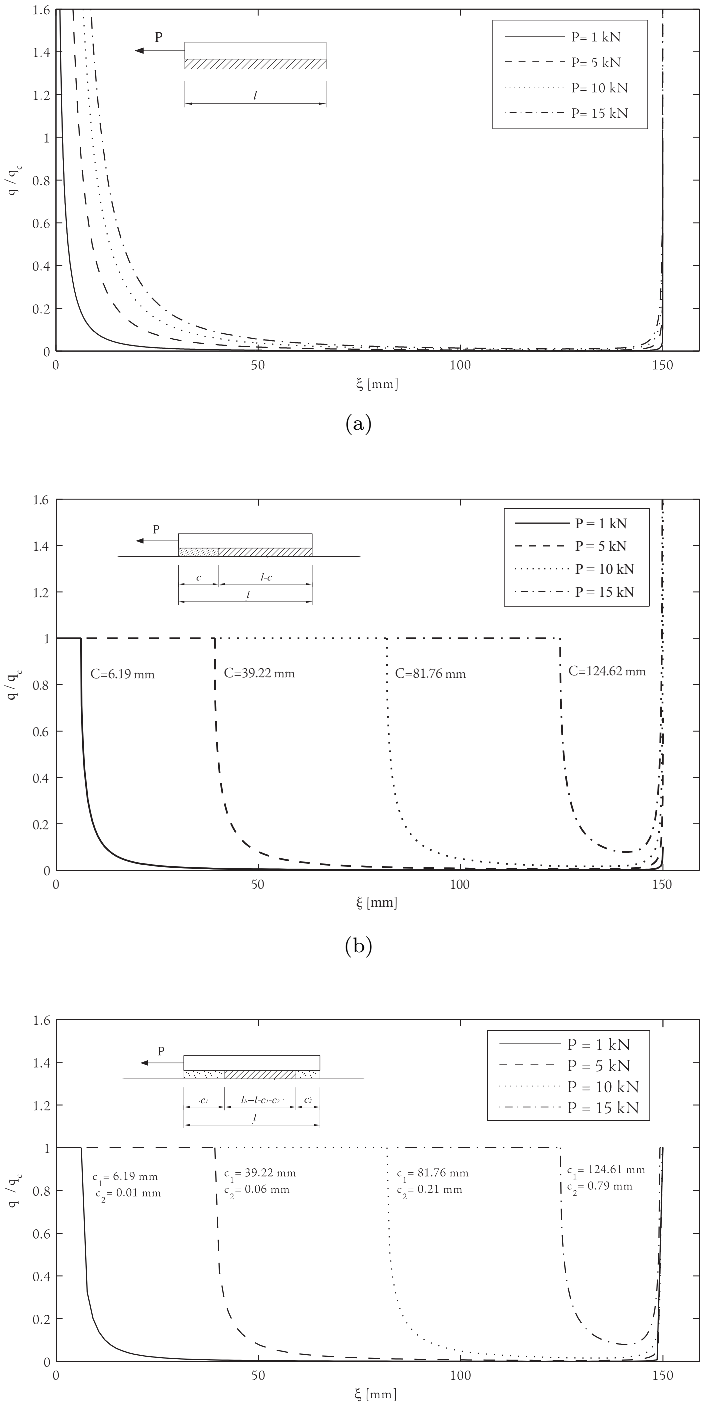

(a)

(b)

(c)

Figure 4.7: Interfacial shear force distribution for different values of the applied load. Same materials of [12], with initial bond length $l = 150$ mm. (a) No-cohesive zone (NCZ) model; (b) Single cohesive zone (SCZ) model; (c) Double cohesive zone (DCZ) model.

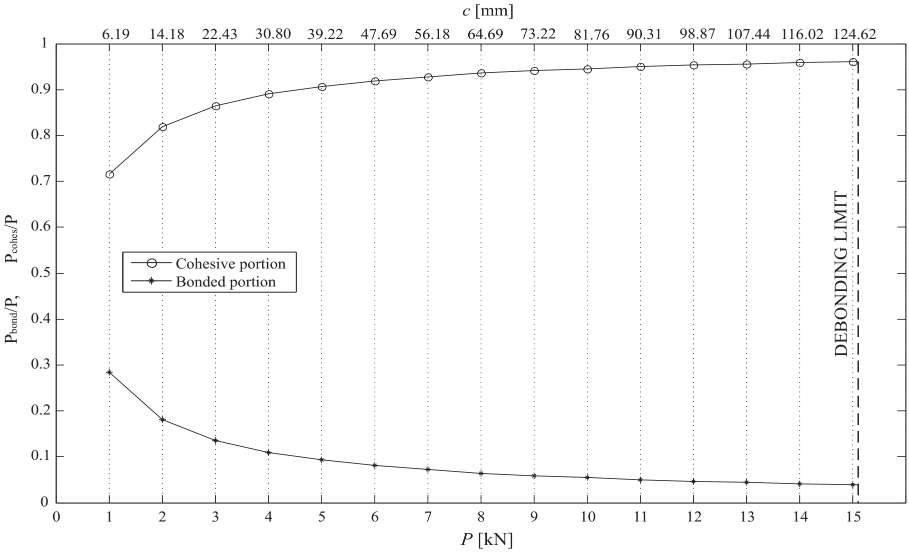

Figure 4.8: Load fraction balanced by the interface stresses acting on the cohesive portion and on the perfectly bonded portion as a function of the applied load. Results from the SCZ model (bond length $l = 150$ mm and mechanical parameters of [12]).

the interface had infinite ductility. Table 4.1 indicates that for the tests of [12] the failure slip is $s_f = 0.15$ mm. Therefore at $\delta_0 = 0.15$ mm debonding starts, and the corresponding load $P_u = 15.09$ kN is the ultimate load. An effective bond length $c_u = 125.4$ mm corresponds to this case. As the load is increased, the cohesive zone reaches a maximal length c_u after which debonding starts and, as shown in section 4.3, the cohesive zone translates towards the free end of the stiffener maintaining its length practically unaltered. This is confirmed by Figure 4.10, which represents the axial load P as a function of the global slip δ_d, calculated at the end of the debonded zone $\xi = d$, for three different values ($d = 0$, $d = 5$ mm, $d = 10$ mm) such that $d + c_u < l$. These cases correspond to the configurations C and D of Figure 4.5. For each value of d, a new cohesive length is derived from condition (4.12) as a function of P. The three graphs in practice overlap, meaning that the response is substantially similar in all the cases when the bond length is greater than c_u. In particular, the value of the cohesive length when $\delta_d = s_f$ is independent of d (c_u varies in the range $125.20 \div 125.41$), while the critical load P_u is practically constant ($P_u \simeq 15$ kN).

In general, the length of the cohesive zone c depends upon the value of the applied load P, independently of the bond length of the stiffener. This is also confirmed by Figure 4.11, which represents the value of c associated with various values of the load P for increasing values of the bond length l. Remarkably, c does not substantially change as l is varied. However, a minimum value of the bond length l has to be associated with each load P. This derives from the condition that $l > P/q_c$, so that for a given value of load there is a minimum length necessary to develop the cohesive zone.

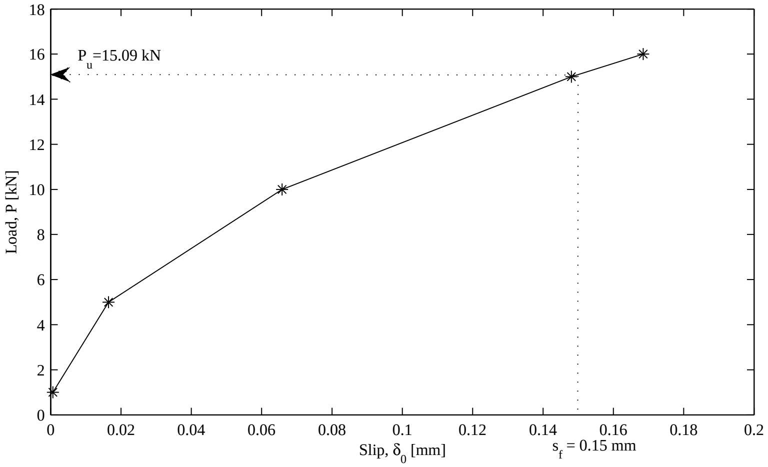

Figure 4.9: Load-slip ($P - \delta_0$) curve for the same material parameters of [12] (Bond length $l = 150$ mm).

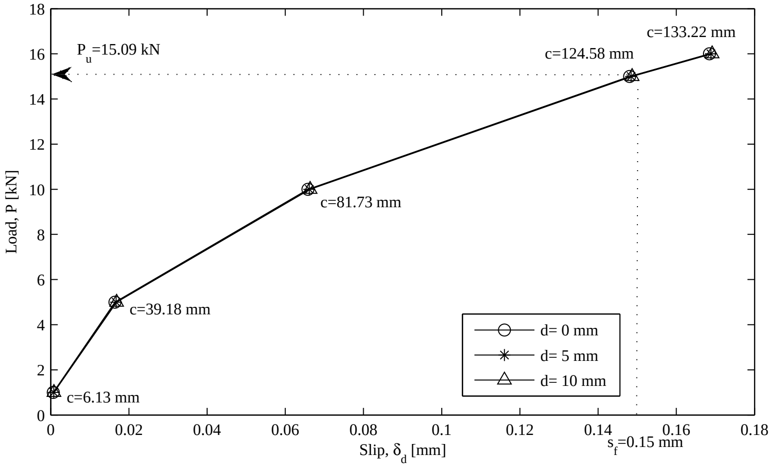

Figure 4.10: Load-slip curves ($P - \delta_d$) for different values of the debonded length d (Experimental data of [12]).

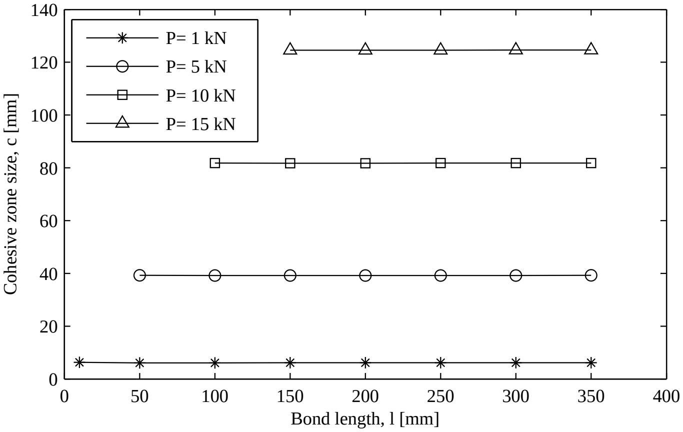

Figure 4.11: Length c of the cohesive zone as a function of different bond lengths l and axial loads P.

iii) The DCZ model

Once the value of the cohesive lengths associated with a given load and the respective constants X_s are evaluated, the interface force per unit length q can be calculated with the expression (4.8). Results are represented in Figure 4.7(c) where, in particular, the values of the cohesive lengths c_1 and c_2, as defined in Figure 4.3 C, have been indicated near the curve corresponding to each load. Also for this case, at the frontier between the bonded part and the cohesive portions the stress results to be continuous, i.e.,

$$\lim_{\xi \to c_1} \frac{q(\xi)}{q_c} = 1 \ , \quad \lim_{\xi \to l-c_2} \frac{q(\xi)}{q_c} = 1 \, . \tag{4.29}$$

In any case, the length of the cohesive zone at the free end of the stiffener is much smaller than that at the loaded end. Comparing the values of c_1 with the corresponding values of c for the SCZ model, also highlighted in Figure 4.7(b), it is clear that at the loaded cohesive zone the SCZ and the DCZ models give in practice identical results. The shear stress profile at the interface does not appreciably change if the singularity at the free end is removed, apart of course in a neighborhood of the free end. In any case, that part of the applied load that is equilibrated by the second singularity at the free end is not significant.

To make this clearer, Figure 4.12 represents the fraction of the axial load equilibrated by that portion of bond length laying on the left-hand side of the generic abscissa ξ. The results obtained with the three approaches for $P = 15$ kN are juxtaposed: the NCZ model (continuous line), the SCZ model (dashed line) and the DCZ model (dash-dotted line). For what the NCZ model is concerned, notice that a bonded length of ~ 20 mm is sufficient to balance 97% of the axial load: in rough terms, most of the load is balanced by the singularity at the loaded edge. Instead, the SCZ and the DCZ curves evidence that a bond length higher than

$\sim$ 120 mm is necessary to balance the relevant part of the applied load. The curves obtained with both the SCZ and DCZ models almost overlap, confirming that the part of load carried out by the singularity at the free end is negligible. Figure 4.12(b) shows a magnification of Figure 4.12(a) in a neighborhood of the free end of the bond length. It is again evident that the main discrepancy between the dashed curve (SCZ model) and the dash-dotted curve (DCZ model) is in a very small part of the bond length, and that the difference between the results obtainable with the two approaches is not substantial.

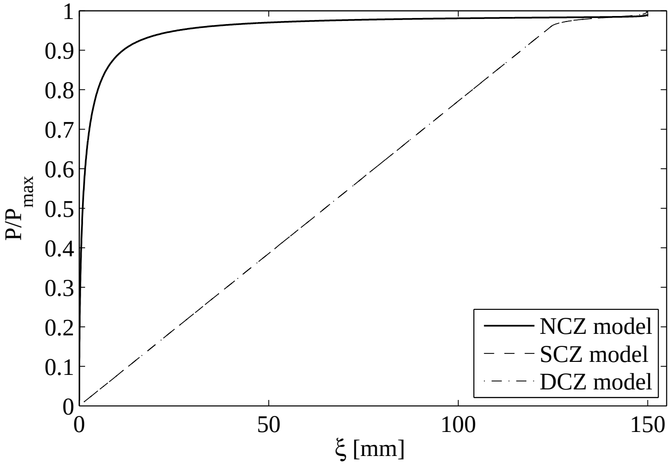

(a)

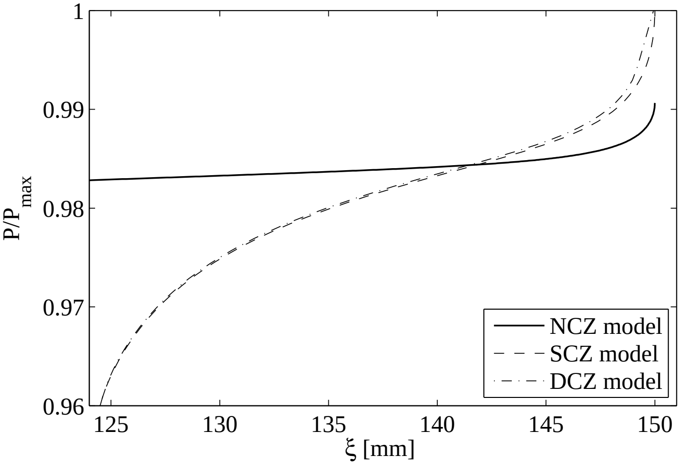

(b)

Figure 4.12: Fraction of the axial load balanced by the interfacial shear force acting in the portion $0 \leq x \leq \xi$. Mechanical parameters of [12] ($l = 150$ mm and $P_{max} = 15$ kN). (a) Comparison between the NCZ, the SCZ and the DCZ model; (b) Detail of the portion comprised between $\xi = 125$ mm and $\xi = 150$ mm.

In conclusion, the NCZ model predicts a rapid decay of the interface shear stress because most of the applied load is carried in a small neighborhood of the stress singularity at the loaded end of the stiffener. In the cohesive interface models, most of the load is carried in the yielded portion of the bond length in proximity of the loaded end. The SCZ model still predicts a singularity at the free end of the stiffeners, but this does not furnish a significant contribution. Indeed, the length of the cohesive portion in proximity of the loaded end of the stiffeners, which is the most important, remains substantially the same in both the SCZ and the DCZ models. Consequently, if one is mainly interested in the engineering evaluation of the mechanism of adhesion, reference could be made to the SCZ model, which requires a computational effort much lower than the DCZ model.

4.5 Effective bond length. Comparison with experiments

There is a general agreement that the adhesion strength (in pure mode II) of a stiffener on a substrate is characterized by an intrinsic length usually referred to as the *Effective Bond Length (EBL)*. This can be defined as the length necessary to transfer the load from the stiffener to the substrate (see section 2.3.2.2). In fact, it has been experimentally verified that increasing the bond length beyond such limit does not lead to any increase of load carrying capacity, confirming that only part of the bond is active. For this reason, the determination of this limit is of fundamental importance in the characterization of the joint performance (as seen in section 4.3).

The aim of this section is to assess the capability of the three considered models to capture, besides the ultimate load, the value of the EBL. Such value can be experimentally determined from pull-out tests on stiffeners with different bond lengths: by definition, the EBL is the bond length beyond which the ultimate load remains almost constant. Comparisons will be made between the analytical outputs and the results from relevant experimental campaigns recorded in the technical literature.

4.5.1 Assessment of the constitutive properties of the interface from experiments.

Several experimental results for FRP reinforced concrete will be now considered. With reference to [23, 12, 8, 11, 9, 25], Table 4.1 reports the specimen properties and the parameters τ_f and s_f that are associated with the trilinear constitutive interface law $\tau - s$ of Figure 4.4. Recall that, following the equivalence established in Section 4.3.1, in the cohesive models here considered a step-wise approximation of the interface-law will be used, with $\tau_c = \tau_f/2$. Since most of the times the values of τ_f and s_f are not explicitly provided in the technical references, it is necessary to describe how they can be derived from generic experimental results.

When only the characteristic compressive strength of concrete f_{ck} is known [65], one can evaluate τ_f through an expression borrowed from technical standards [1] of the form

$$\tau_f = 0.64\kappa_b\sqrt{f_{ck}f_{ctm}}\,, \qquad (4.30)$$

where $f_{ctm} = 0.30\sqrt[3]{(f_{ck})^2}$, with f_{ck} expressed in MPa, is the value of the average tensile strength of concrete [65], while $\kappa_b = \sqrt{\frac{2-b_s/b_p}{1+b_s/400[\text{mm}]}} \geq 1$. The values in Table 4.1 that have been obtained with this procedure have been evidenced by an asterisk.

If the fracture energy per unit area G_f is known, then one readily has $s_f = 2G_f/\tau_f$. When G_f is not explicitly given, it can be approximated through the simple expression

$$G_f = \frac{(P_{max,e})^2}{2b_s^2 E_s t_s}\,, \tag{4.31}$$

where $P_{max,e}$ is the experimentally measured peak load[6] and t_s is the thickness of the stiffener. Such an expression, also suggested by standards [1], neglects the elasticity of the substrate [60] and results quite accurate for FRP-reinforced concrete. However, for the proper evaluation of the shear interface forces, the elasticity of the substrate cannot in general be neglected.

Table 4.1: Mechanical properties of materials used in experimental campaigns and parameters of the interface law.

	Concrete^a			**FRP**			**Interface Law**^{b}	
Test^c	E_p [MPa]	t_p [mm]	b_p [mm]	E_s [MPa]	t_s [mm]	b_s [mm]	τ_f [MPa]	s_f [mm]
Ali Ahmad *et al.* [23]	33230	125	125	230000	0.167	46	7.07	0.230
Carrara *et al.* [12] *	28700	90	150	168500	1.3	50	7.71	0.150
Chajes *et al.* [8] *	34411	152.4	152.4	108478	1.016	25.4	8.78	0.234
Mazzotti *et al.* [11]	30700	200	150	195200	1.2	50	9.14	0.0971
Taljsten [9] *	35000	200	200	170000	1.25	50	9.04	0.154
Yuan *et al.* [25]	28600	150	150	256000	0.165	25	7.20	0.160

Notes:
a. When the literature provides the cylindrical strength f_{ck} only, then, as suggested in technical standards [65], E_p is calculated through $E_p = 22000(f_{cm}/10)^{0.3}$ MPa, being $f_{cm} = f_{ck} + 8$ MPa, f_{ck} in MPa.
b. When the literature does not provide the value for the peak stress τ_f, then expression (4.30) from the Italian Standard [1] has been used.
c. Experimental tests for which the interface-law parameters are not explicitly provided are evidenced by an asterisk (*).

Let us then discuss the results that can be obtained with the various formulations just presented. For what G_f is concerned, the values calculated in the experiments by evaluating the work consumed during the fracture process (integration of the load vs. displacement curve) may differ from the values obtained through (4.31), but the discrepancy is in general very small. This parameter is the only one that needs to be considered in the NCZ approach: the ultimate load can be calculated through the evaluation of the stress intensity factor as *per* (4.17). If one calculates from the experimentally-determined value of the ultimate load the debonding surface energy through (4.31), which derives from a Griffith-like energetic balance where the elasticity of the substrate is neglected, and afterwards re-calculate the ultimate load through (4.17), which considers the elasticity of the substrate, the results that are obtained are in practice the same. This confirms that, at least for concrete, the elasticity of the substrate does not give a substantial contribution for what the evaluation of G_f is concerned. In general I have found that evaluating G_f through (4.31) provides a slightly better approximation than the integration of the experimental load vs. displacement curve (when this is provided in the technical reference), which is usually subjected to measurement errors.

---

[6] The maximum axial loads derived from experiments are recorded later on in Table 4.2.

The parameters τ_f and s_f are of importance for the SCZ and the DCZ models. In order to understand how they may affect the results, reference is made to the tests of [23] and [8], where the sophisticated experimental apparatus allowed a precise measurement of the constitutive interface law.

Figures 4.13(a) and 4.13(b) refer to the tests of [23] and shows P_u as a function of the virgin bond length l. The points indicated with dots refer to data obtained by the same authors in [66] with very accurate numerical experiments that took into account the exact, experimentally measured, interface-law. The graph drawn with continuous line in Figure 4.13(a) refers to the results obtainable with the SCZ model by considering $\tau_f = 5.03$ MPa, $s_f = 0.23$ mm, i.e., the average peak stress and the fracture slip limit of the interface-law that was experimentally-measured in [23].

Since this graph does not exactly match with experiments, I attempted at varying the fracture slip s_f while keeping unchanged the maximum shear stress τ_f. By considering the average experimentally-measured value $G_f = 0.735$ MPa mm [23], one obtains $s_f = 2G_f/\tau_f = 0.292$ mm. The corresponding graph, which is indicated by the dashed curve in Figure 4.13(a), still underestimates the ultimate load. But it is also possible to evaluate the fracture energy from (4.31): taking $P_{max,e} = 11.5$ kN as the average experimental value of [23], one obtains $G_f = 0.812$ MPa mm and, leaving unchanged $\tau_f = 5.03$ MPa, the value $s_f = 0.3235$ mm. The curve obtained in this way is the one indicated by a dotted line in Figure 4.13(a). This shows excellent results for what the evaluation of the maximum load is concerned, but results are still inaccurate for short bond lengths ($l < 100$ mm).

Because of this discrepancy, a further elaboration has been made by assuming that now $s_f = 0.23$ mm is fixed and by changing τ_f. The graphs in Figure 4.13(b) show, respectively, again the curve obtained with the experimentally-measured values $\tau_f = 5.03$ MPa and $s_f = 0.23$ mm (continuous line); the curve corresponding to $G_f = 0.735$ MPa mm and $\tau_f = 2G_f/s_f = 6.39$ MPa (dashed line); the curve associated with $G_f = 0.812$ MPa mm from equation (4.31) and the corresponding $\tau_f = 7.07$ MPa (dotted line). It is clear that it is the dotted line that approximates the best the experiments.

A similar procedure has been followed for the experimental data of Chajes *et al.*

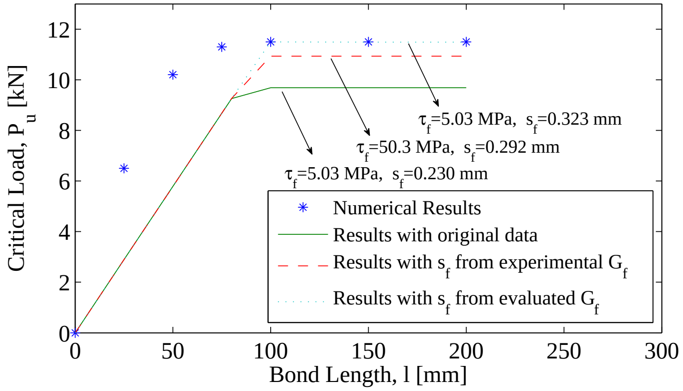

(a) Tests of Ali-Ahmad *et al.* [23]. Varying fracture slip s_f.

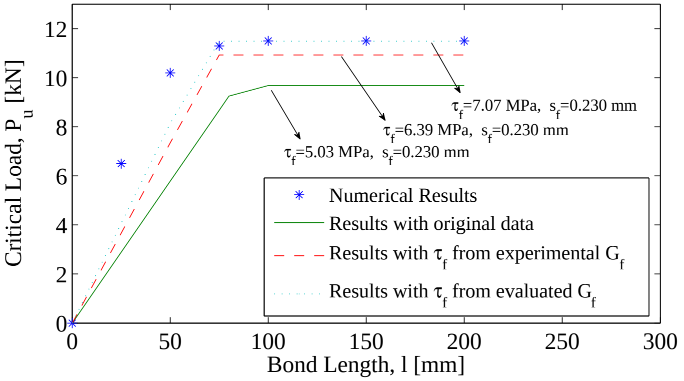

(b) Tests of Ali-Ahmad *et al.* [23]. Varying peak stress τ_f.

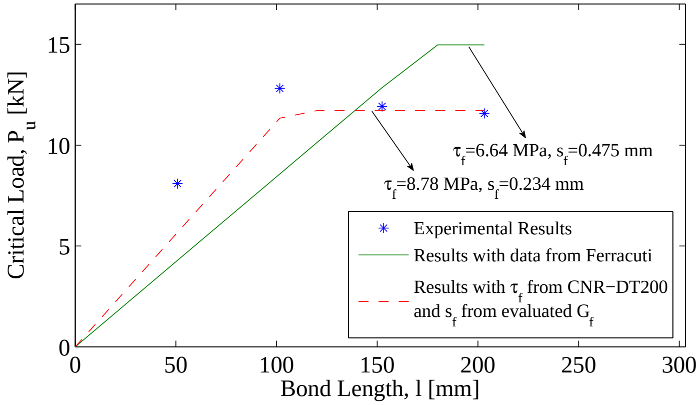

(c) Tests of Chajes *et al.* [8]

Figure 4.13: Maximum applied load as a function of the bond length. Influence of the parameters that define the interface law.

[8], where the authors did not directly provide the parameters of the interface law. At first, an attempt has been made to use the method by Ferracuti *et al.* [26], who proposed a procedure to derive a non-linear mode II interface law starting from experimental data. With a calibration procedure, they obtained $\tau_f = 6.64$ MPa and $s_f = 0.475$ mm for the experiments of [8]. The corresponding curve, which is shown with continuous line in Figure 4.13(c), is not accurate. In a second attempt, the expression (4.31) for G_f has been calculated using the maximum experimental load of [8]: setting $\tau_f = 8.78$ MPa as *per* (4.30), one finds $s_f = 0.234$ mm. The results, drawn with dashed line in the same picture, show a very good agreement with the experimental data.

In conclusion, the best approximations are usually achieved when G_f is estimated through (4.31) from the maximum load obtained in pull-out experiments. This quantity defines the product $\tau_f \cdot s_f$. The best way to find the relative values of these parameters is through a calibration of the model on the basis of simple experimental campaigns, where the pull-out load is measured for various values of the bond length (short and long stiffeners). This approach by-passes all the technical difficulties of a sophisticated experimental apparatus that always becomes necessary to evaluate the constitutive interface-law and, what is more, all the uncertainties of such a complicated measure. The values of τ_f and s_f that are indicated in Table 4.1 have obtained following this procedure.

4.5.2 Results from the various models.

The results obtainable with the NCZ, SCZ and DCZ models are now compared with the experiments of [23, 12, 8, 11, 9, 25], using the material parameters of Table 4.1.

i) The NCZ model

As in Section 4.3.1, let G_f represent the fracture energy per unit surface and $G_f b_s$ the fracture energy per unit length of the stiffener. Then, from the expression (4.17) for the strain energy release rate associated with an infinitesimal crack growth, one finds

$$G_f b_s = \frac{K_{II}^2}{2E_p b_p} = \frac{P^2}{\pi E_p b_p l}\left[\sum_{s=0}^{n} X_s(-1)^s\right]^2, \tag{4.32}$$

so that the critical value P_u of P reads

$$P_u = \sqrt{G_f b_s \frac{\pi E_p b_p l}{\left[\sum_{s=0}^{n} X_s(-1)^s\right]^2}}\,. \tag{4.33}$$

Values of the critical load as a function of the bond length l obtained for the mechanical parameters of [23, 12, 8, 11, 9, 25] are indicated by a continuous line in Figures 4.14 and 4.15 as a function of the bond length. Each graph is compared with the experimental data, here indicated by dots[7], and with the results from the SCZ model (dashed line) and the DCZ model (dotted line), whose derivation is done in the sequel.

---

[7] In the case of [23] and [25], the dots refer to very careful numerical experiments that consider

For what the NCZ model is concerned, notice that the values of the bond length beyond which there is no substantial increase of the ultimate load, i.e., the EBL, is of the order of few millimeters. This is due to the rapid decrease of the interfacial shear stress beyond the singularity, but the result is not corroborated by experiments. In other words, the NCZ model underestimates the EBL.

The values of the ultimate load calculated with the mechanical parameters of the experimental campaigns of [23, 12, 8, 11, 9, 25] are summarized in Table 4.2, together with the results of the SCZ model, the DCZ model and experimental data recorded in the Literature. More precisely, in the "experimental data" columns, the mean experimental value on the peak load has been indicated with $P_{max,e}$, while the values of the EBL evaluated from the experimental data[8] have been referred to as $l_{e,e}$.

ii) The SCZ model

The results of the SCZ model are shown in Figures 4.14 and 4.15 by dashed lines. Comparison with the experimental data [23, 12, 8, 11, 9, 25] evidences the good agreement with the prediction of the model for what the ultimate load is concerned. Notice that P_u increases with the bond length l until the limit of the EBL, which is also well captured by the model. The values of the ultimate load and of the EBL so calculated are also summarized in Table 4.2.

As largely discussed in section 4.3, since the greatest part by far of the applied load is equilibrated by the cohesive shear forces acting in the yielded portion of the adhesive, in this model the EBL may be associated with the *maximal* length c_u of the cohesive zone attained in *long* stiffeners. Increasing the bond length beyond this limit does not increase the load bearing capacity of the joint. The value of c_u, calculated through the model, is also evidenced in Figure 4.14 and Figure 4.15 with a circular marker and denoted with $c_{u,\mathrm{SCZ}}$. It matches very well with the limit bond length according to the standard definition.

The EBL could thus be evaluated through a strain-driven pull-out test on *long* stiffeners. Measuring the relative displacement of the loaded end, debonding starts when the relative slip of the reference point reaches the fracture slip s_f predicted by the interfacial constitutive law (see Figure 4.4). At this point, the maximum load that can be carried by the FRP stringer is attained. The maximal cohesive zone c_u at the beginning of the debonding gives a physical characterization of the EBL.

Recall that, as demonstrated in section 4.3, the value of the ultimate cohesive length c_u does not change as debonding proceeds, but simply the cohesive zone moves towards the free end of the stiffener, leaving its length unaltered, so that the ultimate load P_u remains almost constant. This confirms that increasing the bond length over the EBL limit does not increase the anchorage strength of the joint. However, it certainly improves the joint ductility!

---

the full constitutive interface-law obtained through sophisticated experimental apparatus.

[8] The effective bond length is here defined as that limit of the bond length beyond which no apparent increase of ultimate load is experimentally observed.

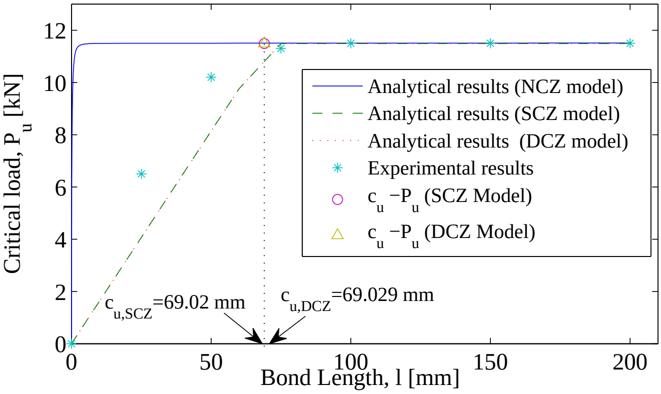

(a) Tests of Ali-Ahmad *et al.* [23]

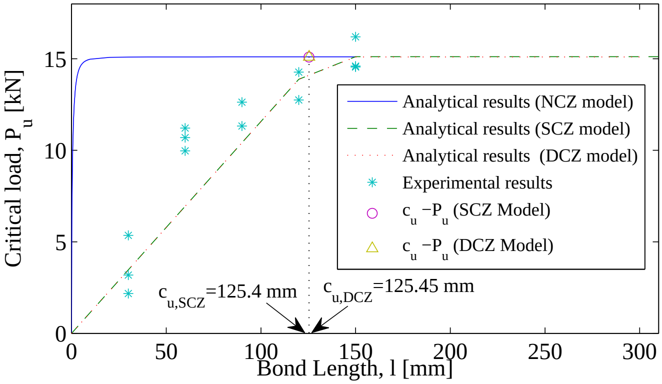

(b) Tests of Carrara *et al.* [12]

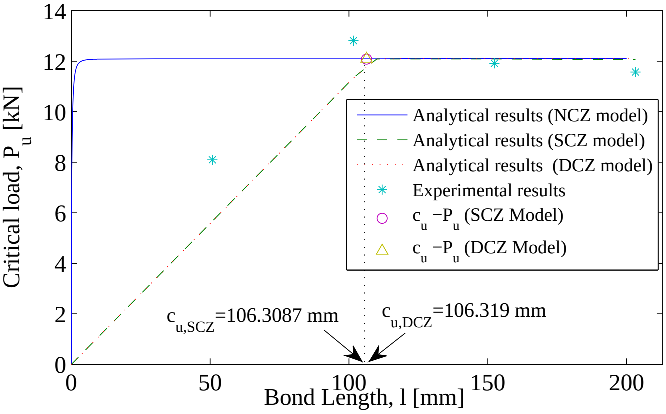

(c) Tests of Chajes *et al.* [8]

Figure 4.14: Ultimate load P_u as a function of the initial bond length l. Predictions of the NCZ, SCZ and DCZ models and comparisons with experimental results.

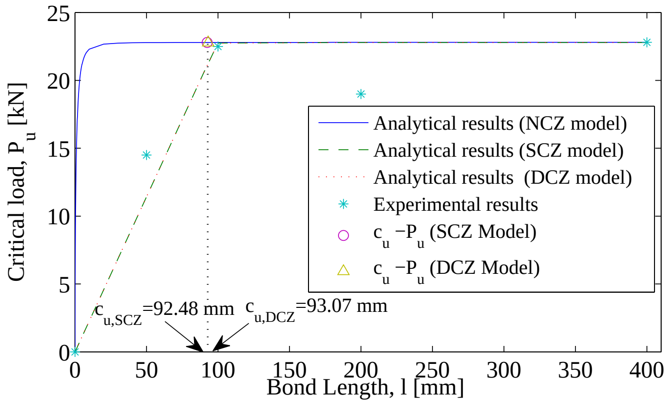

(a) Tests of Mazzotti *et al.* [11]

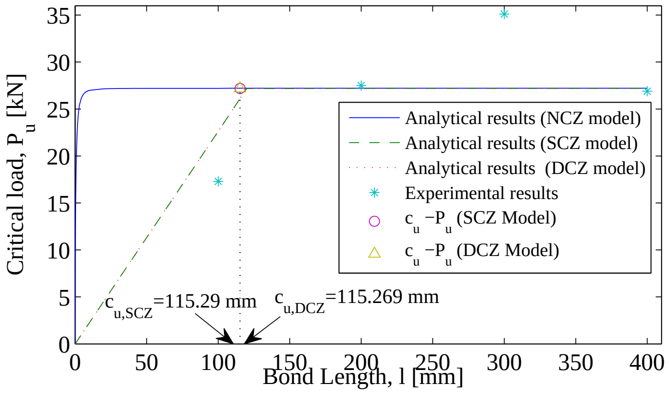

(b) Tests of Taljsten [9]

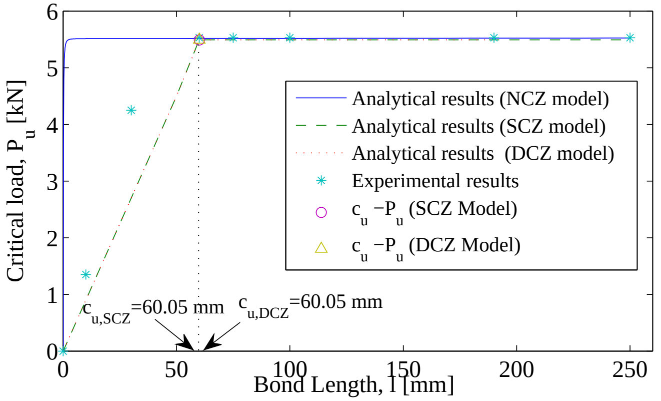

(c) Tests of Yuan *et al.* [25]

Figure 4.15: Ultimate load P_u as a function of the initial bond length l. Predictions of the NCZ, SCZ and DCZ models and comparisons with experimental results.

iii) The DCZ model

There are noteworthy analogies with the SCZ model. A strain driven test can be conducted in order to measure the relative slip of the loaded end of the stiffener for each stage of loading. When the relative slip of the reference point reaches the fracture slip s_f provided by the interface constitutive law (see Figure 4.4), debonding starts and correspondingly the maximum value of the cohesive zone length c_1 is attained, while the cohesive length c_2 undergoes inappreciable changes. The graph showing the ultimate load P_u as a function of l is drawn in Figure 4.14 and Figure 4.15 with dotted line. The limit length of the cohesive zone c_1 is here indicated with $c_{u,\mathrm{DCZ}}$ and evidenced by a triangular marker. Notice that in all the considered cases, the graphs of the SCZ model and of the DCZ model overlap in practice, giving almost the same value of ultimate load and effective bond length, confirming that the influence of the singularity at the free end of the stiffener in the SCZ model is negligible to this respect. The numerical values of the outputs are reported in Table 4.2, where the accuracy of both cohesive models SCZ and DCZ is even more evident.

The main conclusion from this discussion is that the SCZ model is the most convenient engineering approach for the characterization of the joint response, since it involves a reasonable computational effort if compared to that required by the DCZ model.

Finally, it may be useful to compare the values of the EBL just obtained with those obtainable with formulas suggested by technical standards. To this respect, the recent Italian instructions CNR-DT200 [1], which appear to be one of the most modern references, suggest to take EBL= l_e, with

$$l_e = \sqrt{\frac{E_s t_s}{2 f_{ctm}}}\,, \tag{4.34}$$

where f_{ctm} is the mean tensile strength of concrete [65]. The main underlying assumption for (4.34) is a trilinear shear-stress vs. slip model, of the type represented in Figure 4.4, together with the hypothesis of *rigid* substrate. The standard also suggests to evaluate the ultimate load P_{max} through an energetic balance, leading to an expression of the same type of (4.31).

Using the data of Table 4.1, the results from the technical recommendations [1] are also reported in Table 4.2. Notice that the cohesive models, which are not based upon an energetic balance but simply rely upon the calculation of the state of stress with the classical theory of elasticity, give values which are in excellent agreement with the standards for what the ultimate load is concerned. On the other hand, the expression (4.34) seems to *excessively overestimate* the EBL with respect to the experimental data, which are instead very well captured by the proposed cohesive models.

4.6 Discussion

The contact problem between an elastic stiffener and an elastic half-space has been considered to assess the interfacial conditions of detachment in pure mode *II* of the two adherents. Contrarily to the traditional approaches that neglect the

Table 4.2: Results from NCZ, SCZ and DCZ models and comparison with the values predicted by Italian standards [1] and experimental or numerical tests.

	NCZ Model		**SCZ Model**		**DCZ Model**		**CNR-DT200**		**Experiments**	
Test	P_u [kN]	l_e [mm]	$P_{u,SCZ}$ [kN]	$c_{u,SCZ}$ [mm]	$P_{u,DCZ}$ [kN]	$c_{u,DCZ}$ [mm]	P_{max} [kN]	l_e [mm]	$P_{max,e}$ [kN]	$l_{e,e}$ [mm]
Ali Ahmad *et al.* [23]	11.51	-	11.488	69.02	11.491	69.03	11.50	80.08	11.50	$70 \div 90$
Carrara *et al.* [12]	15.10	-	15.095	125.40	15.097	125.45	15.09	185.00	15.11	$120 \div 150$
Chajes *et al.* [8]	12.10	-	12.09	106.30	12.095	106.32	12.09	129.29	12.09	~ 100.00
Mazzotti *et al.* [11]	22.80	-	22.79	92.48	22.78	93.02	22.79	175.33	22.65	~ 100.00
Taljsten [9]	27.22	-	27.18	115.29	27.19	115.27	27.20	175.48	29.83	$100 \div 150$
Yuan *et al.* [25]	5.52	-	5.49	60.05	5.49	60.05	5.51	91.89	5.53	~ 60.00

important role played by elastic deformation of the substrate, here this aspect has been emphasized.

In Chapter 3 the adherents were supposed in perfect contact; in this No-Cohesive-Zone (NCZ) approach, stress singularities are predicted at both extremities of the stiffener. In this chapter, a Single-Cohesive-Zone (SCZ) was introduced at the loaded-end of the stiffener, allowing for relative slip under constant cohesive forces so to annihilate the corresponding stress singularity. Moreover, I have considered a more complicated problem that accounts for a second cohesive region at the free end of the stiffener, such to mitigate also the second singularity. The solutions of this Double-Cohesive-Zone (DCZ) problem, obtained through a Chebyshev expansion, prescribes a continuous interfacial shear stress that never exceeds the cohesive limit.

The potentialities of the three approaches have been discussed. In the NCZ model, the interfacial shear stress shows an extremely rapid decrease from the maximum concentration near the loaded end. The SCZ approach, just assuming a very simple step-wise interface law, predicts the formation of a cohesive zone that produces a more gradual decay of the contact stress in agreement with experimental results. The DCZ model prescribes two cohesive zones at the edges of the reinforcement, but it has been shown that the zone at the free end does not play a significant role. The stress distribution practically coincides with that of the SCZ model, apart from a very small neighborhood of the free end where the singularity is present.

A method has also been proposed to calibrate the parameters that determine the interface shear vs. slip constitutive law of the cohesive models on the basis of simple experimental campaigns. The interface fracture energy G_f can be estimated from the maximum pull-out forces through simple formulas proposed in technical standards [1]. Then, the cohesive parameters can be conveniently calibrated from a series of elementary pull-out tests on specimens with a sufficiently wide range of bond lengths. This is done by requiring the equivalence with the expected value of G_f and the best fitting with the experimental results, trying to capture in particular the limit value of the bond length beyond which no further increase of the pull-out load can be obtained.

Indeed, such limit value is usually referred to as the *Effective Bond Length* (EBL) of the reinforcement. The NCZ model underestimates by far the experimentally measured EBL, because the shear stress at the interface decays too rapidly. The SCZ and the DCZ approaches both give excellent predictions of the EBL, because their shear stress distribution is almost the same except in a small neighborhood of the free-end.

As explained in detail in section 4.3, the SCZ approach allows a complete description of the post-critical response of bonded joints, after delamination has started. A maximal length c_u of the cohesive zone is reached when the relative slip at the loaded end reaches the fracture limit s_f, representing a key parameter of the model. Debonding initiates at this stage at a critical value P_u of the applied load. The length c_u does not change appreciably but simply translates as delamination propagates along the interface, until it reaches the opposite free end. Since the resultant of the cohesive forces only is sufficient to equilibrate almost the whole applied load P, this remains almost constant and equal to P_u during the delamination process. Therefore, the length c_u gives a physical characterization of the EBL, i.e., the length necessary to transfer the load from the stiffener to the substrate. Obviously, increasing the bond length beyond its effective limit does not increase the load bearing capacity, although it increases the ductility of the reinforcement. The length of the ultimate cohesive zone c_u predicted by the DCZ model practically coincides with that of the SCZ model because the length of the second cohesive zone is usually very small, as small is the resultant of the shear stress at the free-end singularity in the SCZ model.

The ultimate load P_u obtained through the three models matches very well not only with experimental results, but also with the relevant formulas proposed in technical standards [1]. For what the effective bond length is concerned, the NCZ is not accurate, but both the SCZ and DCZ models give predictions in good agreement with relevant tests recorded in the literature, here considered for the sake of comparison. On the other hand, it must be observed that the formulas suggested by standards [1] give excessively overestimated values, that in some cases are about twice the experimental results. To this respect, the SCZ and DCZ approaches seem to be an improvement of what proposed so far.

In conclusion the SCZ model, which considers only one cohesive zone and the simplest stepwise interface constitutive law, is able to predict correct values of the critical pull-out load as well as of the EBL. The DCZ model is physically more accurate, but gives in practice identical results, though at a price of much more complicated calculations. In an engineering approach, thus the SCZ formulation appears to be the best compromise.

CHAPTER 5

WEDGE-SHAPED FRACTURING OF SUBSTRATE

This study has been in part developed during a stage at the University of Minnesota, with the supervision of professor Roberto Ballarini.

5.1 Introduction

In order to qualitatively describe the debonding phenomenon in all its phases, in Chapters 3 and 4 the contact problem between an elastic stiffener and an elastic half-space has been considered, emphasizing the role played by the deformation of the substrate on the contrary to the traditional approaches that neglect such a contribution.

We have seen that at the beginning of the loading process, the process zone starts to develop at the loaded end of the stiffener and progresses in a stable manner until it reaches a critical length, indicated by c_u in Figure 4.5B. Indeed, this is reached when the relative slip δ_0 at the loaded end of the bond reaches the crack sliding displacement, s_f, one of the parameters that defines the shear-relative slip constitutive relationship that governs the cohesive zone. Debonding initiates at this stage, at the critical value P_u of the applied load. As it is pulled further, the relative displacement δ_0 between the stiffener and substrate exceeds the limit value s_f and delamination starts. During this phase, corresponding to Figures 4.5C-D, the length c_u does not change appreciably but simply translates as the delamination propagates along the interface, maintaining the load unchanged and equals to P_u, until it reaches the opposite free end.

When the cohesive zone reaches the free end of the stiffener (Figure 4.5E), a strain-softening phase begins. Henceforth the length of the cohesive zone decreases, causing a reduction of the strength of the bond. This phase, sketched in Figure 4.5F, is often associated with a *snapback* response that could not be captured under displacement control. Final failure is produced by the complete separation of the FRP stringer from the substrate. Remarkably, such a failure is characterized by the formation of a characteristic *wedge-shaped* bulb-shaped spall, as shown in Figure 5.1 for a FRP-to-concrete bond. Experiments [34, 12, 67, 68] have provided evidence that the width of this bulb is approximately equal to the width of the FRP lamina. However, its length is independent of the initial length of the reinforcement [34], as evident in Figure 5.1 where various bond lengths have been compared. This phenomenon is true not only for concrete substrates, but also for masonry substrates.

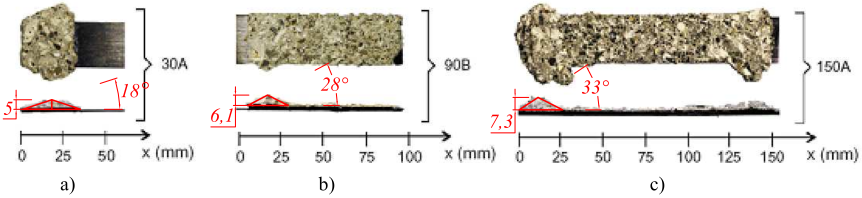

Figure 5.1: Wedge-shaped detached portions of the substrate in FRP-to concrete reinforcement with different initial bond lengths, as *per* [12]. Initial bond length: a) $l = 30$ mm, b) $l = 90$ mm; c) $l = 150$ mm.

The stage at which the bulb forms corresponds to a very small surviving bond length, of the order of $30 \div 50$ mm, and is associated with phase F of Figure 4.5. The bulb is isolated by an inclined crack that initiates at the free end of the stiffener, and whose extension eventually leads to the complete separation of a portion of material from the substrate. To my knowledge, this type of cracking has not been modeled. Thus the present study.

A key hypothesis made here that enables interpretation of the phenomenon is that fractures do not progress continuously and uniformly, but in discrete steps. In other words, there is a *quantized* length for crack propagation, that is attributed to the fact that the characteristic dimensions of the experiment are comparable to those of the microstructure of the substrate material. For the case of artificial conglomerates like concrete, the finite length crack increment is of the same order as the characteristic size of the constituent aggregates. The justification for the hypothesis is that the aggregate represents the most brittle constituent in the concrete mass; when the stress intensity factor of a crack within a portion of an aggregate reaches a critical value, the crack is prone to extend through the whole grain, rather than arrest within it. The granular microstructure of the substrate prevents the possibility of a *continuous* propagation of cracks. This fact is confirmed by experimental evidence. Figure 5.2 shows a concrete surface from which an adherent FRP strip was pulled off. Notice the presence of well-marked grooves on the surface that reflect the discrete steps taken by the advancing crack front. A theory of “quantized fracture mechanics” has been recently proposed in [69] to interpret the size effect in solids made of quasi brittle materials.

Under reasonable simplifying assumptions, a model problem in linear elasticity is now proposed. The stiffener is assumed to transmit shear stresses to a substrate modeled as a homogeneous isotropic elastic half-plane in generalized plane stress. The elastic fields are found by means of the distributed dislocation technique proposed in [71, 72] and developed by different authors [73, 74, 75]. The formulation of the propagation of a crack at the free end of the stiffener relies on the superposition of two effects: *i*) the effect of tangential forces *per* unit area on the surface of the half plane and *ii*) the effect of distributed edge dislocations along the crack reference configuration. The condition that the crack lips are traction-free

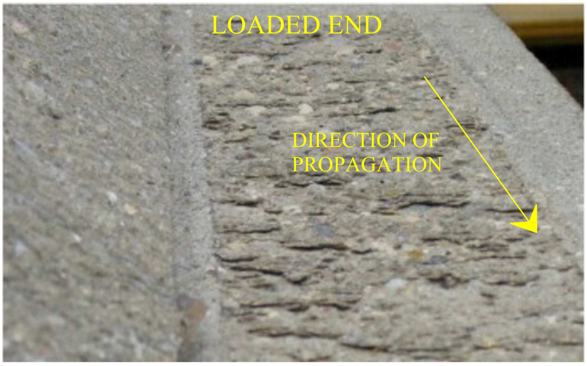

Figure 5.2: Detail of the surface of a concrete support after delamination of the FRP strip [70].

furnishes an integral equation, which is solved using the properties of Chebyshev polynomials.

In the proposed model, two competing mechanisms of degradation may occur: *a*) failure of the adhesive joint, which progresses at the stiffener-substrate interface when the corresponding shear stress is greater than the strength of the interface itself; *b*) inclined cracking, which can develop in the substrate when the strain energy release associated with its (quantized) propagation is greater than the corresponding fracture energy of the material. From the competition between the two mechanisms one can evaluate when the inclined crack starts to form and the characteristic angle of the wedge-shaped bulb. The proposed model problem represents a simple and intuitive tool to investigate this peculiar phenomenon and provides results that are in very good qualitative agreement with experiments drawn from the technical literature.

5.2 The model problem

A simple Linear Elastic Fracture Mechanics model amenable of an analytical treatment is now presented. It relies on a few simplifying assumptions.

5.2.1 Preliminary considerations

The detachment of a bulb from the substrate occurs in the latest stage of the debonding process, where the surviving bond length is very small, of the order of $30 \div 50$ mm. In the schematic representation of Figure 4.5, this stage is associated with phase F. The characteristic wedge-like shape of the bulb, represented in Figure 5.1, is due to the nucleation of an inclined crack that initiates at the free end of the stiffener, and eventually induces the complete separation of that portion of the substrate.

In general, the stiffener is a very thin strip or plate, with negligible bending stiffness. Therefore, peeling stresses at the interface are absent because the stiffener is not able to equilibrate transverse loads during small deformations. Thus the only relevant contact stresses are the shear stresses acting at the stiffener-substrate interface [76]. There is general agreement that the strength of the adhesive joint can be characterized through a shear-bond-stress "τ" *vs.* relative-slip "s" constitutive law. The $\tau - s$ curve is evaluated by measuring experimentally the strain in the stiffener and the substrate [23]. The typical response is illustrated in Figure 4.4: the quasi-linear branch leading to the peak stress is followed by a strain-softening phase that ends at the zero-stress level associated with complete debonding. This curve can be approximated by three straight lines [1]; an ascending branch up to the peak stress τ_f; a linear strain-softening phase approaching $s = s_f$ where $\tau = 0$ and, finally, a zero-stress *plateau*. In certain cases, to interpret the gradual debonding process, it is sufficient to consider a simple step-wise approximation of such a constitutive law [76, 77] with equal fracture-energy G_f and critical crack sliding displacement s_f, so that the maximum shear stress is $\tau_c = \frac{1}{2}\tau_f$. But if the bond length is very small, as it is in the final stage of the debonding process, then the relative displacement at the extremities is moderate. Consequently, one can neglect the strain gradient and assume that the slip is uniform. The consequence is that the interfacial shear stress transmitted by the stiffener to the substrate can be considered constant over the entire bond length.

The initiation of the inclined crack is sketched in Figure 5.3(a) for a bond length that reaches the critical value l. Observe that when a crack of length a, inclined by the angle ω, forms at the free end of the stiffener, a wedge-shaped prism is formed within the substrate. This suggests that the substrate stiffness is locally degrading in the neighborhood of the crack.

As a first order approximation, the effect of the elastic deformation of the substrate can be modeled by a set of shear springs *à là* Winkler, which connect the stiffener to a support now supposed infinitely rigid. This scheme is represented in Figure 5.3(b). But if a portion of the substrate locally yields because of the formation of the inclined crack, then the stiffness of the springs tends to zero in a neighborhood of such a portion. Consequently, there is a local release of the stiffener, which must be taken into account.

To give a quantitative interpretation, one may consider the problem of an elastic half plane in generalized plane stress, with a crack of length a inclined by the angle ω. A uniformly-distributed shear stress q is applied on the free surface of the half-space, for a length l starting from the crack origin, to represent the contact stress transmitted by the stiffener over its *whole* bond length. The elasticity problem is solved using the method presented in Section 5.2.2 and the corresponding solution is recorded in Appendix C. The normal component of strain ε_{rr} in the direction of the surface of the half-plane, derived according to equations (C.7) and (C.12a), is drawn in Figure 5.4 as a function of the normalized abscissa $\xi/(a\cos\omega)$, indicated in Figure 5.3(a). Apart from a neighborhood of $\xi = 0$, the analytical solution is in perfect agreement with the results of numerical simulations performed with the FEM program Abaqus [78], also reported in the same figure for the sake of comparison.

The analytical solution predicts a strain singularity at $\xi = 0^+$; then the strain remains almost constant for $0 < \xi/(a\cos\omega) < 1$. Moreover, one finds that the strain energy becomes infinite as the angle ω tends to zero. It should be observed that over the wedge-shaped portion isolated from the substrate by the inclined crack (Figure 5.3(a)), the state of stress is similar to that associated with the

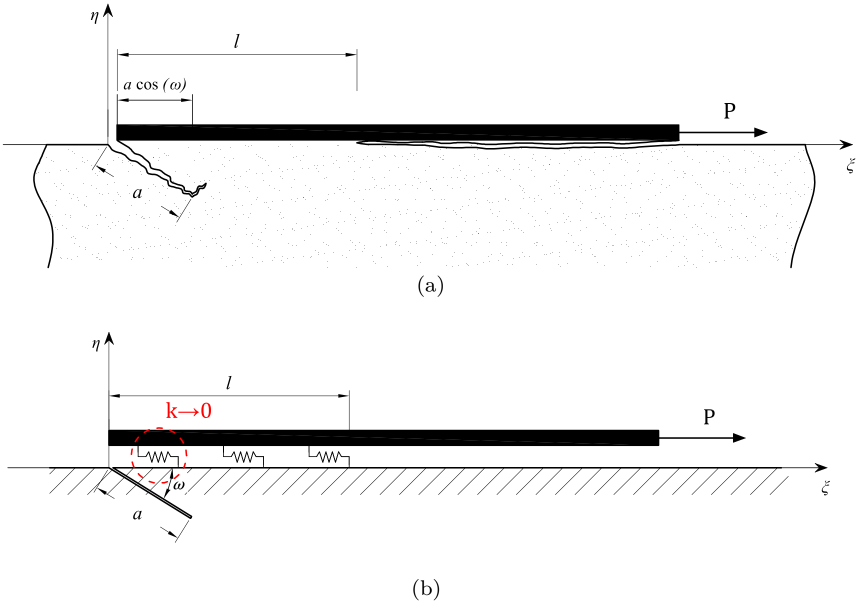

Figure 5.3: A finite stiffener bonded to the boundary of a semi-infinite plate. a) Edge crack forming at the free end of the stiffener; b) Simplified scheme with a set of shear springs *à là* Winkler.

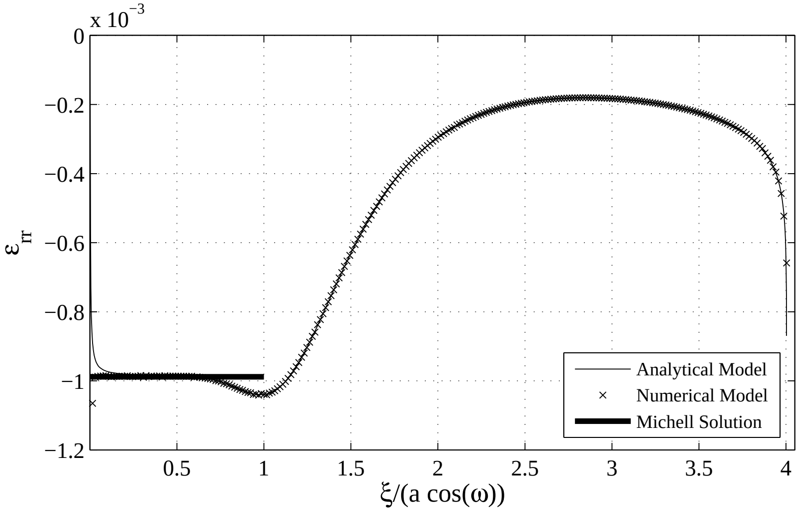

Figure 5.4: Elastic half plane with an inclined crack, loaded by a uniformly distributed load for a prescribed length. Normal component of strain at right angle to the surface of the half-space, as a function of the normalized abscissa $\xi/(a\cos\omega)$. Elastic solution, numerical results, approximate Michell solution.

Michell problem of a long wedge subjected to shear loading along one of the sides [79], as represented in Figure 5.5. The solution by Michell, whose relevant results are given in Appendix C (eqs. (C.11) and (C.12a)), prescribes a constant strain that fits very well with the analytical solution and the numerical experiments in the range $0 < \xi/(a\cos\omega) < 1$, as represented in Figure 5.4. Of course when $\omega \to 0$ the wedge angle is null, and the displacement becomes infinite: this is the reason why the elastic strain energy becomes unbounded.

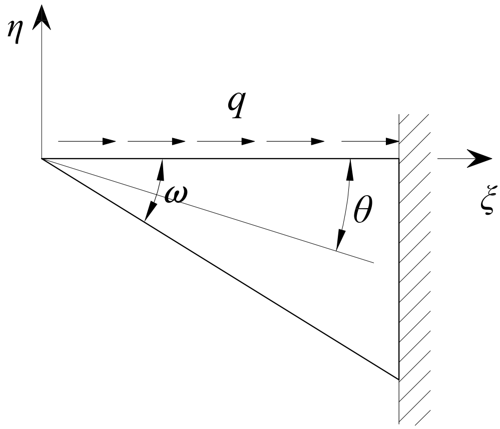

Figure 5.5: Michell problem of a wedge, loaded along one side by shear stresses.

It is important to note that the strain over the portion $0 \leq \xi/a\cos(\omega) \leq 1$ is much higher (in absolute value) than in the remaining part of the bond length. For the case considered in Figure 5.4, representative of a typical condition ($l = 52$ mm, $a = 15$ mm, $\omega = 30°$, $q = 3.85$ MPa), the strain in the neighborhood of the crack is more than five times higher than the strain in the remaining portion. Consequently, in the simplified scheme of Figure 5.3(b), the stiffness of the springs on that left-hand-side portion would be about 20% of the stiffness of the others. Deriving an analytical solution to the actual contact problem of an elastic stringer bonded to an elastic half space with an inclined crack is a formidable task that is not attempted here. Instead, with the aim at a qualitative description of the phenomenon, the following assumptions are made to achieve a reasonable first-order approximation:

- the stringer is only able to transmit shear contact stress because of its small stiffness, which annihilates its bending strength;
- the shear contact stress is constant, because the actual bond length of the stringer in the latest stage of the debonding process is so small that one can assume that the stiffener-substrate relative slip is constant;
- the shear contact stress is null in the interval $0 \leq \xi/a\cos(\omega) \leq 1$; in fact, one can neglect the stiffness offered by the substrate in that portion because of the formation of the inclined crack.

In conclusion, the elasticity problem that will be considered is that represented in Figure 5.6. Here, a linear-elastic, homogenous and isotropic half-plane in generalized plane stress, with an inclined crack initiating at $\xi = 0$, is loaded by an uniformly distributed shear stress q on the interval $a\cos(\omega) \le \xi \le l$.

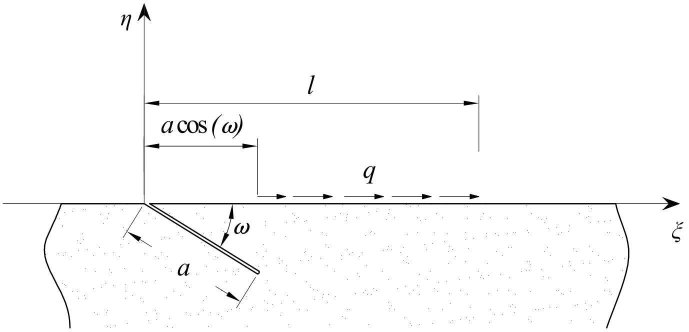

Figure 5.6: Model problem for a finite stiffener bonded to the boundary of an elastic half-space, where an inclined fracture forms.

Observe that all the aforementioned hypotheses are required, without exception, for a simple but complete description of the phenomenon. In particular, it is crucial to consider that there is a local weakening of the substrate in the neighborhood of the inclined crack. Here I made the simplifying, quite drastic, assumption that the shear contact stress is null in the interval $0 \le \xi/a\cos(\omega) \le 1$. Of course, more refined considerations could be made, but the simplicity of the analytical solutions would be lost. Comparison with numerical experiments where no simplifying assumption is made will be the subject of further work.

5.2.2 Governing equations in linear elasticity theory

The problem in linear elasticity represented in Figure 5.6 can be formulated in terms of the complex Muskhelishvili potentials [80]. With respect to a system of polar coordinates as in Figure 5.7(a), centered at $\xi = \eta = 0$, the components of stress in polar coordinates can be expressed in terms of two analytic functions $\Phi(z)$ and $\Psi(z)$ of the complex variable $z = \xi + i\eta = re^{i\vartheta}$ as

$$\sigma_{rr} + \sigma_{\vartheta\vartheta} = 4\mathrm{Re}[\Phi(z)], \tag{5.1a}$$

$$\sigma_{\vartheta\vartheta} - \sigma_{rr} + 2i\sigma_{r\vartheta} = 2e^{2i\vartheta}[\bar{z}\Phi'(z) + \Psi(z)], \tag{5.1b}$$

$$\sigma_{\vartheta\vartheta} + i\sigma_{r\vartheta} = \Phi(z) + \overline{\Phi(z)} + e^{2i\vartheta}[\bar{z}\Phi'(z) + \Psi(z)], \tag{5.1c}$$

in which $i = \sqrt{-1}$, μ is the shear modulus, $\kappa = 3 - 4\nu$ for plane strain and $\kappa = (3-\nu)/(1+\nu)$ for generalized plane stress, ν is the Poisson's ratio. Moreover, $(\cdot)'$ denotes differentiation with respect to z and $\overline{(\cdot)}$ implies complex conjugation. The normal and shear components of stress must be zero on the crack surfaces, i.e.,

$$\sigma_{\vartheta\vartheta} + i\sigma_{r\vartheta} = 0, \ \text{for } \vartheta = -\omega, \ 0 \le r \le a, \tag{5.2}$$

and must agree with the boundary conditions on the surface of the half space.

In the distributed dislocation approach, the problem can be reduced to that of an elastic half-plane containing a distribution of edge dislocations on $\vartheta = -\omega$, $0 \leq r \leq a$, as described in Figure 5.7(a), and tangential stress $q(\xi)$ applied over the portion $\vartheta = 0$, $a\cos(\omega) \leq r \leq l$, as indicated in Figure 5.7(b).

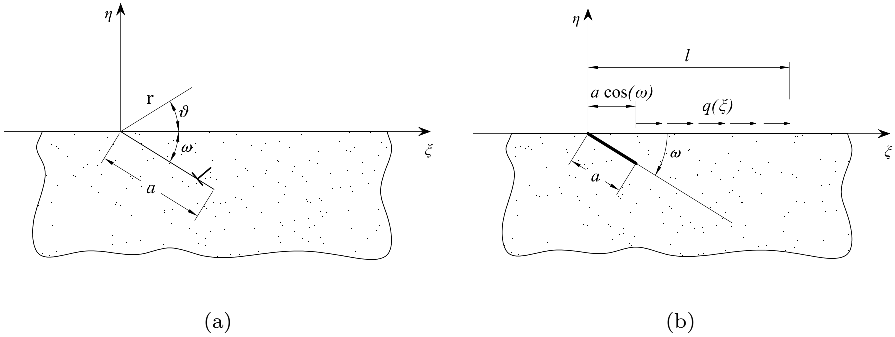

Figure 5.7: Superposition effects: a) distributed edge dislocation; b) effect of surface tangential stress.

Equation (5.2) can then be written as

$$(\sigma_{\vartheta\vartheta} + i\sigma_{r\vartheta})^{(d+q)} = (\sigma_{\vartheta\vartheta} + i\sigma_{r\vartheta})^{d} + (\sigma_{\vartheta\vartheta} + i\sigma_{r\vartheta})^{q} = 0, \quad \text{for } \vartheta = -\omega, \quad 0 \leq r \leq a, \tag{5.3}$$

where the apexes d and q indicate the contribution of dislocations and shear stresses, respectively.

5.2.2.1 Problem I: elastic half-plane with edge dislocations

Consider a straight crack of length a at an angle $\vartheta = -\omega$ in an elastic half plane $\eta < 0$, as indicated in Figure 5.8. The functions $\Phi(z)$ and $\Psi(z)$ are holomorphic in this region. If z is a point of the lower half-plane, clearly $\bar{z}$ is its mirror image in the upper half-plane.

The solution of the problem of one edge dislocation in an elastic homogenous half-space is known [80, 71]. It can be represented in complex variables form using the analytic continuation procedure. The complex potentials given by

$$\Phi_{dw}(z) = \frac{\beta}{z - z_0}, \qquad \Psi_{dw}(z) = \frac{\overline{\beta}}{z - z_0} + \frac{\beta \bar{z}_0}{(z - z_0)^2}, \tag{5.4}$$

define the elastic solution at any point z for a *dislocation* acting at point z_0 in a *whole* elastic plane. The constant β is defined as

$$\beta = \frac{\mu}{\pi i(\kappa + 1)} [b_r + i b_\vartheta] \frac{z_0}{|z_0|}, \tag{5.5}$$

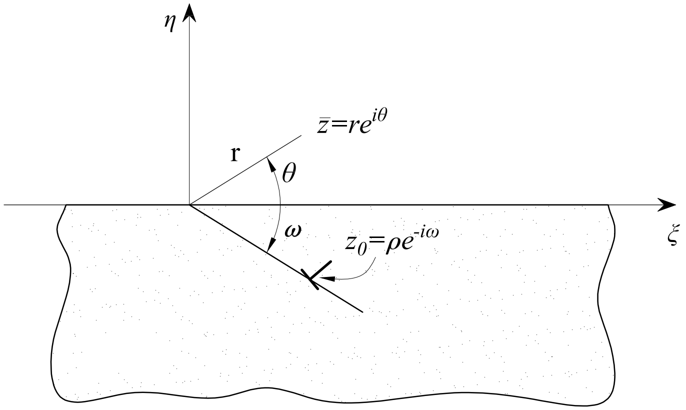

Figure 5.8: An edge dislocation in a half space. Representative variables.

where b_r and b_ϑ represent the radial and circumferential components of the Burgers vector and μ is the shear modulus.

These potentials produce non-zero tractions along the line representing the free surface of the half-plane. To clear these, an additional set of complex potentials need to be added. These are determined using the analytic continuation of (5.4) through the boundary of the half plane [80], and recalling the properties $\overline{\Phi}(z) = \overline{\Phi(\bar{z})}$, and $\overline{\Phi}(\bar{z}) = \overline{\Phi(z)}$. In conclusion, one finds that the potential Φ in the half plane $\mathrm{Im}(z) \leq 0$ reads

$$\Phi_{dc}(z) = -\overline{\Phi_{dw}(\bar{z})} - z\overline{\Phi'_{dw}(\bar{z})} - \overline{\Psi_{dw}(\bar{z})}. \tag{5.6}$$

For the particular case of a half plane with zero tractions on the boundary, using symmetry considerations, one can demonstrate [80] that the expression (5.1c) can be simplified and results to be a function of the potential $\Phi(z)$ only. In particular, one finds

$$\sigma_{\vartheta\vartheta} + i\sigma_{r\vartheta} = \overline{\Phi(z)} + (1 - e^{-2i\omega})\Phi(z) + (\bar{z} - z)e^{-2i\omega}\Phi'(z) - e^{-2i\omega}\overline{\Phi}(z). \tag{5.7}$$

By setting in this expression $\Phi(z) = \Phi_{dw}(z) + \Phi_{dc}(z)$, as *per* (5.4) and (5.6), one obtains the desired solution.

The discrete dislocation at $z_0 = \rho e^{-i\omega}$ can be replaced by a distribution of dislocations, $B(\rho)d\rho$, of the form

$$B(\rho) = \frac{\mu}{\pi i(\kappa + 1)} \frac{\partial}{\partial \rho}[b_r + ib_\vartheta]e^{-i\omega}. \tag{5.8}$$

In this way, maintaining fixed ω and integrating over the length of the crack a, the relevant stresses on the radial line $z = re^{-i\omega}$ (Figure 5.8) due to the distributed dislocations become

$$(\sigma_{\vartheta\vartheta} + i\sigma_{r\vartheta})^d = \int_0^a B(\rho)K_1(r,\rho)d\rho + \int_0^a \overline{B(\rho)} \left[\frac{2e^{-i\omega}}{r-\rho} + K_2(r,\rho)\right] d\rho, \quad (5.9)$$

where $K_1(r,\rho)$ and $K_2(r,\rho)$ are given in Appendix B.

5.2.2.2 Problem II: elastic half-plane under surface tangential stress

In the problem of Figure 5.9, a distribution of shear stresses $q(\xi)$, positive if directed towards the positive $\xi-$axis, is applied on the surface over the length $l_c = l - a\cos\omega$.

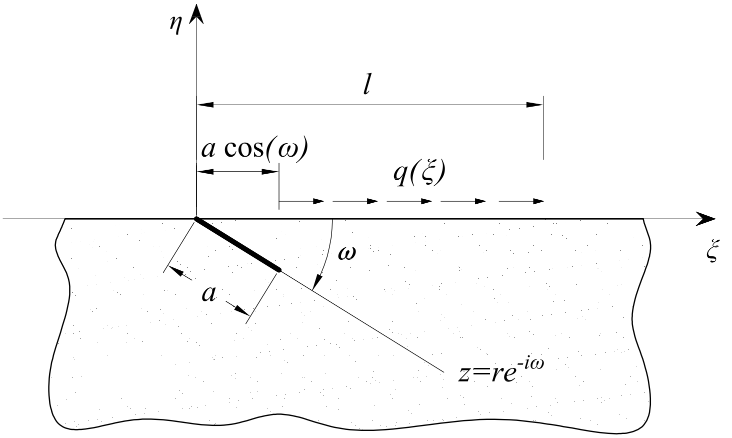

Figure 5.9: Elastic half-plane under surface shear stress. Representative variables.

The complex potentials for the *uncracked* half plane are given by

$$\Phi_q(z) = -\frac{1}{2\pi}\int_{a\cos\omega}^{l} \frac{q(\xi)}{\xi - z}d\xi, \quad (5.10a)$$

$$\Psi_q(z) = \frac{1}{2\pi}\int_{a\cos\omega}^{l} \frac{q(\xi)}{\xi - z}d\xi - \frac{1}{2\pi}\int_{a\cos\omega}^{l} \frac{q(\xi)}{(\xi - z)^2}\xi d\xi. \quad (5.10b)$$

The relevant stresses on the radial line $z = re^{-i\omega}$ ($\bar{z} = re^{i\omega}$) of Figure 5.9, can be obtained by substituting equations (5.10) in (5.7), to give

$$(\sigma_{\vartheta\vartheta} + i\sigma_{r\vartheta})^q = \frac{1}{2\pi}\left[\int_{a\cos\omega}^{l} \overline{q(\xi)}H_1(r,\xi)d\xi + \int_{a\cos\omega}^{l} q(\xi)H_2(r,\xi)d\xi\right], \quad (5.11)$$

where $H_1(r,\xi)$ and $H_2(r,\xi)$ are given in Appendix B.

5.3 Solution of the elastic problem

Taking into account the contributions of the two systems considered in sections 5.2.2.1 and 5.2.2.2, the condition of traction free crack surface (5.3) reads

$$\int_0^a B(\rho)K_1(r,\rho)d\rho + \int_0^a \overline{B(\rho)}\left[\frac{2e^{-i\omega}}{r-\rho} + K_2(r,\rho)\right]d\rho \\ + \frac{1}{2\pi}\left[\int_{a\cos\omega}^{l} \overline{q(\xi)}H_1(r,\xi)d\xi + \int_{a\cos\omega}^{l} q(\xi)H_2(r,\xi)d\xi\right] = 0. \quad (5.12)$$

5.3.1 Approximation in Chebyshev's series

The integral equation (5.12) can be solved using the method suggested by Erdogan and Gupta in [58], which exploits the properties of Chebyshev polynomials of the first and the second kind[9]. These polynomials are traditionally defined in the interval $[-1,1]$, so that it is convenient to change variables according to the transformations

$$\rho = \frac{a}{2}(t+1), \quad (5.13a)$$

$$r = \frac{a}{2}(s+1), \quad (5.13b)$$

$$\xi = a\cos\omega + \frac{(l-a\cos\omega)}{2}(\zeta+1), \quad (5.13c)$$

to obtain

$$\int_{-1}^1 B(t)K_1(s,t)dt + \int_{-1}^1 \overline{B(t)}\left[\frac{2e^{-i\omega}}{s-t} + K_2(s,t)\right]dt \\ + \frac{1}{2\pi}\left[\int_{-1}^1 \overline{q(\zeta)}H_1(s,\zeta)\,d\zeta + \int_{-1}^1 q(\zeta)H_2(s,\zeta)\,d\zeta\right] = 0, \quad (5.14)$$

where $K_1(s,t)$, $K_2(s,t)$, $H_1(s,\zeta)$ and $H_2(s,\zeta)$ are reported in Appendix B.

Observe that the kernels $K_1(s,t)$ and $K_2(s,t)$ appearing in the integrals of equation (5.14) are not regular at all points of the crack, as can be seen from equations (B.8) and (B.9). They become infinite as both s and t approach the mouth of the crack ($s,t \to -1$). The integral equations are referred to as having Generalized Cauchy kernels and the Gauss Chebyshev quadrature for standard Cauchy integral equations does not apply. It is necessary to examine the behavior of the functions $B(t)$ at the ends $t = \pm 1$.

We argue that at the crack mouth the order of the singularity is weaker than the square root type, and thus we force the regular part of the dislocation density at the crack mouth to be zero, i.e.,

---

[9] The definition and properties of Chebyshev polynomials that are used here, have been summarized in Appendix A.

$$B(-1) = 0. \tag{5.15}$$

It has been demonstrated that such treatment of the mouth of the edge crack produces sufficiently accurate stress intensity factors for the range of angles considered in this study.

For the reasons explained at length in Section 5.2.1, one can assume that the surface stress $q(\xi)$ is constant over the length l_c, i.e., $q(\xi) = \text{const.} = q$. In this situation, equation (5.14) becomes

$$\int_{-1}^{1} B(t)K_1(s,t)dt + \int_{-1}^{1} \overline{B(t)} \left[\frac{2e^{-i\omega}}{s-t} + K_2(s,t)\right] dt + \frac{q}{2\pi}\int_{-1}^{1} \left[H_1(s,\zeta) + H_2(s,\zeta)\right] d\zeta = 0. \tag{5.16}$$

Such a singular integral equation can be solved by representing the dislocation density $B(t)$ in terms of a regular function $B_{\text{reg}}(t)$ and a function $w(t)$ with proper singularities at the end points, of the form

$$B(t) = B_{\text{reg}}(t)w(t) = \frac{B_{\text{reg}}(t)}{\sqrt{1-t^2}}, \tag{5.17}$$

where $B_{\text{reg}}(t)$ is bounded. The regular function can be expressed in terms of the Chebyshev polynomials of the first kind T_j as

$$B_{\text{reg}}(t) = \sum_{j=0}^{n} X_j T_j(t), \tag{5.18}$$

where X_j are *complex* coefficients. Substituting (5.17) and (5.18) in (5.16), setting $\widehat{B}_{\text{reg}} = B_{\text{reg}}/(q_c/(2\pi))$, and using the properties of Chebyshev polynomials, one obtains the discretized form of the integral equation as

$$\frac{\pi}{n}\sum_{k=1}^{n} \widehat{B}_{\text{reg}}(t_k)K_1(s_j,t_k) + \frac{\pi}{n}\sum_{k=1}^{n} \overline{\widehat{B}_{\text{reg}}(t_k)} \left[\frac{2e^{-i\omega}}{s_j-t_k} + K_2(s_j,t_k)\right] + sgn(q)\frac{\pi}{n}\sum_{k=1}^{n} \left[H_1(s_j,\zeta_k) + H_2(s_j,\zeta_k)\right] = 0,\ j = 1,...,n-1, \tag{5.19}$$

where $t_k = \cos\varphi_k$, $s_j = \cos\vartheta_j$ and $\zeta_k = \cos\delta_k$, while the integration and collocation points

$$\begin{cases} \varphi_k = \delta_k = \frac{(2k-1)\pi}{2n} & k = 1,...,n, \\ \vartheta_j = \frac{j\pi}{n} & j = 1,...,n-1, \end{cases} \tag{5.20}$$

represent the roots of the Chebyshev polynomials of the first and second kind, respectively. Condition

$$\widehat{B}_{\mathrm{reg}}(-1) = 0\,, \tag{5.21}$$

has to be added in order to fulfill (5.15).

5.3.2 Stress intensity factors

At the apex of the inclined crack, the complex stress intensity factor $K = K_I + iK_{II}$, comprehensive of mode I and mode II opening, is given by

$$K = K_I + i\,K_{II} = \lim_{r\to a}(\sigma_{\vartheta\vartheta} + i\sigma_{r\vartheta})^{(d+q)}\sqrt{2\pi(r-a)}. \tag{5.22}$$

It can be shown that the only unbounded part of the integral equation (5.12) is the one involving the Cauchy Kernel, so that

$$K = K_I + i\,K_{II} = \lim_{r\to a}\left[\int_0^a \overline{B(\rho)}\frac{2e^{-i\omega}}{r-\rho}\,d\,\rho\right]\sqrt{2\pi(r-a)}. \tag{5.23}$$

In terms of the dimensionless quantities introduced in the previous section, equations (5.17) and (5.18), together with the properties[10] of Chebyshev polynomials of the first kind for $|s| > 1$, the relevant expression reads

$$K = K_I + i\,K_{II} = \frac{q}{2}\sqrt{2\pi a}e^{-i\omega}\sum_{j=0}^{n}\overline{X}_j, \tag{5.24}$$

or, equivalently,

$$K = K_I + i\,K_{II} = \frac{q}{2}\sqrt{2\pi a}e^{-i\omega}\overline{\widehat{B}_{\mathrm{reg}}}(1), \tag{5.25}$$

which can be made normalized as

$$K_n = \frac{K}{q\sqrt{2\pi a}} = \frac{1}{2}e^{-i\omega}\sum_{j=0}^{n}\overline{X}_j = \frac{1}{2}e^{-i\omega}\overline{\widehat{B}_{\mathrm{reg}}}(1). \tag{5.26}$$

The value of the function $B(t)$ at the end points $t = \pm 1$ is given by the interpolation formulas [72, 81]

---

[10] See Appendix A.

$$B(1) = \frac{1}{n}\sum_{k=1}^{n} \frac{\sin\left[\frac{2k-1}{4n}\pi(2n-1)\right]}{\sin\left[\frac{2k-1}{4n}\pi\right]} B(t_k), \tag{5.27a}$$

$$B(-1) = \frac{1}{n}\sum_{k=1}^{n} \frac{\sin\left[\frac{2k-1}{4n}\pi(2n-1)\right]}{\sin\left[\frac{2k-1}{4n}\pi\right]} B(t_{n+1-k}). \tag{5.27b}$$

Figure 5.10 shows the stress intensity factors K_I (Figure 5.10(a)) and K_{II} (Figure 5.10(b)), evaluated through equation (5.25), as a function of the angle ω for different values of the crack length a and a fixed bond length of the stiffener. Both figures have been obtained using the mechanical parameters of [12], whose values are reported later in Table 5.1.

It should be noted that in order to achieve a good approximation the number n of Chebyshev terms that are needed in the series to define K, strongly increases as ω decreases, i.e., as the crack tends to be parallel to the surface. This is shown in Figure 5.11, which plots the normalized stress intensity factors $K_{I,n}$ and $K_{II,n}$, evaluated through equation (5.26), as a function of ω for varying n. For the sake of comparison the graph also reports the results obtained using FEM program Abaqus [78]. Observe that, for $\omega > 20°$, 100 terms are sufficient to obtain a very good approximation, but for small values of ω, at least 300 terms are necessary to avoid the classical "fluctuations", as evidenced in Figure 5.11(b).

5.4 Competing mechanisms of failure

In a pull-out test, debonding starts from the loaded end of the stiffener and progresses parallel to its axis (Figure 4.5). When the actual bond length reaches a critical value the formation of an inclined crack, nucleated at the free end, becomes more favorable than continued debonding. There is thus a competition between two different failure mechanisms, summarized in Figure 5.12: interface debonding and crack diving into the substrate.

When at the loaded end, the interfacial tangential stresses become greater than the maximum allowable tangential stress for the interface, q_0, namely when

$$\tau \geq q_0, \tag{5.28}$$

interface debonding occurs and, consequently, fracture propagates parallel to the adhesive joint.

On the other hand, for the inclined crack of length a and inclination ω that progresses from the free end of a stiffener, the energy release rate is obtained from its stress intensity factors by using Irwin's relation

$$G_\omega(a) = \frac{\left(K_{I,\omega}(a)\right)^2 + \left(K_{II,\omega}(a)^2\right)}{\overline{E}_p}, \tag{5.29}$$

where $\overline{E}_p = E_p$ for plane stress, $\overline{E}_p = E_p/(1-\nu^2)$ for plane strain, and in the notation I have emphasized the dependence upon ω and a. When the crack length

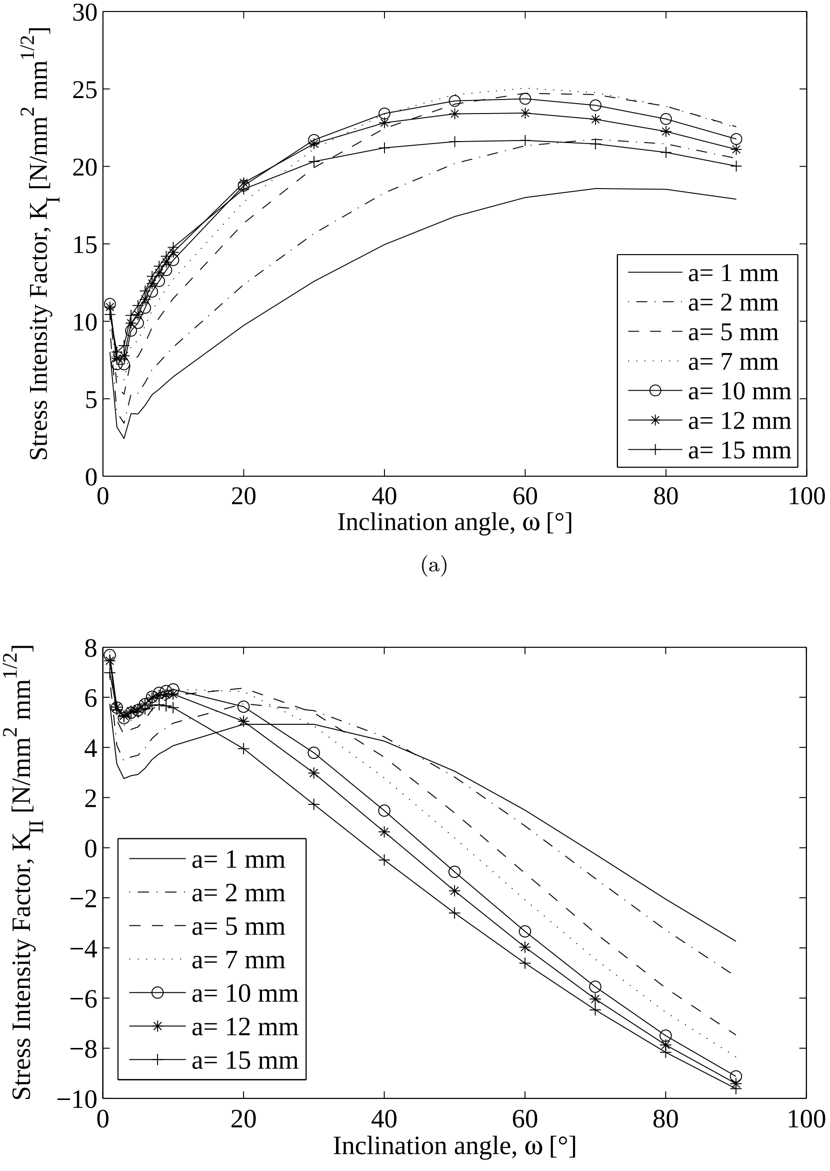

(a)

(b)

Figure 5.10: Stress intensity factors at the tip of the crack for different values of crack length a and a fixed $l = 30$ mm (mechanical properties of [12]). Stress intensity factor in: a) Mode I; b) Mode II.

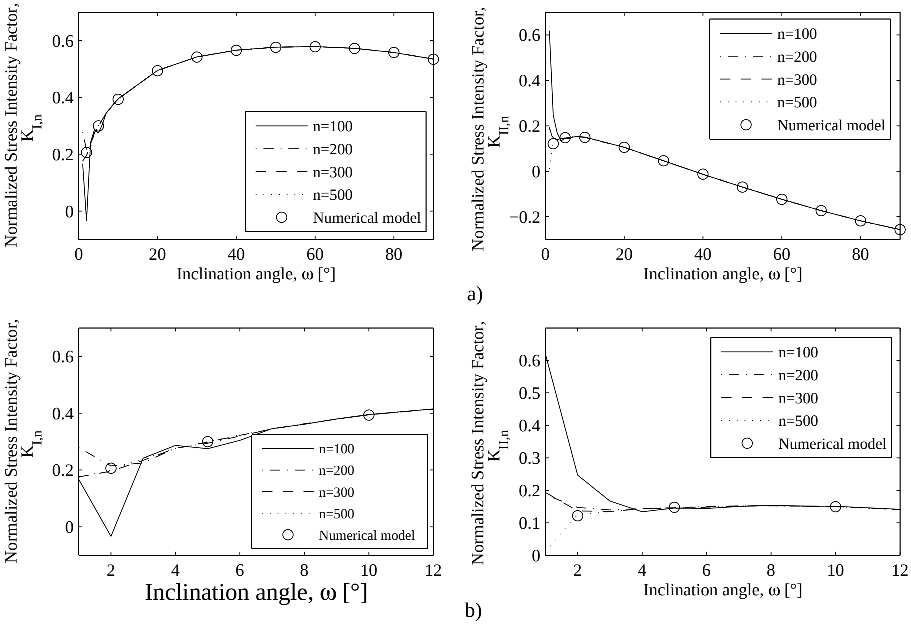

a)

b)

Figure 5.11: Normalized stress intensity factors at the tip of the crack as a function of the angle ω (mechanical parameters of [12]: $l = 30$ mm and $a = 15$ mm). a) Influence of the number n of terms of the Chebyshev expansion. b) Detail in the interval $1° \leq \omega \leq 12°$.

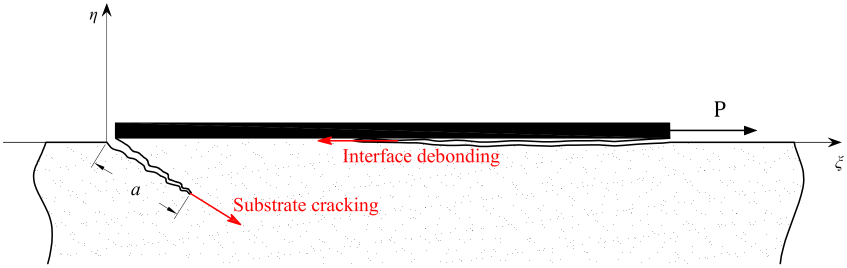
η
ξ
P
a
Interface debonding
Substrate cracking

Figure 5.12: Competing mechanisms of failure in a pull out test of a stringer bonded to a substrate.

passes from the value $a = a_1$ to $a = a_2 > a_1$, the corresponding energy release reads

$$\Delta G_{\omega, a_1 \to a_2} = \int_{a_1}^{a_2} G_\omega(a)\, da\,. \tag{5.30}$$

One of the major assumptions in the present theory is that fracture propagation is *quantized*, i.e., crack progress in steps (*quanta*) of finite length, which are of the same order of the material intrinsic length scale. Let a^* represent such a quantum, and suppose that the toughness of the substrate is defined by the fracture energy *per* unit area Γ. Then, the *quantized nucleation* of the crack at the free end of the stiffener is governed by an energetic balance *à là* Griffith that reads

$$\int_0^{a^*} G_\omega(a)\, da = \Gamma a^*\,. \tag{5.31}$$

In other words, the crack propagates when

$$G^*_\omega \geq \Gamma, \text{ with } G^*_\omega = \frac{1}{a^*}\int_0^{a^*} G_\omega(a)\, da. \tag{5.32}$$

In general G^*_ω is a quadratic function of the stress intensity factors and, consequently, it is a quadratic function of the shear stress τ transmitted by the stiffener to the substrate. One can normalize such a quantity and write $G^*_\omega = G^*_{\omega,n}\tau^2$, so that equation (5.32) can be written in the equivalent form

$$\tau^2 \geq \frac{\Gamma}{G^*_{\omega,n}}. \tag{5.33}$$

Comparing such an expression with (5.28), the competition between the two mechanisms of Figure 5.12 can be summarized in the following conditions

$$\begin{cases} \tau^2 \geq \Gamma / G^*_{\omega,n}, & \Rightarrow \textit{crack propagation in the substrate,} \\ \\ \tau^2 \geq q_0^2, & \Rightarrow \textit{interface debonding.} \end{cases} \tag{5.34}$$

Combining these expressions, following the same rationale proposed by [82], one obtains

$$\begin{cases} G^*_{\omega,n}\, q_0^2/\Gamma > 1, & \Rightarrow \textit{crack propagation in the substrate,} \\ \\ G^*_{\omega,n}\, q_0^2/\Gamma < 1, & \Rightarrow \textit{interface debonding,} \\ \\ G^*_{\omega,n}\, q_0^2/\Gamma = 1, & \Rightarrow \textit{the two mechanisms are equivalent.} \end{cases} \tag{5.35}$$

The importance of (5.35) is that it provides a comparison which is independent on the applied shear stress τ. The value of the non-dimensional quantity $G^*_{\omega,n}\, q_0^2/\Gamma$ directly indicates which one of the mechanisms of Figure 5.12 is the most favorable when the stiffener is pulled until some damage occurs. When $G^*_{\omega,n}\, q_0^2/\Gamma$ is less than 1, propagation along the interface (debonding) occurs first; when it is greater than 1, formation of an inclined crack is privileged; when it is equal to 1, both mechanisms are equivalent.

5.5 Comparison with experiments

In order to make a comparison with experiments, reference is made to the two campaigns of pull-out tests recorded in [34] and [12]. Carbon Fiber Reinforced Polymer (CFRP) strips were bonded to concrete prisms and subjected to simple pull out tests with a closed loop control that allowed the capture of snap-back instabilities. Typical specimen size and measured mechanical properties for the materials used in such tests are reported in Table 5.1.

As already discussed in Section 5.2.1, it is commonly accepted that the adhesive joint can be characterized by an interface constitutive law of the type represented in Figure 4.4, correlating the shear bond-stress τ with the relative slip s of the two adherents through the adhesive. Supposing that the slip between the two adherents is constant in practice, from the constitutive law of Figure 4.4 it is possible to consider a definite value for the shear stress transmitted by the stiffener to the substrate. Failure in the bond occurs when such stress reaches the critical value, which has been indicated with q_0 in Section 5.4.

The correct choice of q_0 deserves some comments. One could directly refer to the peak value τ_f of Figure 4.4, which is certainly associated with failure of the interface, but there are some uncertainties in the experimental evaluation of the $\tau - s$ constitutive law. This is assessed by estimating the slip s by measuring, by means of gages, the strains in the stiffener and in the substrate. However, in the latter case the measurement cannot be made immediately below the stiffener, but instead it is made at one of its sides [23]. Moreover, as evident from Figure 5.2, debonding is not a smooth process and the concrete substrate always present noteworthy inhomogeneities that render any constitutive law valid only at the qualitative level.

In the theory of debonding presented in [76, 77], a simple step-wise approximation of the constitutive law of Figure 4.4 has been sufficient to represent the debonding process in very good agreement with the experimental results. Therefore, I suggest to set also here $q_0 = \tau_c$, where $\tau_c = \tau_f/2$ represents an average value of the bond strength and corresponds to the maximum stress in a stepwise approximation that preserves the same fracture energy of the joint and the same limit slip s_f. *Ad hoc* experiments would be necessary for a precise evaluation of q_0, but this choice represents a reasonable compromise. In any case, the results that follow remain valid, at the qualitative level, if one considered other values of q_0 rather than this.

For the experiments of [12], I suggest the values $\tau_f = 7.71$ MPa and $s_f = 0.15$ mm, so that $\tau_c = 3.85$ MPa (Table 5.1). Figure 5.13 shows the ratio $G^*_{\omega,n}\tau_c^2/\Gamma$ introduced in (5.35), as a function of the inclination angle ω of the crack for different values of the quantum length a^*. The fracture energy Γ for the substrate has been evaluated through the empirical model by Bažant and Becq-Giraudon

Table 5.1: Mechanical properties of materials used in experimental campaigns and parameters of the interface law.

Test	**Concrete**								**FRP**			**Interface Law**	
	E_p [MPa]	f_t [MPa]	f'_c [MPa]	$d_{a,\max}$ [mm]	W/C -	a_0 -	t_p [mm]	b_p [mm]	E_s [MPa]	t_s [mm]	b_s [mm]	τ_f [MPa]	s_f [mm]
Biolzi *et al.* [34]	30500	3.06	32.59	25	0.7	1.00	120	150	170000	1.4	25.4	7.78	0.26
Carrara *et al.* [12]	28700	3.2	32.4	16	0.5	1.44	90	150	168500	1.3	50	7.71	0.15

[83], which takes into account the effects of the shape and the surface texture of the aggregates based upon a large database of test results. In particular, one can consider the expression for mode I fracture energy of concrete (the dominant fracture mode), which reads

$$\Gamma = 2.5\, a_0 \left(\frac{f'_c}{0.051}\right)^{0.46} \left(1 + \frac{d_{a,\max}}{11.27}\right)^{0.22} \left(\frac{W}{C}\right)^{-0.30} = \begin{cases} 0.077\,\mathrm{N\,mm^{-1}}, & \text{for [34]},\\ 0.11\,\mathrm{N\,mm^{-1}}, & \text{for [12]}, \end{cases} \tag{5.36}$$

where a_0 is the parameter that takes into account the shape of the aggregate (1 for rounded aggregates; 1.44 for crushed and sharp aggregates), $f'_c = f_c + 8[MPa]$ is the cylinder compressive strength of concrete [65], $d_{a,\max}$ is the maximum aggregate size in the mix and W/C is the water/cement ratio by weight of the mix. Assumed data are those of Table 5.1.

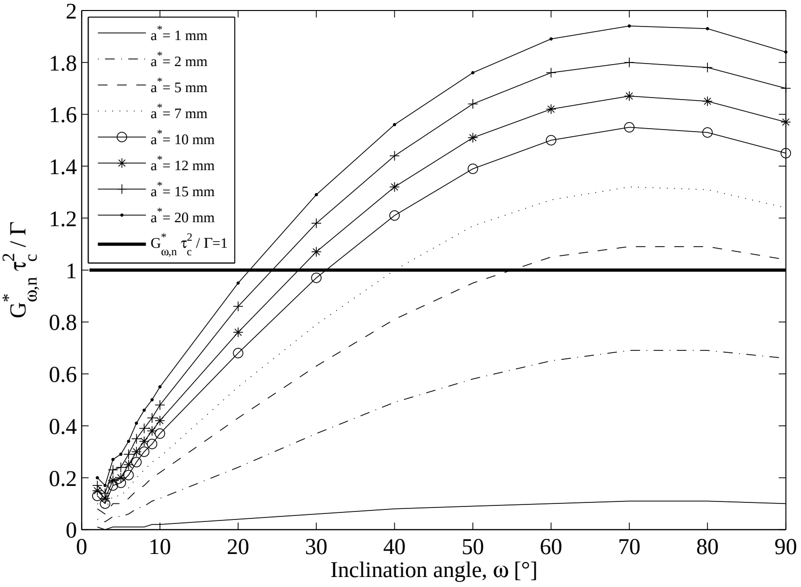

Figure 5.13: Normalized strain energy release as a function of the inclination angle ω for different values of the crack quantum length a^* (mechanical parameters of [12], bond length $l = 30$ mm, $q_0 = \tau_c$).

The value $G^*_{\omega,n}\,\tau_c^2/\Gamma = 1$ defines the limit case that separates the two different damage mechanisms as *per* (5.35) of section 5.4. From the graph of Figure 5.13, it is then possible to evaluate, for a fixed quantum length a^* of crack-propagation, defined in (5.31), the limit angle ω which marks the transition from one of the damage mechanism to the other. For example, the angle $\omega \simeq 31°$ corresponds to a quantum length $a^* = 10$ mm, whereas the angle $\omega \simeq 21°$ is associated with $a^* = 20$ mm.

For the sake of comparison, I report in Figure 5.14 the counterpart of the graphs of Figure 5.13 for the case $q_0 = \tau_f$, i.e., when the peak shear stress, rather than the average value, is considered. For this case, $\omega \simeq 33^\circ$ for $a^* = 10$ mm, and $\omega \simeq 26^\circ$ when $a^* = 20$ mm. In general, the higher the value of the critic shear stress q_0, the higher are the inclination angles. It is reasonable to assume that the real situation should correspond to an intermediate value between $q_0 = \tau_c$ and $q_0 = \tau_f$. In any case, the qualitative aspects of the problem remain the same.

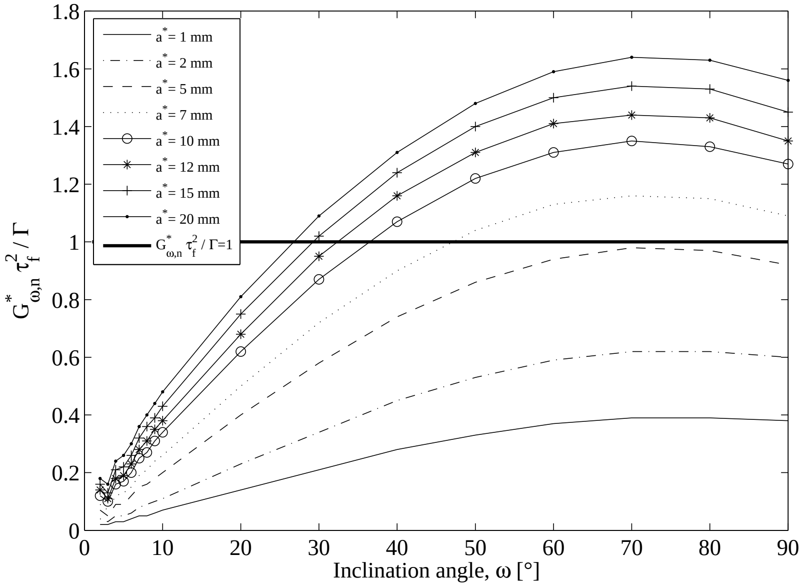

Figure 5.14: Normalized strain energy release as a function of the inclination angle ω for different values of the crack quantum length a^* (same parameters of Figure 5.13, except $q_0 = \tau_f$ and $l = 25$ mm).

Figure 5.15 reports the counterpart of the graphs of Figure 5.14 for the tests by Biolzi *et al.* [34]. From Table 5.1, one has $\tau_f = 7.78$ MPa and $s_f = 0.26$ mm. Consequently, for this case, $\omega \simeq 17^\circ$ for $a^* = 10$ mm, and $\omega \simeq 10^\circ$ when $a^* = 20$ mm.

It is important to remark that such a result is strongly based upon the assumption of “quantized fracture mechanics” [69]. Relaxation of this hypothesis, i.e., assuming that the crack propagation is smooth and the increment of crack length is whatever small, does not allow to interpret the phenomenon. In fact, notice that as $a^* \to 0$, the corresponding graphs tend to flatten so that in general, for whatever value of ω and q_0, one would find $G^*_{\omega,n} q_0^2/\Gamma < 1$. In other words, interface debonding would always be the preferred mechanism. Therefore, the definition of the “fracture quantum” has a central role for the description of the propagation process.

For the case of concrete, the crack quantum length a^* is certainly associated with the average size of the aggregate, correlated with the characteristic length-scale of

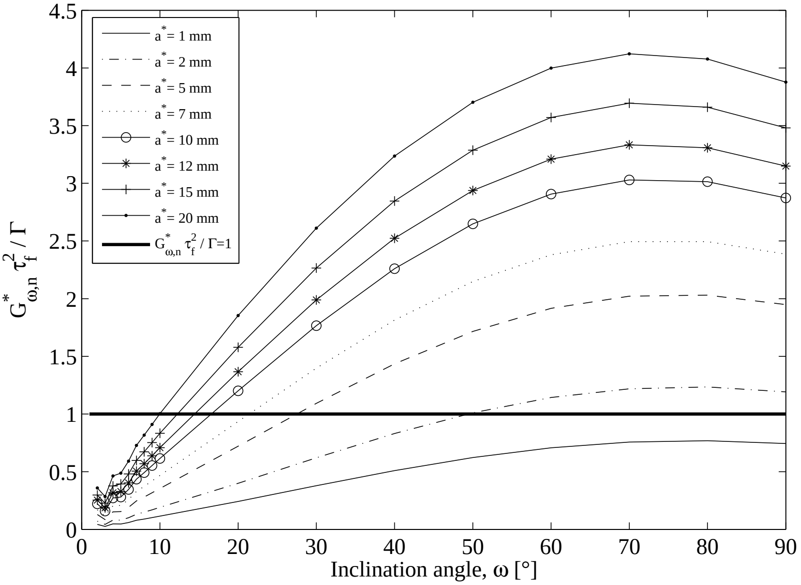

Figure 5.15: Normalized strain energy release as a function of the inclination angle ω for different values of the crack quantum length a^* (Mechanical parameters of [34], $l = 50$ mm, $q_0 = \tau_f$).

the material. For the tests of [12], since such average size is in the range $10 \div 15$ mm, one can conveniently consider values of the same order for a^*. Figure 5.13 shows that, with this choice, the critical angle ω varies in the interval $24° \div 31°$. From the pictures recorded in [12], already presented in Figure 5.1, it is evident the formation of wedge-shaped concrete bulbs at the end of the broken specimens. Such wedges are defined by angles comprised in the interval $18° \div 33°$, which agree very well with the conclusions of the present theory.
In the same way, considering the experimental data of [34], since the average size of the aggregate is in the range $10 \div 20$ mm, one can conveniently consider such values for a^*. Therefore, from the graph of Figure 5.15, it is evident that the critical angle ω varies in the interval $10° \div 17°$. Measurements of the bulbs detached in the experiments [34] show that the critical angle ω varies in the range $9° \div 18°$, which squares very well with the prediction of the analytical model.

5.6 Discussion

The pull-out of a FRP stringer adherent to a quasi-brittle substrate such as concrete is characterized by debonding starting from the loaded end and progressing towards the free extremity of the stringer [76, 77]. A peculiar phenomenon occurs just prior to rupture, when the surviving bond length is of the order of $30 \div 50$ mm. An inclined crack forms at the free end of the stiffener and extends into the substrate, and in doing so it defines a wedge-shaped portion of the substrate that eventually separates as a characteristic bulb that remains attached to the stiffener.

To my knowledge, this type of failure has not been exhaustively discussed in the technical literature. This is the motivation for the present study, where a simplified model problem has been presented. The model is built upon four hypotheses: *i*) the stiffener bending stiffness is negligible, so that only tangential traction develops between the stiffener and the substrate; *ii*) when the inclined crack initiates, the surviving bond length is so small that the stiffener-substrate relative slip, and consequently the tangential contact stress, can be considered uniform; *iii*) the eventual formation of the inclined crack isolates a wedge in the substrate immediately underneath the stiffener that produces a localized release of the stiffener itself, here supposed to be complete (contact stresses directly applied on this portion are neglected); *iv*) the crack propagation occurs through crack increments (*quanta*) of small but finite length.

Under the assumption of a linear elastic, homogeneous and isotropic semi-infinite substrate in generalized plane stress, the distributed dislocation approach has been used to determine the opening of the inclined crack, the stress intensity factors, and the energy release rate. The problem is reduced to the solution of a singular integral equation, representing the condition of zero traction along the crack surfaces, which has been solved numerically by using the method proposed by Erdogan and Gupta [58].

It is concluded that two damage mechanisms are in competition: debonding along the stiffener-substrate interface or cracking at the free extremity of the stiffener along an inclined path. In general, debonding can occur when the shear contact stress is greater than the maximum allowable strength of the interface. On the other hand, the inclined crack opens when the strain energy release associated with its quantized propagation is not lower than the corresponding fracture energy of the substrate itself. Which of the two scenarios is realized for prescribed values of the crack quantum (including the angle of extension of the subsurface crack that do form) is identified using the criterion proposed in [82].

The hypothesis of "quantized fracture mechanics" is crucial for the present model, because the inclination of the crack that wins the competition with interface debonding depends upon the length of the crack "quantum". This quantity is associated with the characteristic length-scale of the material, which for a natural conglomerate, like concrete, is of the same order of the average size of the aggregate.

Assuming consistent material parameters, the predictions of the proposed model have been compared with experimental results of FRP-to-concrete pull-out tests that are available in the literature. The concrete bulbs that remain attached to the FRP strips have angles in very good agreement with the proposed analytical model. The results of this study provide valuable insights that can in the future be assessed further using computational simulations under less restrictive assumptions.

CHAPTER 6

CONCLUSIONS

6.1 Review

Fiber Reinforced Polymer (FRP) strips are widely employed to strengthen concrete or masonry structural elements. Although an extensive research has been carried out during the past years, a review of the state-of-the-art in the applications of FRP to concrete structures has evidenced that further investigations need to be done to clarify some aspects of the debonding process. Information on how interfacial properties affect the debonding mechanism and strengthening capacity is not completely understood and, in some cases, the modeling techniques proposed by different authors in past investigations have been done without a sound theoretical basis. Furthermore, a review of the technical literature has evidenced a lack in the modeling of the characteristic phenomenon of the wedge-shaped fracturing of concrete in the final stage of debonding, i.e., when complete separation of the stiffener from the support occurs. As a matter of fact, there is no unanimous agreement on the causes of this particular aspect.

Motivated by the necessity to furnish a throughout characterization of the debonding process with sound theoretical basis, an analytical model has been developed in order to assess the interfacial debonding failure of the FRP-to-concrete bonded joint.

Due to the popularity of this strengthening technique, many different experimental set-ups have been proposed, but all the experiments evidence that the main failure mode is the cracking of concrete under shear, generally occurring a few millimeters below the adhesive interface. For this reason, among the various experimental set-ups, the pull-out test has been considered to analyze the debonding process. Despite the variety of the reinforcing materials, of the strengths of the substrates and of the geometry of the stiffeners, there is a general agreement on many aspects of the ultimate performance of the bonded joint. One of these is certainly the *Effective*-Bond-Length (EBL) of the stiffener, defined as the bond length beyond which no further increase of pull-out load can be achieved. Accordingly, the latter is therefore another important parameter of the failure process, i.e., the *ultimate load* or *bond strength* of the bonded joint.

Considering the main characteristics of the pull-out test, the model problem here considered is therefore the debonding in *mode II* of a straight elastic stiffener, of prescribed length, from an elastic substrate in generalized plane stress. Since its thickness is in general very small, the FRP strip can be modeled as a membrane with negligible bending stiffness. Hence, the stiffener is not able to sustain transverse loads during small deformations and this results in the absence of peeling stresses at the interface.

In the model of Chapter 3, the role of the substrate elasticity has been emphasized. Compatibility conditions for the axial strains between stiffener and substrate permitted to obtain an integral equation in terms of the shear stresses. The solution obtained exploiting the properties of Chebyshev polynomials has then be used to establish an energetic balance *à la* Griffith, which also permits to determine the critical load. Fracture occurs as long as the strain energy release rate associated with the propagation of an infinitesimal crack length is higher than the interfacial fracture energy. In order to determine the energy release rate, a generalization of the *Crack Closure Integral Method* developed by Irwin [57] has been written. Results of the calculations show that the strain energy release rate strongly depends upon the elasticity of the substrate, tending to the limit value for a rigid substrate calculated by Taljsten [60] when the Young modulus of the substrate, E_p, tends to ∞. The energetic balance allows to evaluate the maximum transmissible load and the progression of the debonding phenomenon as well as the onset of a snap-back phase, remarking the important role played by the elasticity of the substrate, which is usually neglected in the practice. One of the major drawbacks of this model is that the diffusion of load from the stringer to the substrate only depends upon the elasticity of the material: stress singularities occur at both ends of the adherent interface, so that it is difficult to give a sound definition of the effective anchorage length.

To solve this inconsistency, Chapter 4 introduces two cohesive zones at both ends of the stiffener, where slip can occur, in order to annihilate the singularities predicted by the elasticity theory. Following the approach originally proposed by Barenblatt [63], the length of these cohesive zones for a fixed load is evaluated by imposing that the stress intensity factors at the extremities of the perfectly bonded zone are null. Two model have been developed: the SCZ (Single Cohesive Zone) model, where the cohesive zone is introduced at loaded end of the stiffener and the DCZ (Double Cohesive Zone) model, that accounts also for a second cohesive zone at the free end of the stiffener. To illustrate, one may consider that in the SCZ model[11] material separation is supposed to start when the relative slip at the loaded end exceeds a certain threshold. If the stiffener is sufficiently long, there is maximal reachable length of the cohesive zone: in a pull out test, the cohesive portion simply translates along the stiffener as debonding proceeds, maintaining its length unchanged, while the load remains practically constant, confirming that only part of the bond is active. In other words, the bond strength does not increase with an increase of the bond length, even if increasing the bond length can improve the ductility of the bonded joint. A strain softening phase, usually associated with snap-back, is entered when the cohesive zone reaches the free end of the stiffener. As a consequence, this model provides a physical definition of the *effective bond length*, since it is associated with the maximal length of the cohesive zone reached in sufficiently long stiffeners. Assuming a very simple, step-wise, shear-stress vs. slip constitutive law for the interface, the model is able to interpret the debonding process step-by-step, evidencing different-in-type responses when the bond length is higher or lower than the effective bond length.

---

[11] The behavior is exactly the same in the DCZ model.

The potentialities of the two approaches (SCZ and DCZ) have been discussed and compared with the completely adherent model of Chapter 3, referred to as No Cohesive Zone (NCZ) model. In the NCZ model, the interfacial shear stress shows an extremely rapid decrease from the maximum concentration near the loaded end. The SCZ approach, just assuming a very simple step-wise interface law, predicts the formation of a cohesive zone that produces a more gradual decay of the contact stress in agreement with experimental results. The DCZ model prescribes two cohesive zones at the edges of the reinforcement, but it has been shown that the zone at the free end does not play a significant role. The stress distribution practically coincides with that of the SCZ model, apart from a very small neighborhood of the free end where the singularity is present.

The *ultimate load* obtained through the three models matches very well not only with experimental results, but also with the relevant formulas proposed in technical standards [1]. For what the effective bond length is concerned, the NCZ is not accurate, because the shear stress at the interface decays too rapidly. The SCZ and DCZ models both give predictions in good agreement with relevant tests recorded in the literature, because their shear stress distribution is almost the same except in a small neighborhood of the free-end. On the other hand, it must be observed that the formulas suggested by standards [1] give excessively overestimated values. To this respect, the SCZ and DCZ approaches seem to be an improvement of what proposed so far. Moreover, the SCZ model, which considers only one cohesive zone, is able to predict correct values of the critical pull-out load as well as of the EBL, identical to those provided by the DCZ model through more complicated calculations. Consequently, in an engineering approach, the SCZ formulation appears to be the best compromise.

Chapter 5 investigates the last stage of debonding, when a wedge-shaped portion of material detaches from the support. The opening of an inclined crack, which isolates the bulb, usually occurs when the remaining bond length is very small, generally of the order of the width of the FRP lamina. Under reasonable hypothesis, the solution of the elastic problem has been found by means of the distributed dislocation technique and the propagation of crack at the end of the stiffener has been obtained superimposing two schemes: *i*) the effect of the distribution of tangential stresses on the surface of the half plane and *ii*) the effect of distributed edge dislocations along the crack reference configuration. Conditions that the crack lips are stress free furnishes an integral equation that is solved in series of Chebyshev's polynomials.

In the model, two competing mechanisms of failure may occur: *a*) failure of the adhesive joint, which progresses at the stiffener-substrate interface when the corresponding shear stress is greater than the strength of the interface itself; *b*) inclined cracking, which can develop in the substrate when the strain energy release associated with its propagation is greater than the corresponding fracture energy of the material. From the competition of the two mechanisms one can evaluate when the inclined crack starts to form and the characteristic angle of the wedge-shaped bulb.

The proposed model problem represents a simple and intuitive tool to investigate this peculiar phenomenon and provides results that are in very good qualitative agreement with experiments, drawn from the technical literature.

6.2 Contributions

The main purpose of this work has been the modeling of the various and different-in-type mechanisms that characterize the failure process of FRP stiffeners bonded to quasi-brittle substrates under pull-out loads. What I repute to be novel contributions of this research to the state-of-the-art can be summarized as follows.

- The contact problem of the elastic stiffener to the substrate has been analyzed taking into account the deformation of the substrate itself, here considered linear elastic. In the traditional approaches the substrate is supposed rigid and the essence of the phenomenon is condensed in a particular stress vs. slip constitutive law for the cohesive interface. But I have shown that this assumption has major drawbacks.

- The *Crack Closure Integral Method* developed by Irwin has been extended to the case of a propagating interface crack between the stiffener and the substrate, to evaluate the energy release rate as a function of the corresponding stress intensity factor. This generalization, although attempted by other authors, does not seem to have been correctly posed in previous contributions.

- I have shown that a simple energetic balance *à la* Griffith is effective in predicting the *strength* of the bond under the hypothesis of perfect adhesion (no slip) between stiffener and substrate. However, the presence of stress singularities in the corresponding linear elastic solutions does not allow to give a sound definition and interpretation of the *effective bond length*.

- To solve the aforementioned inconsistency, I have assumed the presence of a cohesive zone in the bond. With a very simple step-wise constitutive law for the interface, but considering the elastic deformation of the substrate, I have shown that it is possible to annihilate the stress singularities. More important, slip can occur in just a portion of the bonded joint, while the other part remains perfectly bonded. The load applied to the stiffener is in practice balanced by the cohesive portion of the joint, whose maximum length can therefore be considered the effective bond length. In this way, a physically consistent definition of this important parameter has been provided.

- In the elastic perfect-contact problem, the are two stress singularities, one at loaded end and the other at the free extremity of the stiffener. The singularity that plays a major role is the one at the loaded end, because the stress in a very small neighborhood of that singular point equilibrates, by far, most of the pull-out load. The second singularity, at the free extremity, gives almost a negligible contribution to this respect. Therefore, I have concluded that it is sufficient to introduce one cohesive zone at the loaded end to obtain consistent results, thus avoiding the major complication of treating two cohesive zones.

- The characteristic *wedge-shaped fracturing* of the substrate in the final stages of the failure process has been modeled in detail. This aspect does not seem to have been exhaustively treated in the technical literature. A basic hypothesis for the proposed theory is the “quantized” propagation of fracture, i.e., crack increments can only be of finite length (*quantum*).
- The proposed models can cover the whole process of failure of the bonded joint under a pull out load. The results obtained from the models are in very good agreement with the experimental evidence.

6.3 Further developments and future research

This study is analytical. The careful hypotheses that were necessary to simplify the problem to allow its analytical solution have permitted, at the same time, to recognize and understand the fundamental aspects of the phenomenon. This is therefore a preliminary study, propaedeutic to do a more complex numerical modeling. For example, the cohesive models have been derived under the hypothesis of a step-wise constitutive law for the interface. Despite its simplicity, the formulation is able to capture the essence of the debonding phenomenon before the snap-back phase occurs, i.e., the maximum strength and the extension of the effective bond length. However, a numerical implementation that uses the trilinear interface law, the one commonly accepted in the scientific community, could improve the predictions obtainable through the model, to better interpret in particular the snapback phase in the load-displacement curve. Moreover, the characteristic wedge-shaped fracturing of the substrate in the latest stage of the failure process has been obtained under the major hypothesis of quantized propagation of cracks. I believe that such an assumption cannot be relaxed, and therefore should be accurately implemented in any numerical modeling. Further work could account for the possibility of a cohesive zone at the interface. Of course, a more refined experimental investigation is needed to confirm the soundness of the proposed approaches. The essential aspects of the debonding phenomenon have been conjectured in the analytical models here presented. Ad hoc designed experimental activity will clarify the correctness of the assumptions made.

APPENDIX **A**

CHEBYSHEV POLYNOMIALS

The Chebyshev polynomials are usually defined introducing the variables

$$t = \cos(\varphi)\,, \quad \varphi = \arccos(t)\,. \tag{A.1}$$

The polynomials of the first kind take the form [84]

$$T_s(t) = \cos(s\varphi(t)) = \cos(s \arccos(t))\,, \tag{A.2}$$

while the polynomials of the second kind are defined as

$$U_s(t) = \frac{\sin(s+1)\varphi(t)}{\sin(\varphi(t))}\,. \tag{A.3}$$

Both T_s and U_s form a sequence of orthogonal polynomials. The polynomials of the first kind are orthogonal with respect to the weight $1/\sqrt{1-t^2}$ on the interval $[-1,1]$, that is,

$$\int_{-1}^{1} \frac{T_s(t)T_m(t)}{\sqrt{1-t^2}}dt = \begin{cases} 0\,, & \text{for } m \neq s\,, \\ \frac{\pi}{2}\,, & \text{for } m = s \neq 0\,, \\ \pi\,, & \text{for } m = s = 0\,. \end{cases} \tag{A.4}$$

Similarly, the polynomials of the second kind are orthogonal with respect to the weight $\sqrt{1-t^2}$ on the interval $[-1,1]$, i.e.,

$$\int_{-1}^{1} U_s(t)U_m(t)\sqrt{1-t^2}dt = \begin{cases} 0\,, & \text{for } m \neq s\,, \\ \frac{\pi}{2}\,, & \text{for } m = s\,. \end{cases} \tag{A.5}$$

The following properties are useful:

$$\int_{-1}^{1} \frac{T_s(t)}{\sqrt{1-t^2}(t-t_0)} dt = \begin{cases} 0\,, & \text{for } s=0 \text{ and } |t_0|<1\,, \\ \pi U_{s-1}(t_0)\,, & \text{for } s>0 \text{ and } |t_0|<1\,, \\ -\pi \frac{(t_0 - \frac{|t_0|}{t_0}\sqrt{t_0^2-1})^s}{\frac{|t_0|}{t_0}\sqrt{t_0^2-1}}\,, & \text{for } s\geq 0 \text{ and } |t_0|>1\,. \end{cases} \tag{A.6}$$

$$\begin{aligned} &\int_{-1}^{1} U_{s-1}(t)\sqrt{1-t^2}\ln|t-t_0|dt \\ &= \begin{cases} -\frac{\pi}{2}(t_0^2+\ln 2), & \text{for } s=1 \text{ and } |t_0|<1, \\ \frac{\pi}{2}\left[\frac{T_{s+1}(t_0)}{s+1} - \frac{T_{s-1}(t_0)}{s-1}\right], & \text{for } s>1 \text{ and } |t_0|<1, \\ \frac{\pi}{4}\left[\left(\sqrt{t_0^2}-\sqrt{t_0^2-1}\right)^2 + 2\ln\left|\frac{t_0+\frac{|t_0|}{t_0}\sqrt{t_0^2-1}}{2}\right|\right], & \text{for } s=1 \text{ and } |t_0|>1, \\ \frac{\pi}{2}\left(-\frac{|t_0|}{t_0}\right)^{s-1}\left[\frac{\left(\sqrt{t_0^2-1}-\sqrt{t_0^2}\right)^{s+1}}{s+1} - \frac{\left(\sqrt{t_0^2-1}-\sqrt{t_0^2}\right)^{s-1}}{s-1}\right], & \text{for } s>1 \text{ and } |t_0|>1. \end{cases} \end{aligned} \tag{A.7}$$

Another property of the Chebyshev polynomials is that, in the interval $-1 \leq t \leq 1$, they attain the maximum and minimum values at the endpoints, given by

$$\begin{cases} T_s(1) = 1\,, \\ T_s(-1) = (-1)^s\,, \\ U_s(1) = s+1\,, \\ U_s(-1) = (s+1)(-1)^s\,. \end{cases} \tag{A.8}$$

These relationships are of help while estimating qualitative properties of the solution.

APPENDIX B

GREEN'S FUNCTIONS

$$K_1(r,\rho) = -\frac{2\rho i \sin\omega}{(re^{i\omega}-\rho e^{-i\omega})^2} - \frac{1-e^{-2i\omega}}{(re^{-i\omega}-\rho e^{i\omega})} + \frac{2rie^{-2i\omega}\sin\omega}{(re^{-i\omega}-\rho e^{i\omega})^2} \tag{B.1}$$

$$\begin{aligned} K_2(r,\rho) = &-\frac{1}{(re^{i\omega}-\rho e^{-i\omega})} + \frac{2\rho i(1-e^{-2i\omega})\sin\omega}{(re^{-i\omega}-\rho e^{i\omega})^2} \\ &- \frac{e^{-2i\omega}}{(re^{-i\omega}-\rho e^{i\omega})} + \frac{8r\rho e^{-2i\omega}\sin^2\omega}{(re^{-i\omega}-\rho e^{i\omega})^3} \end{aligned} \tag{B.2}$$

$$\begin{aligned} K_3(r,\rho) = &-\frac{1}{re^{-i\vartheta}-\rho e^{i\omega}} + \frac{1}{re^{-i\vartheta}-\rho e^{-i\omega}} - \frac{1}{re^{i\vartheta}-\rho e^{-i\omega}} - \frac{e^{2i\vartheta}}{re^{i\vartheta}-\rho e^{i\omega}} \\ &+ \frac{(1+e^{2i\vartheta})(re^{i\vartheta}-\rho e^{i\omega})}{\left(re^{i\vartheta}-\rho e^{-i\omega}\right)^2} + \frac{4rie^{2i\vartheta}\sin\vartheta}{\left(re^{i\vartheta}-\rho e^{-i\omega}\right)^2} - \frac{4rie^{2i\vartheta}\sin\vartheta(re^{i\vartheta}-\rho e^{i\omega})}{\left(re^{i\vartheta}-\rho e^{-i\omega}\right)^3} \end{aligned} \tag{B.3}$$

$$\begin{aligned} K_4(r,\rho) = &-\frac{1}{re^{-i\vartheta}-\rho e^{i\omega}} - \frac{(1+e^{2i\vartheta})}{re^{i\vartheta}-\rho e^{-i\omega}} + \frac{1}{re^{i\vartheta}-\rho e^{i\omega}} + \frac{re^{-i\vartheta}-\rho e^{-i\omega}}{re^{-i\vartheta}-\rho e^{i\omega}} \\ &+ \frac{2rie^{2i\vartheta}\sin\omega}{\left(re^{i\vartheta}-\rho e^{-i\omega}\right)^2} + \frac{e^{2i\vartheta}(re^{-i\vartheta}-\rho e^{-i\omega})}{\left(re^{i\vartheta}-\rho e^{i\omega}\right)^2} \end{aligned} \tag{B.4}$$

$$H_1(r,\xi) = \frac{1}{\xi - re^{i\omega}} - \frac{e^{-2i\omega}}{\xi - re^{-i\omega}} \tag{B.5}$$

$$H_2(r,\xi) = \frac{(1-e^{-2i\omega})}{\xi - re^{-i\omega}} + \frac{2rie^{-2i\omega}\sin\omega}{(\xi - re^{-i\omega})^2} \tag{B.6}$$

$$H_3(r,\xi) = \frac{1}{\xi - re^{-i\vartheta}} + \frac{(1+e^{2i\vartheta})}{\xi - re^{-i\vartheta}} + \frac{2rie^{2i\vartheta}\sin\vartheta}{\left(\xi - re^{i\vartheta}\right)^2} \tag{B.7}$$

$$\begin{aligned} K_1(s,t) = &-\frac{2(t+1)i\sin\omega}{((s+1)e^{i\omega}-(t+1)e^{-i\omega})^2} - \frac{1-e^{-2i\omega}}{((s+1)e^{-i\omega}-(t+1)e^{i\omega})} \\ &+ \frac{2(s+1)ie^{-2i\omega}\sin\omega}{((s+1)e^{-i\omega}-(t+1)e^{i\omega})^2} \end{aligned} \tag{B.8}$$

$$\begin{aligned} K_2(s,t) = &-\frac{1}{((s+1)e^{i\omega}-(t+1)e^{-i\omega})} + \frac{2(t+1)i(1-e^{-2i\omega})\sin\omega}{((s+1)e^{-i\omega}-(t+1)e^{i\omega})^2} \\ &- \frac{e^{-2i\omega}}{((s+1)e^{-i\omega}-(t+1)e^{i\omega})} + \frac{8(s+1)(t+1)e^{-2i\omega}\sin^2\omega}{((s+1)e^{-i\omega}-(t+1)e^{i\omega})^3} \end{aligned} \tag{B.9}$$

$$H_1(s,\zeta) = \frac{1}{(\zeta+1)-(s+1)e^{i\omega}} - \frac{e^{-2i\omega}}{(\zeta+1)-(s+1)e^{-i\omega}} \tag{B.10}$$

$$H_2(s,\zeta) = \frac{(1-e^{-2i\omega})}{(\zeta+1)-(s+1)e^{-i\omega}} + \frac{2(s+1)ie^{-2i\omega}\sin\omega}{((\zeta+1)-(s+1)e^{-i\omega})^2} \tag{B.11}$$

APPENDIX **C**

STRESS AND STRAIN ON THE WEDGE-SHAPED-CRACKED HALF-PLANE, LOADED FOR THE WHOLE BOND LENGTH

Consider the wedge-shaped cracked elastic half-plane of Figure 5.3(a), and suppose that the contact stresses with the stiffener are tangential forces per unit area q, uniformly distributed along the *whole* bonded surface. In order to evaluate the state of stress σ_{rr} along such surface, consider the relation

$$\sigma_{rr} + i\sigma_{r\vartheta} = \Phi(z) + (1 + e^{2i\vartheta})\overline{\Phi(z)} - (z - \bar{z})e^{2i\vartheta}\overline{\Phi'(z)} + e^{2i\vartheta}\Phi(\bar{z}). \tag{C.1}$$

With the same procedure of section 5.2.2, the stress is due to the superposition of the two problems of Figure 5.7.

Consider first the half-plane with the inclined crack (Figure 5.8). The stress along the radial line $z = re^{-i\vartheta}$ due to a distributed dislocation acting along the crack of length a at $z_0 = \rho e^{-i\omega}$, $0 \le \rho \le a$, are given by setting $\Phi(z) = \Phi_{dw}(z) + \Phi_{dc}(z)$, as *per* (5.4) and (5.6), in (C.1), and reads

$$(\sigma_{rr} + i\sigma_{r\vartheta})^d = \int_0^a B(\rho)K_3(r,\rho)d\rho + \int_0^a \overline{B(\rho)}K_4(r,\rho)d\rho, \tag{C.2}$$

where $K_3(r,\rho)$ and $K_4(r,\rho)$ are given in Appendix B.

The case of a half-space with tangential stresses applied over the length l of its boundary can be solved with the same procedure of section 5.2.2 substituting the expression for the complex potentials (5.10) into equation (C.1), where in this case the domain of integration is the interval $[0, l]$. The stresses along the line $z = re^{-i\vartheta}$ due to the presence of a distribution of constant shear stress q along the surface $z_0 = \overline{z_0} = \xi$ are given by

$$(\sigma_{rr} + i\sigma_{r\vartheta})^q = \frac{q}{2\pi}\int_0^l H_3(r,\xi)d\xi, \tag{C.3}$$

where $H_3(r,\xi)$ is given in Appendix B.
Therefore, the state of stress due to the superposed effects is given by

$$\sigma_{rr}+i\sigma_{r\vartheta}=\int_0^a B(\rho)K_3(r,\rho)d\rho+\int_0^a \overline{B(\rho)}K_4(r,\rho)d\rho+\frac{q}{2\pi}\int_0^l H_3(r,\xi)d\xi. \quad \text{(C.4)}$$

In the special case $\vartheta=0$ (surface of the half-plane) the integral (C.4) becomes

$$(\sigma_{rr}+i\sigma_{r\vartheta})|_{\vartheta=0}=\int_0^a B(\rho)K_3^*(r,\rho)d\rho+\int_0^a \overline{B(\rho)}K_4^*(r,\rho)d\rho+\frac{q}{2\pi}\int_0^l \left[\frac{4}{\xi-r}\right]d\xi, \quad \text{(C.5)}$$

where

$$\begin{aligned} K_3^*(r,\rho)&=\left[2\left(-\frac{1}{r-\rho e^{i\omega}}+\frac{r-\rho e^{i\omega}}{(r-\rho e^{-i\omega})^2}\right)\right],\\ K_4^*(r,\rho)&=\left[2\left(-\frac{1}{r-\rho e^{-i\omega}}+\frac{r-\rho e^{-i\omega}}{(r-\rho e^{i\omega})^2}\right)\right],\end{aligned} \quad \text{(C.6)}$$

and the last integral is intended as a Cauchy principal value.
The integral (C.5) can be solved using the methods provided by Erdogan and Gupta in [58] and reported in section 5.3.1. By using relations (5.17) and (5.18) and the property of Chebyshev polynomials, one obtains the integral (C.4) in the discretized form

$$\begin{aligned}(\sigma_{rr}+i\sigma_{r\vartheta})|_{\vartheta=0}=\frac{\pi}{n}\sum_{k=1}^{n}B_{\text{reg}}(t_k)K_3^*(s_j,t_k)+\frac{\pi}{n}\sum_{k=1}^{n}\overline{B_{\text{reg}}(t_k)}\;K_4^*(s_j,t_k)+\\ \frac{q}{2\pi}\left[4\left(i\pi+\ln\left|\frac{1-s_j}{1+s_j}\right|\right)\right],\quad j=1,...,n-1,\end{aligned} \quad \text{(C.7)}$$

where $t_k=\cos\varphi_k$, $s_j=\cos\vartheta_j$ and the integration and collocation points are given by equation (5.20). The following relation holds

$$B_{\text{reg}}=\frac{q}{2\pi}\widehat{B}_{\text{reg}},$$

where $\widehat{B}_{\text{reg}}$ is given by the solution of the integral equation (5.19).
For the sake of comparison, one may focus on the wedge-shaped portion of the substrate isolated by the inclined crack, and consider for this, as an approximation, the solution given by Michell [79] for an *infinite* wedge loaded by shear stresses on one of its edges, as represented in Figure 5.5. Recall that the stress components are given by

$$\sigma_{rr} = -2A_1 \cos 2\vartheta + 2A_2 - 2A_3 \sin 2\vartheta + 2A_4\vartheta, \tag{C.8a}$$

$$\sigma_{r\vartheta} = 2A_1 \sin 2\vartheta - 2A_3 \cos 2\vartheta - A_4, \tag{C.8b}$$

$$\sigma_{\vartheta\vartheta} = 2A_1 \cos 2\vartheta + 2A_2 + 2A_3 \sin 2\vartheta + 2A_4\vartheta, \tag{C.8c}$$

where the four constants can be obtained through the boundary conditions

$$\begin{cases} \sigma_{r\vartheta} = q, \quad \sigma_{\vartheta\vartheta} = 0, \quad \text{for } \vartheta = 0\,, \\ \sigma_{r\vartheta} = 0, \quad \sigma_{\vartheta\vartheta} = 0, \quad \text{for } \vartheta = \omega\,. \end{cases} \tag{C.9}$$

The stress components are therefore

$$\sigma_{rr} = -\frac{q}{2}\frac{[\cos(2\vartheta - \omega) + \cos\omega - 2\omega\cos\vartheta\cos(\vartheta - 2\omega)\csc\omega - 2\vartheta\sin\omega]}{\omega\cos\omega - \sin\omega}, \tag{C.10a}$$

$$\sigma_{r\vartheta} = -q\frac{[-\cos\vartheta + \omega\cos\vartheta\cot\omega + \omega\sin\vartheta]\sin(\vartheta - \omega)}{\omega\cos\omega - \sin\omega}, \tag{C.10b}$$

$$\sigma_{\vartheta\vartheta} = \frac{q}{2}\frac{[\cos(2\vartheta - \omega) - \cos\omega - 2\omega\sin\vartheta\sin(\vartheta - 2\omega)\csc\omega + 2\vartheta\sin\omega]}{\omega\cos\omega - \sin\omega}. \tag{C.10c}$$

In the case $\vartheta = 0$, one obtains

$$\sigma_{rr} = \frac{q}{2}\frac{\csc\omega\,(2\omega\cos 2\omega - \sin 2\omega)}{\omega\cos\omega - \sin\omega}, \tag{C.11a}$$

$$\sigma_{r\vartheta} = q, \tag{C.11b}$$

$$\sigma_{\vartheta\vartheta} = 0. \tag{C.11c}$$

Finally, the strain components are given, by Hooke's law, in the form

$$\varepsilon_{rr} = \frac{1}{E}(\sigma_{rr} - \nu\sigma_{\vartheta\vartheta}), \tag{C.12a}$$

$$\varepsilon_{\vartheta\vartheta} = \frac{1}{E}(\sigma_{\vartheta\vartheta} - \nu\sigma_{rr}), \tag{C.12b}$$

$$\varepsilon_{r\vartheta} = \frac{2(1+\nu)}{E}\sigma_{r\vartheta}. \tag{C.12c}$$

Remarkably, the simple Michell's solution, and the elastic solution for the cracked half plane, coincide on the wedge-shaped cracked portion, as represented in the graph of Figure 5.4.

REFERENCES

1. CNR-DT/200, Guide for the Design and Construction of Externally Bonded FRP Systems for Strengthening Existing Structures - Materials, RC and PC structures, masonry structures, National Research Council (CNR), 2004
2. Banthia N., Bisby L., Cheng R., Fallis G., Hutchinson R., Mufti A., Neale K.W., Newhook J., Soudki K., Wegner L., An Introduction to FRP Composites for Construction, ISIS Canada Educational Module, 2006
3. Banthia N., Bisby L., Britton R., Cheng R., Fallis G., Hutchinson R., Mufti A., Neale K.W., Newhook J., Soudki K., Wegner L., An Introduction to FRP Strengthening of Concrete Structures, ISIS Canada Educational Module, 2004
4. Piggott M., Load-bearing fibre composites, Pergamon international library of science, technology, engineering, and social studies, Pergamon Press, 1980
5. Chen J., Teng J., "Anchorage Strength Models for FRP and Steel Plates Bonded to Concrete", *Journal of Structural Engineering*, Vol. 127, no. 7, 2001, pp. 784–791
6. Maeda T., Asano Y., Sato Y., Ueda T., Kakuta Y., "A study on bond mechanism of carbon fiber sheet", *Proceedings of 3rd international symposium on non-metallic (FRP) reinforcement for concrete structures*, Vol. 1, 1997, pp. 279–285
7. Brosens K., Van Gemert D., "Anchoring stresses between concrete and carbon fibre reinforced laminates", *Proceedings of 3rd international symposium on non-metallic (FRP) reinforcement for concrete structures*, Vol. 1, 1997, pp. 271–278
8. Chajes M., Jr. W.W.F., Januszka T.F., Jr. T.A.T., "Bond and Force Transfer of Composite-Material Plates Bonded to Concrete", *ACI Structural Journal*, Vol. 93, no. 2, 1996, pp. 209–217
9. Taljsten B., "Defining anchor lengths of steel and CFRP plates bonded to concrete", *International Journal of Adhesion and Adhesives*, Vol. 17, no. 4,

1997, pp. 319 – 327

10. Bizindavyi L., Neale K., “Transfer Lengths and Bond Strengths for Composites Bonded to Concrete”, *Journal of Composites for Construction*, Vol. 3, no. 4, 1999, pp. 153–160
11. Mazzotti C., Savoia M., Ferracuti B., “An experimental study on delamination of FRP plates bonded to concrete”, *Construction and Building Materials*, Vol. 22, no. 7, 2008, pp. 1409 – 1421
12. Carrara P., Ferretti D., Freddi F., Rosati G., “Shear tests of carbon fiber plates bonded to concrete with control of snap-back”, *Engineering Fracture Mechanics*, Vol. 78, no. 15, 2011, pp. 2663 – 2678
13. Yao J., Teng J., Chen J., “Experimental study on FRP-to-concrete bonded joints”, *Composites Part B: Engineering*, Vol. 36, no. 2, 2005, pp. 99 – 113
14. De Lorenzis L., Miller B., Nanni A., “Bond of Fiber-Reinforced Polymer Laminates to Concrete”, *ACI Material Journal*, Vol. 98, 2001, pp. 256–264
15. Leung C.K., “Delamination failure in concrete beams retrofitted with a bonded plate”, *Journal of Materials in Civil Engineering*, Vol. 13, no. 2, 2001, pp. 106–113
16. Gemert D.V., “Force transfer in epoxy bonded steel/concrete joints”, *International Journal of Adhesion and Adhesives*, Vol. 1, no. 2, 1980, pp. 67 – 72
17. Suo Z., Hutchinson J., “Steady-state cracking in brittle substrates beneath adherent films”, *International Journal of Solids and Structures*, Vol. 25, no. 11, 1989, pp. 1337–1353
18. Dai J., Ueda T., Sato Y., “Development of the Nonlinear Bond Stress-Slip Model of Fiber Reinforced Plastics Sheet-Concrete Interfaces with a Simple Method”, *Journal of Composites for Construction*, Vol. 9, no. 1, 2005, pp. 52–62
19. Sayed-Ahmed E., Bakay R., Shrive N., “Bond strength of FRP laminates to concrete: state-of-the-art review”, *Electronic Journal of Structural Engineering*, Vol. 9, 2009, pp. 45–61
20. Holzenkämpfer P., Ingenieurmodelle des Verbunds geklebter Bewehrung für Betonbauteile, Dissertation, Ingenieurmodell für das Verbundsystem Stahlbeton + Klebelasche / Institut für Baustoffe, Massivbau und Brandschutz Braunschweig, IBMB, TU, 1994
21. Yuan H., Wu Z., Yoshizawa H., “Theoretical solutions on interfacial stress transfer of externally bonded steel/composite laminates.”, *Journal of Structural Mechanics and Earthquake Engineering*, Vol. 18, 2001, pp. 27–39
22. Neubauer U., Rostasy F., “Design aspects of concrete structures strengthened with externally bonded CFRP plates”, *Proceedings of the 7th International Conference on Structural Faults and Repair*, Vol. 2, 1997, pp. 109–118
23. Ali-Ahmad M., Subramaniam K., Ghosn M., “Experimental Investigation

and Fracture Analysis of Debonding between Concrete and FRP Sheets", *Journal of Engineering Mechanics*, Vol. 132, no. 9, 2006, pp. 914–923

24. Wu Z., Yuan H., Hiroyuki Y., Toshiyuki K., "Experimental/analytical study on interfacial fracture energy and fracture propagation along FRP-concrete interface", *ACI International SP-201-8*, Vol. 1, 2001, pp. 133–152
25. Yuan H., Teng J., Seracino R., Wu Z., Yao J., "Full-range behavior of FRP-to-Concrete bonded joints.", *Engineering Structures*, Vol. 26, 2004, pp. 553–565
26. Ferracuti B., Savoia M., Mazzotti C., "Interface law for FRP-concrete delamination", *Composite Structures*, Vol. 80, no. 4, 2007, pp. 523 – 531
27. Ueda T., Dai J., "Interface bond between FRP sheets and concrete substrates: properties, numerical modeling and roles in member behaviour", *Progress in Structural Engineering and Materials*, Vol. 7, no. 1, 2005, pp. 27–43
28. Lu X., Teng J., Ye L., Jiang J., "Bond-slip models for FRP sheets-plates bonded to concrete", *Engineering Structures*, Vol. 27, no. 6, 2005, pp. 920–937
29. Bazant Z., Planas J., Fracture and Size Effect in Concrete and Other Quasibrittle Materials, New directions in civil engineering, CRC Press, 1998
30. Neubauer U., Rostasy F., "Bond Failure of Concrete Fiber Reinforced Polymer Plates at Inclined Cracks-Experiments and Fracture Mechanics Model", *Proc of 4th international symposium on fiber reinforced polymer reinforcement for reinforced concrete structures, SP-188*, Vol. 188, 1999, pp. 369–382
31. Nakaba K., Kanakubo T., Furuta T., Yoshizawa H., "Bond behavior between fiber-reinforced polymer laminates and concrete", *ACI Structural Journal*, Vol. 98, no. 3, 2001, pp. 359–367
32. Savoia M., Ferracuti B., Mazzotti C., "Non linear bond-slip law for FRP-concrete interface", *Seven*, 2003, pp. 1–10
33. Monti G., Renzelli M., Luciani P., "FRP Adhesion in Uncracked and Cracked Concrete Zones", *Proc of 6th international symposium on FRP reinforcement for concrete structures*, 2003, pp. 183–192
34. Biolzi L., Ghittoni C., Fedele R., Rosati G., "Experimental and theoretical issues in FRP-concrete bonding", *Construction and Building Materials*, Vol. 41, 2013, pp. 182–190
35. Wu Z., Yuan H., Niu H., "Stress Transfer and Fracture Propagation in Different Kinds of Adhesive Joints", *Journal of Engineering Mechanics*, Vol. 128, no. 5, 2002, pp. 562–573
36. Chen G., Teng J., Chen J., "Process of debonding in RC beams shear-strengthened with FRP U-strips or side strips", *International Journal of Solids and Structures*, Vol. 49, no. 10, 2012, pp. 1266 – 1282
37. Carloni C., Subramaniam K.V., "Direct determination of cohesive stress

transfer during debonding of FRP from concrete", *Composite Structures*, Vol. 93, no. 1, 2010, pp. 184 – 192

38. Carloni C., Subramaniam K.V., Savoia M., Mazzotti C., "Experimental determination of FRP - concrete cohesive interface properties under fatigue loading", *Composite Structures*, Vol. 94, no. 4, 2012, pp. 1288 – 1296
39. Kamel A., Elwi A., Cheng R., "Experimental investigation on FRP sheets bonded to concrete", *Emirates Journal Engineering Resources*, Vol. 9, no. 2, 2004, pp. 71–76
40. Subramaniam K.V., Carloni C., Nobile L., "Width effect in the interface fracture during shear debonding of FRP sheets from concrete", *Engineering Fracture Mechanics*, Vol. 74, no. 4, 2007, pp. 578 – 594
41. Arutiunian N., "Contact problem for a half-plane with elastic reinforcement", *Journal of Applied Mathematics and Mechanics*, Vol. 32, no. 4, 1968, pp. 652–665
42. Benscoter S., "Analysis of a Single Stiffener on an Infinite Sheet", *Journal of Applied Mechanics*, Vol. 16, 1949, pp. 242–246
43. Brown E.H., "The Diffusion of Load from a Stiffener into an Infinite Elastic Sheet", *Proceedings of the Royal Society of London Series A*, Vol. 239, no. 1218, 1957, pp. 296–310
44. Koiter W.T., "On the diffusion of load from a stiffener into a sheet", *Quarterly Journal of Mechanics and Applied Mathematic*, Vol. 8, no. 2, 1955, pp. 164–178
45. Melan E., "Ein Beitrag zur Theori geschweisster Verbindungen", *Ingenieur Archiv*, Vol. 3, 1932, pp. 123–129
46. Reissner E., "Note on the Problem of the Distribution of Stress in a Thin Stiffened Elastic Sheet", *Proceedings of the National academy of Sciences of the United States of America*, Vol. 26, no. 4, 1940, pp. 300–305
47. Alaca B.E., Saif M., Sehitoglu H., "On the interface debond at the edge of a thin film on a thick substrate", *Acta Materialia*, Vol. 50, no. 5, 2002, pp. 1197 – 1209
48. Hu S.M., "Film-edge-induced stress in substrates", *Journal of Applied Physics*, Vol. 50, no. 7, 1979, pp. 4661–4666
49. Shield T., Kim K., "Beam theory models for thin film segments cohesively bonded to an elastic half space", *International Journal of Solids and Structures*, Vol. 29, no. 9, 1992, pp. 1085 – 1103
50. Yu H., He M., J.W.Hutchinson, "Edge effects in thin film delamination", *Acta Materialia*, Vol. 49, no. 1, 2001, pp. 93–107
51. Erdogan F., Gupta G.D., "The Problem of an Elastic Stiffener Bonded to a Half Plane", *Journal of Applied Mechanics*, Vol. 38, no. 4, 1971, pp. 937–941
52. Guler M.A., "Mechanical Modeling of Thin Films and Cover Plates Bonded to Graded Substrates", *Journal of Applied Mechanics*, Vol. 75, no. 5, 2008,

p. 051105

53. Freund L., Suresh S., Thin Film Materials: Stress, Defect Formation and Surface Evolution, Cambridge University Press, 2008

54. Grigolyuk E., Tolkachev V., Contact Problems in the Theory of Plates and Shells, Moscow: Mir Pub., 1987

55. Villaggio P., “The problem of the stiffener and advice for the worm”, *Mathematical and Computer Modelling*, Vol. 34, no. 12-13, 2001, pp. 1423–1429

56. Villaggio P., “Brittle detachment of a stiffener bonded to an elastic plate”, *Journal of Engineering Mathematics*, Vol. 46, 2003, pp. 409–416

57. Irwin G., “Analysis of stresses and strains near the end of a crack traversing a plate”, *Journal of Applied Mechanics*, Vol. 24, 1957, pp. 361–364

58. Erdogan F., Gupta G.D., “On the numerical solution of singular integral equations”, *Quart Appl Math*, Vol. 29, 1972, pp. 525–534

59. Cherepanov G., Wit R.D., Cooley W., Mechanics of brittle fracture, McGraw-Hill International Book Co., 1979

60. Taljsten B., “Strenghtening of concrete prism using the plate-bonding technique”, *International Journal of Fracture*, Vol. 82, 1996, pp. 253–266

61. Anderson T., Fracture mechanics: Fundamentals and Applications, Taylor & Francis, 2005

62. Franco A., Royer-Carfagni G., “Energetic Balance in the Debonding of a Reinforcing Stringer: Effect of the Substrate Elasticity”, *International Journal of Solids and Structures*, Vol. 50, no. 11-12, 2013, pp. 1954 – 1965

63. Barenblatt G., “The Mathematical Theory of Equilibrium Cracks in Brittle Fracture”, *Advances in Applied Mechanics*, Vol. 7, Elsevier, 1962, pp. 55 – 129

64. Chen B., Wu P., Gao H., “Geometry- and velocity-constrained cohesive zones and mixed-mode fracture/adhesion energy of interfaces with periodic cohesive interactions”, *Proceedings of the Royal Society A: Mathematical, Physical and Engineering Science*, Vol. 465, no. 2104, 2009, pp. 1043–1053

65. NTC 2008, New Technical standards for Construction, Italian Ministry of Public Works (DM 14.01.08), 2008, [In Italian]

66. Ali-Ahmad M., Subramaniam K., Ghosn M., “Analysis of Scaling and Instability in FRP-Concrete Shear Debonding for Beam-Strengthening Applications”, *Journal of Engineering Mechanics*, Vol. 133, no. 1, 2007, pp. 58–65

67. Carrara P., Ferretti D., Freddi F., “Debonding behavior of ancient masonry elements strengthened with CFRP sheets”, *Composites Part B: Engineering*, Vol. 45, no. 1, 2013, pp. 800–810

68. Grande E., Imbimbo M., Sacco E., “Bond behaviour of CFRP laminates glued on clay bricks: Experimental and numerical study”, *Composites Part B: Engineering*, Vol. 42, no. 2, 2011, pp. 330–340

69. Pugno N.M., Ruoff R.S., “Quantized fracture mechanics”, *Philosophical Magazine*, Vol. 84, 2004, pp. 2829–2845

70. Mazzotti C., Savoia M., Ferracuti B., “A new single-shear set-up for stable debonding of FRP-concrete joints”, *Construction and Building Materials*, Vol. 23, no. 4, 2009, pp. 1529 – 1537, {FRP} Composites in Construction

71. Dundurs J., Mathematical theory of dislocations, chap. Elastic interaction of dislocations with inhomogeneities, American Society of Mechanical Engineers, 1969

72. Hills D., Solution of Crack Problems: The Distributed Dislocation Technique, Mathematics and Its Applications, Springer, 1996

73. Ballarini R., Keer L., Shah S., “An analytical model for the pull-out of rigid anchors”, *International Journal of Fracture*, Vol. 33, no. 2, 1987, pp. 75–94

74. Ballarini R., Miller G., Mukai D., “Analysis of branched interface cracks”, *Journal of Applied Mechanics*, Vol. 57, no. December, 1990, pp. 887–893

75. He M., Hutchinson J., “Kinking of a crack out of an interface”, *Journal of Applied Mechanics*, Vol. 56, 1988, pp. 270–278

76. Franco A., Royer-Carfagni G., “Cohesive debonding of a stiffener from an elastic substrate”, *Composites Structures*, Vol. 111, 2014, pp. 401–414

77. Franco A., Royer-Carfagni G., “Effective bond length of FRP stiffeners”, *International Journal of Non-Linear Mechanics*, Vol. 60, no. 4, 2014, pp. 46–57

78. ABAQUS, “Analysis Users Manual”, Version 6.10, Simulia

79. Michell J.H., “On the Direct Determination of Stress in an Elastic Solid, with application to the Theory of Plates”, *Proceedings of the London Mathematical Society*, Vol. 31, no. 1, 1899, pp. 100–124

80. Muskhelishvili N., Some Basic Problems of the Mathematical Theory of Elasticity, No. 1, Noordhoff, 1975

81. Krenk S., “On the use of the interpolation polynomial for solutions of singular integral equations”, *Quarterly of Applied Mathematics*, Vol. 32, 1975, pp. 479–484

82. Willis J., “A comparison of the fracture criteria of Griffith and Barenblatt”, *Journal of the Mechanics and Physics of Solids*, Vol. 15, no. 3, 1967, pp. 151 – 162

83. Bažant Z.P., Becq-Giraudon E., “Statistical prediction of fracture parameters of concrete and implications for choice of testing standard”, *Cement and Concrete Research*, Vol. 32, no. 4, 2002, pp. 529 – 556

84. Abramowitz M., Stegun I., Handbook of Mathematical Functions: With Formulas, Graphs, and Mathematical Tables, Applied Mathematics Series, Dover Publications, 1964